NASA CONTRACTOR REPORT





# AN ANALYTICAL STUDY OF THE MEASURED WALL PRESSURE FIELD UNDER SUPERSONIC TURBULENT BOUNDARY LAYERS

*by Thomas J. Black*

*Prepared by*
TRACOR, INC.
Rockville, Md.
*for Langley Research Center*



NATIONAL AERONAUTICS AND SPACE ADMINISTRATION • WASHINGTON, D. C. • APRIL 1968

NASA CR-888

# AN ANALYTICAL STUDY OF THE MEASURED WALL PRESSURE FIELD UNDER SUPERSONIC TURBULENT BOUNDARY LAYERS

By Thomas J. Black

Turbulent Boundary Layers



Issued by Originator as TRACOR Document No. RL/67-070-U

Prepared under Contract No. NAS 1-6952 by
TRACOR, INC.
Rockville, Md.

for Langley Research Center

NATIONAL AERONAUTICS AND SPACE ADMINISTRATION

For sale by the Clearinghouse for Federal Scientific and Technical Information
Springfield, Virginia 22151 – CFSTI price $3.00

ACKNOWLEDGMENT

The author's thanks are due to Mr. Toivo Tagamets who provided valuable assistance in the reduction and analysis of data throughout the program and in the preparation of this report.

TABLE OF CONTENTS

## ABSTRACT

This report presents the results of a short analytical study of the turbulent wall pressure field under supersonic shear layers. The study is based on a new, hitherto unpublished, theory of wall turbulence which is accordingly presented in some detail herein. The theory asserts that the turbulent transfer of mass, heat, momentum and energy within the boundary layer are essentially effected within discrete, horseshoe-vortex structures which are generated and maintained by powerful, localized non-linear instabilities within the sublayer and which move downstream over the wall in a characteristic, quasi-frozen, spatial array. In particular, the theory explains the generation of turbulent shear stress in terms of the dynamic interaction between these vortex systems and the basic shear flow through which they move. It suggests, furthermore, that the turbulent wall pressure field is an essential and integral part of the turbulent shear stress mechanism and hence provides a new analytical basis for the study of boundary layer noise.

On the basis of this theory, new scaling laws are proposed for the turbulent wall pressure field under subsonic and supersonic layers. These laws feature quite different scaling parameters for the high and low frequency portions of the spectra and indicate the effect of pressure gradient on the spectra.

The proposed laws are evaluated first on the basis of experimental data measured by various investigators in subsonic layers, and are subsequently examined in the light of supersonic wall pressure data obtained in wind-tunnel tests and in flight tests on high-speed aircraft and space vehicles.

# INTRODUCTION

In recent years, the design and development of aerodynamic vehicles operating at supersonic speeds has stimulated considerable practical interest in the mechanics of turbulent boundary layer flow and, in particular, in the structure of the fluctuating wall pressure field under supersonic layers. This interest is dictated by three main problem areas pertaining to (1) the response of surface structures exposed to turbulent flows; (2) the generation of aerodynamic noise by turbulent boundary layers; (3) aerodynamic heating of supersonic vehicles.

These problems are of particular significance in the design of space vehicles and of the projected supersonic transport aircraft. In space vehicles, the problems are particularly acute in the base region of the craft, where the highly turbulent recirculation flow subjects the base structure to very large unsteady acoustic,aerodynamic and thermal loads. Also of considerable importance are the fluctuating aerodynamic loads which occur on or near protuberances on the vehicle body and in the region of shock systems established at geometrical discontinuities on the body.

On the commercial supersonic transport aircraft, major problems are likely to include cabin noise, aerodynamic heating of specific regions and dynamic loading of surface structures caused by turbulent flow.

The study of these problems, insofar as they are related to turbulent shear flow phenomena has been appreciably

hampered by the absence of a sound physical understanding of the mechanism of heat, mass and momentum transfer in turbulent flows. In particular, the experimental study of the turbulent wall pressure field under both subsonic and supersonic layers has lacked a suitable analytical framework against which the data collected can be correlated and compared.

The conventionally accepted method of analyzing wall pressure spectra on a 'Strouhal' basis has not been entirely successful in correlating subsonic data, while available supersonic data plotted on this basis reveals large discrepancies which cannot be ascribed to compressibility effects and must therefore be attributed to an incorrect or inadequate analytical basis.

In the absence of adequate scaling laws, the experimental data recorded in wind-tunnel tests cannot be extrapolated with confidence to specific full-scale conditions (a severe problem in the case of aerospace vehicles which generally operate at much higher Reynolds' number than those attainable in most test facilities) while detailed flight-measurements are extremely expensive to obtain on research aircraft and prohibitively so in the case of space vehicles. Furthermore, there are strong grounds for suspecting that the usefulness of many experimental studies already completed may be severely restricted by the omission of certain specific local measurements

not hitherto considered relevant to the analysis of the recorded data. For these reasons it is clearly of prime importance that a sound basis for analyzing wall pressure data be established.

The principal investigator in the present study has recently developed a new theory of wall turbulence (reported briefly in ref. 1) which offers hope of a completely new analytical approach to the study of turbulent shear layers. It permits a deterministic treatment of the large-scale unsteady motions (so-called large eddies) of turbulent flow and provides a simple physical picture of the mechanics of heat, mass and momentum transfer in turbulent layers. In particular, it provides a new basis for the analysis of the turbulent wall pressure field.

The present study was consequently conducted in order to re-examine all available relevant data in the light of the new analytical framework provided by the theory. The specific tasks involved included (1) the collection, correlation and evaluation of existing data relating to the supersonic wall pressure field, (2) the development of new scaling laws for this data, and (3) the extension of the theory, where necessary, to encompass compressibility effects including those other than the local variation of fluid properties.

As indicated earlier, the basic theory underlying the present study has not yet been presented in any detail in the literature; furthermore the fundamental concepts involved have undergone some appreciable development in the course of the present program. For these reasons, a fairly full and detailed description of the theory as developed for incompressible turbulent layers is presented first in section 2, herein. In section 3, scaling laws are developed for analysis of experimental data. In section 4, the theory is then applied to the analysis of a selected range of subsonic wall pressure data in order to establish its validity in this regime before attempting the analysis of supersonic data. Also in section 4, the theory is extended to the case of supersonic layers and the subsequent analysis of the supersonic data acquired is reported.

## 2.0 THEORETICAL BASIS FOR THE STUDY

### 2.1 The Instability Hypothesis

The present theory of wall turbulence is founded on the belief that the mechanism responsible for turbulence production and momentum transfer in the shear layer, involves a strong, repetitive non-linear instability of the flow within the viscous sublayer. The concept of repetitive flow breakdown within the fully-developed turbulent layer is not a new one. In 1956, Einstein and Li[2] put forward a novel theory in which they suggested that the viscous sublayer undergoes alternate periods of slow viscous growth and rapid breakdown. Their physical model provided a quantitative description of mean-flow and statistical properties of the sublayer which agreed remarkably well with measured data. Furthermore, their measurements of auto-correlated wall pressure fluctuations under a fully-developed turbulent boundary layer provided some direct evidence of a periodic structure in the sublayer flow in support of their theory.

While the Large Eddy Equilibrium Hypothesis proposed at the same time by Townsend[3] appears to hold little common ground with Einstein and Li's theory, it does incorporate the suggestion that the large eddies of turbulent motion are generated by chance instabilities of the basic shear flow. Grant[4]

proposed an alternative interpretation of available statistical data, suggesting that the large eddies are, in fact, stres-relieving motions comprising coherent transverse 'mixing jets' which result from an instability in the turbulent shear stress mechanism. More recently, Malkus[5] and Landahl[6] have suggested that hydrodynamic instability may play a key role in fully-developed wall turbulence.

There are indeed considerable grounds for proposing such a hypothesis. Let us consider, for example, the logical (though by no means simple) approach to fully-developed wall turbulence afforded by our present understanding of the process of transition from laminar to turbulent flow. The early stages in this process, involving the development of the Tollmein-Schlichting instability at some critical Reynolds' number have been well understood for some considerable time and analytical predictions relating to the onset of instability have been closely verified experimentally. However, the strongly non-linear nature of the subsequent processes by which the initially weak two dimensional, Tollmein-Schlichting waves are progressively amplified and finally breakdown to provide a fully-turbulent regime, has so far precluded a rigorous analytical treatment of the later stages of transition. Knowledge of these processes is consequently limited to an intuitive physical picture developed largely on the basis of experimental studies conducted in recent years.

It has become increasingly apparent from these studies, that some form of secondary instability is responsible for the actual generation of turbulence. This process evidently involves a spanwise warping of the amplified Tollmein-Schlichting waves leading to a concentration of disturbance amplitude along preferred streamwise parallel lines. Turbulence first appears in small 'spots' which develop spontaneously and periodically along these lines of maximum distrubance amplitude. The spots subsequently move downstream and increase in size until they finally coalesce to exclude all intervening regions of laminar flow and so provide a fully-turbulent layer. The few experimental studies so far devoted to the detailed spot structure tentatively suggest that the flow within each spot is very similar, if not identical to fully-developed wall turbulence.

The actual birth of the turbulence spot is now generally attributed to a secondary non-linear instability and breakdown of the perturbed laminar flow. Benney and Greenspan[7], for example, suggest that the progressive amplification of the Tollmein-Schlichting waves modifies the basic laminar velocity profile until inflexional instability occurs; and have further shown that such an instability could account for very large energy transfer rates consistent with the sudden appearance of a turbulence spot.

If this is the case, the continuing production of turbulence within the spot as it moves downstream (as evidenced by the growth of the spot) would seem to suggest that the instability responsible for its birth is not transient, but, in fact, persists and accompanies the spot into the fully developed flow regime. If, furthermore, each spot does indeed comprise a region of self-sustaining fully-turbulent shear flow, then it is reasonable to suspect that the instability within the spot may be responsible not only for turbulence production, but also for the turbulent transfer of momentum. The final step in this argument then suggests that the instabilities distributed throughout the turbulence spots in the transition regions continue to govern the processes of turbulence production and momentum transfer, even when the spots have coalesced to form a fully-developed shear layer.

If the preceeding argument is correct, then careful inspection of fully-developed wall turbulence should reveal a quasi-frozen array of localized non-linear instabilities moving downstream with some characteristic wave velocity. Immediately downstream of the transition regime, the distribution of these instabilities over the wall in the fully-turbulent layer will be determined by their prior distribution among the transitional turbulence spots. As they move downstream, however, it seems likely that their distribution (lateral and streamwise spacings) will be determined by local boundary layer parameters and hence

will vary with local Reynolds' number, a process which must involve either the generation of new additional instabilities as the flow develops downstream, or the decay of some existing ones. Indeed it is probable that both decay and regeneration of instabilities will occur simultaneously throughout the layer, the net streamwise variation in their density distribution over the wall depending upon the extent to which one process predominates.

Strong experimental support for such a physical picture has been provided in recent years by the remarkable visual studies conducted by Kline and his colleagues[8] [9]. These studies have revealed a distinctive spatio-temporal flow pattern in the sublayer and blending region in which fluid is periodically and violently ejected outwards from the wall in localized jet-like motions. These eruptive motions exhibit a characteristic distribution over the wall which appears to scale on the sublayer thickness and are generally consistent with the presence of a moving array of powerful, locally-disruptive instabilities located near the edge of the sublayer.

The repetitive ejection of fluid from the sublayer observed by Kline et al. also lends support to Grant's 'mixing-jet' hypothesis. Indeed the notion that the primary function of the observed eruption process is to periodically relieve a

viscous stress build-up in the sublayer is not only intuitively attractive, but also provides a basis for incorporating Einstein and Li's unsteady sublayer model in a more general unified theory. In this regard, the recent experimental study by Willmarth and Tu [10] should also be mentioned, since their data is consistent with the existence near the wall of counter-rotating pairs of Townsend's large eddies accompanied by an associated outflow of fluid between the eddy-pair compatible with the 'mixing-jets' proposed by Grant.

Thus the instability hypothesis proposed herein not only furnishes an approach to wall turbulence which is consistent with the observed behavior of the flow; it also provides a basis for reconciliation of a number of diverse flow models already proposed and holds out some hope for the construction of a unified theory of wall turbulence.

## 2.2 The Nature of the Instability

If the foregoing hypothesis is correct, the actual array of instabilities within the full-developed shear layer will undoubtedly exhibit a complex and ever-changing geometrical pattern in which individual units may decay or new ones may be generated; and in which the instantaneous spacing of the units in both lateral and streamwise directions may vary considerably about characteristic mean values. In order to develop an analytical approach, it will initially be necessary to adopt

a more simple model of the instability distribution. It will therefore be assumed, for the present, that (see Fig. 1)

1. The instabilities move as a perfect frozen pattern at a constant wave velocity $\bar{U}_i$;

2. The instabilities line up in rows in the flow direction with constant streamwise spacing $l_x$;

3. The lateral spacing, $l_z$, of these rows is constant and,

4. The entire flow in each streamwise 'slice' or section of the boundary layer containing a single row of instabilities can be treated in isolation from the flow in neighboring 'slices' so that (for example) the phase-relationship between the distribution of instabilities in neighboring rows is unimportant.

Assumptions (1) through (3) imply that instabilities neither decay nor regenerate as they move downstream and that the downstream Reynolds' number variation of parameters is consequently neglected. Assumption (4) does <u>not</u> require that the flow in each streamwise slice be two-dimensional, but merely that mutual interference effect between adjacent rows may be neglected. These assumptions will have to be re-examined at some later stage; for the moment, however, they permit a simple first step towards the construction of a more sophisticated model.

This first step must clearly consider the nature of the hypothesized instability and the manner in which it interacts with the boundary layer flow field in its immediate vicinity. Let us therefore consider first the boundary layer flow in the fixed coordinate system x, y, z in which x and z lie in the wall, parallel and normal to the freestream respectively and y is normal to the wall. It will be assumed that the layer is fully turbulent and well behaved, that the mean flow is two-dimensional in the x-y plane and that, for the moment, no pressure gradient is present. Let the instantaneous motion at any point be represented by $q(x,y,z,t)$ where q may be identified with any one of the velocity components u,v,w parallel to x,y,z respectively or with the instantaneous pressure, p.

Then at any fixed x-station, the flow in any streamwise 'slice' as previously defined will, according to the simple model of Figure 1, experience a periodic instability which occurs with frequency $\frac{\overline{U}_i}{l_x}$. The question now arises as to what motion within the layer becomes periodically unstable. Evidently, the mean motion (which by definition

$$\overline{q}(x,\ y) = \frac{1}{\Delta t} \int_{t}^{t+\Delta t} q(x,\ y,\ z)\ dt \qquad (2.1)$$

(where $\Delta t$ is a suitably-chosen time interval).
is invariant with time) cannot exhibit a periodic instability

of the type proposed. Nor again, can the turbulent motion, $q'(x, y, z, t.)$ (which, by its very definition is random in nature) exhibit the regular behavior required by the model. It would therefore seem that the classical division of the instantaneous motion into mean and turbulent components, i.e.,

$$q(x, y, z, t.) = \overline{q}(x,y) + q'(x,y,z,t.) \qquad (2.2)$$

is not adequate for present purposes, and that we must instead express q as the sum of two unsteady component motions, i.e.,

$$q(x,y,z,t) = q^*(x,y,z,t.) + q'(x,y,z,t) \qquad (2.3)$$

where $q'$ is the random turbulent component so defined (as in the classical sense) that

$$\overline{q'} = 0 \qquad (2.4)$$

and $q^*$ is an organized, non-random time-dependent motion (hence-forth referred to as the primary motion) which becomes periodically unstable as required and upon which the turbulent (secondary) motion, $q'$, is superimposed. It follows from equations 2.3 and 2.4 that the mean motion is simply the time-average value of the primary motion, i.e.,

$$\overline{q} = \overline{q^*}\ (x, y.) \qquad (2.5)$$

and in particular, if q is identified with the streamwise velocity component, the mean velocity distribution in the region for which equation 2.3 applies is

$$\overline{u} = \overline{u}^{*}\ (x,y) \qquad (2.6)$$

The physical significance of the primary motion becomes evident if we now examine the flow in the moving-axis systems, $\left[ (x - \overline{U}_i t)\ y,\ z \right]$, which is fixed relative to the instability array. While the transformation involves the instability wave velocity $\overline{U}_i$, it will be sufficient at this point to assume (in the light of the experimental evidence of Kline) that

$$o < \overline{U}_i < U^{\infty} \ . \qquad (2.7)$$

Where $U_\infty$ is the freestream velocity. Then relative to an observer in the moving-axis system, the wall moves "upstream"* with velocity, $\overline{U}_i$ while the fluid outside the layer moves "downstream" with velocity $U_\infty - \overline{U}_i$. To such an observer, the overall exchange of momentum and energy between the wall and the freestream will appear as a two-stage process: one stage

*Quotes (" ") will be used to denote motion relative to the moving axis system. Thus, for example, all fluid particles whose streamwise velocity is less than $\overline{U}_i$ will move "upstream" in the moving-axis system, even though their motion relative to the wall is in the downstream direction.

involves the transfer of momentum and energy from the wall to the instability system across the velocity "jump" $\overline{U}_i$; while the other involves transfer between the instability system and the freestream across the velocity step, $U_\infty - \overline{U}_i$.

If such a view of the flow is to have any real physical significance, it is clear that: (1) the two transfer processes must involve quite different physical mechanisms and (2) the instabilities (and any local flow description associated with them) must provide the link or interface between the two transport mechanisms.

If this is the case, we may now "separate" the two processes and examine each independently in more detail. In the first place, it is clear that the "inner" process, involving transfer of momentum and energy from the wall, must be governed essentially by viscosity (at least, in the case of aerodynamically smooth walls) and will generate an inner velocity distribution in which the flow moves "upstream" through successive instability locations. Since the hypothesized instabilities are located in or near the viscous sublayer, it is evidently the inner motion which breaks down repeatedly in space (in the moving-axis system) to feed and maintain the instabilities. It also follows that the spatially unstable "inner" motion and the primary motion (which is temporally unstable in the fixed axis system) are essentially

the same and are related through the vector equation

$$\left[\overrightarrow{\text{inner motion}}\right] = \bar{U}_i - \vec{q^*} \qquad (2.8)$$

Thus the inner (primary) motion undergoes spatial (temporal) periods of viscosity-governed development, during which it acquires energy and momentum from the wall through the viscous shear stress gradient. These periods are then regularly terminated by a rapid, non-linear instability and breakdown of the flow during which the energy and momentum accumulated during the previous cycle are transferred to some alternate motion generated by the instability.

Since the non-viscous (i.e., turbulent) transport process in the inner region is attributed to the (as yet undetermined) action of the instability and some local perturbation field associated with it, the Instability Hypothesis implies that the random turbulence superimposed upon the inner, primary motion will not effect any net turbulent transfer of momentum during the development period between successive instabilities. Consequently the development of the primary motion will be governed solely by the viscous shear stress and pressure gradients present.

The energy lost by the primary motion at each instability must clearly be transferred to an alternative motion which must necessarily be vortical in nature.

Furthermore, if the instability is to achieve a gross transfer of mean momentum between the inner and outer regions of the layer, the vortical motion which it generates must be suitably organized (and therefore essentially non-random) and must develop on a scale comparable with that of the shear layer itself. The instabilities may thus be regarded in the moving-axis system as fixed continuous sources of discrete vorticity, or vortex generators which feed and maintain ordered and probably complex vortex structures within the layer. These vortex structures, in transporting momentum across the layer, evidently interact with the basic shear flow to generate turbulent shear stress. Since turbulent motion generally involves much higher energy losses than its laminar counterpart, a large portion of energy which they acquire from the primary motion must subsequently be expended in the transfer process. The vortex structures thus also apparently provide the major source of turbulence production in the layer in accord with the Instability Hypothesis.

Before examining the nature of these vortex structures in more detail, we shall complete this tentative, initial picture of the flow structure by considering briefly the "outer" motion which must be responsible for the final transfer of energy and momentum from the instability/vortex system to the freestream. This motion must evidently involve

the "smoothing" of the outer velocity "jump," $U_\infty - \overline{U}_i$, since it is inconceivable that the inner, primary motion as defined can have both "upstream" and "downstream" components in the moving-axis system, with totally unrelated "histories." The outer motion will consequently exhibit a "wake-type" structure in which viscosity plays a negligible role (except in the ultimate dissipation of turbulent energy), and which is dominated by turbulent entrainment of freestream fluid and characterized by intermittence.

Little further progress can be made in the analysis of the outer motion until the nature of both the inner motion and the instability/vortex systems are more clearly defined. However, we may note at this early stage that the physical picture emerging is strongly consistent with the semi-empirical analysis developed by Coles[11] on the basis of his Laws of the Wall and Wake. Indeed the present model, if once substantiated, removes a major (perhaps the only major) fundamental objection to Coles analysis; namely that a motion governed by the (apparently) strongly non-linear Reynold's equations should be capable of description as the simple sum of two independent universal component motions. It does so by ascribing physical significance to the moving-axis system $(x - \overline{U}_i t, y, z)$ which "splits" the flow into two quite distinct motions, so that a "priviliged" observer in that system sees on one hand a viscous-governed inner motion developing "upstream" and an inertia-governed

outer motion developing "downstream." Clearly, the inner and outer motions must be closely related respectively to the Law-of-the-Wall and Law-of-the-Wake proposed by Coles[11].

We shall see later that the "smoothed" velocity distribution in the outer, wake-type motion only exists because the inner motion in the real boundary layer does not exhibit the perfect regularity and symmetry of the simple model assumed so far; and because, in particular, the real instability/vortex systems do not exist indefinitely, but undergo a constant process of decay and regeneration. For the moment, however, it is sufficient to assume that the inner, primary motion can be analyzed in isolation from any mechanism which may exist in the outer region of the layer. Specifically, we shall confine our application of the simple, perfectly-regulated model to the inner region, including the fully turbulent region, the blending zone (so-called) and the viscous sublayer.

The tentative model so far developed may thus be conveniently summarized in block diagram form as in Figure 2, which shows schematically the stages involved in the transfer of energy and momentum from the wall* through the inner region of the boundary layer. As shown, the initial transfer of energy and momentum from the wall to the primary motion is achieved by the viscous shear stress gradient, a process accompanied by an energy loss due to direct-viscous-dissipation. The

*The sense of the energy transfer (i.e., from the wall to the fluid) is appropriate to an observer in the moving-axis system.

second stage involves transfer from the primary motion to some as yet undefined, organized vortex structure which is effected periodically by a repetitive instability of the primary motion. A considerable amount of the energy fed into the vortex structure must evidently be lost in turbulence production. Since the ambient turbulence level is known to exert some considerable influence on the development of fully-turbulent wall layers, some feed-back system linking the background turbulence must fulfill this feed-back requirement by controlling the strength of the instability and hence, the rate of energy transfer from the primary motion. This role is, of course, intuitively attractive, since the effect of ambient turbulence level on hydrodynamic instability is well-established. Concurrent with the loss of energy in the primary motion and vortex system, some momentum is also lost due to the convective acceleration associated with downstream development of the layer. Finally the energy and momentum remaining in the vortex system is transferred to the freestream by some mechanism yet to be determined.

We will now consider in some detail the probable nature of the instability and the associated vortex structure responsible for the non-viscous transfer of energy and momentum between the inner and outer motions.

## 2.3 The Nature of the Instability and Associated Vortex Structure

Consider, in the moving axis system $(x-\overline{U}_i t, y, z)$ the development of the primary or inner motion through a complete development/breakdown cycle; that is to say, from the point at which it leaves one instability location (A) (see Figure 3) to that at which it emerges from the next one(B) immediately "upstream." We can make three statements regarding the change which occurs in the velocity distribution, $\overline{U}_i - u^*$, (taken as positive in the "upstream" sense) during its viscous development between A and B namely:

1. The velocity at the wall must remain unchanged and equal to $\overline{U}_i$ to satisfy the zero-slip condition;

2. The primary velocities will generally be increased by the viscous shear stress gradient between A and B, since our model requires an input of energy from the wall to replace that lost to the instability at A, and hence an increase in energy flux

$$\left( = \tfrac{1}{2} \int_o^y \rho \quad (\overline{U}_i - u^*)^3 \, dy \right) \text{ between A and B;}$$

3. This energy input must involve a progressive modification of the profile which is initiated at the wall so that in the finite distance between A and B the overall change

in the profile will be confined to a limited region $0 \leq y \leq \delta_s$ (say) immediately adjacent to the wall. This region will later be identified with the so-called viscous sublayer and we shall therefore formally define $\delta_s$ as the sublayer thickness.

According to the above statements, the primary velocity distribution must vary between A and B in the manner shown in Figure 3; that is, the profile will become progressively less concave and consequently more unstable as it develops, consistent with the Instability Hypothesis. Within the localized unstable regime at B, the energy-enriched profile breaks down and rapidly reverts to its initial development condition once more, giving up its excess energy to the vortex system generated by the instability.

We shall now examine the transport of mass, momentum and vorticity through a small control volume which just encloses the instability; is bounded in part by the wall and by the parallel plane $y = \delta_s$; and extends laterally across one complete instability width or "slice" as defined earlier. It is evident, first, that the reduction in primary mass flow through the control volume associated with the loss of energy flux must be compensated by a corresponding outflow of fluid away from the wall as in Figure 4a (lateral outflow through the sides of the control volume is intuitively less likely and would violate the basic assumption regarding mutual interference between adjacent instability bands).

This jet-like efflux of fluid will at the same time transport streamwise momentum vertically out of the control volume to compensate the reduction in primary momentum flux through the volume. The mean motion, however, will not "see" this periodic outward ejection of mass and momentum and will thus attribute the intermittent loss of primary momentum in the moving-axis system to the action of an apparent mean shear stress in the fixed axis system (Figure 4b). We may now identify this apparent stress with the "turbulent" shear stress in accordance with the basic premise that the turbulent transfer mechanism is governed directly by the instabilities in the shear layer. It is easily shown that if the turbulent shear stress gradient thus established is to be positive throughout the sublayer in agreement with experimental observation, then $\overline{U}_i > u^*$ everywhere in that region. The condition that the instability wave velocity exceed the primary velocities throughout the sublayer (and as will be seen later more generally, throughout the wall region) is evidently a fundamental requirement of the present model.

The transport of vorticity through the instability region is governed by the classical theories relating to vorticity in an incompressible fluid, i.e.:

1. The creation and diffusion of vorticity are effected only through the action of viscosity; in particular, vorticity can originate only at a solid boundary and not in the interior of the fluid.

2. The strength of a vortex line at any instance is the same at all points along the line; consequently such a line cannot end at an internal point but must either form a closed curve or terminate at a solid boundary.

3. In an inviscid fluid, the particles within a discrete vortex tube remain a part of the tube during its entire motion; furthermore, according to (1) the strength of such a tube is invariant with time, consequently the vorticity is convected with the fluid; in a viscous fluid, this convective property is modified only insofar as the vorticity is diffused by viscosity as it is convected.

It is now required to develop a plausible physical picture of the assumed process of discrete vortex generation by the instability. The problem is most easily approached in two stages in which the entire flow process within the instability regime is first considered to be two-dimensional in the $(x-\overline{U}_i t, y)$ plane (Figure 4c).

Since the streamwise extent of the instability regime is very small compared with the corresponding development length of the cycle and since the instability mechanism has to effect within that small space, a non-viscous (i.e., turbulent) transfer of momentum equivalent to that achieved by viscosity over the entire development length, it follows that the effect of viscosity

in either generating or dissipating vorticity within the instability region will be negligibly small. We may therefore assume that vorticity is conserved during the breakdown process and accordingly equate the net change in primary vorticity flux through the control volume to the rate at which discrete vorticity is generated by the instability inside it. Assuming two dimensionality, the former quantity may be written as

$$\left.\begin{array}{l}\text{change in}\\ \text{primary vorticity}\\ \text{flux through}\\ \text{control volume}\end{array}\right\} = \left[\int_0^{\delta_s}\left(\bar{U}_i - u^*\right)\left(\frac{\partial v^*}{\partial x} - \frac{\partial\left(\bar{U}_i - u^*\right)}{\partial y}\right)dy\right]_{IN} - \left[\int_0^{\delta_s}\left(\bar{U}_i - u^*\right)\left(\frac{\partial v^*}{\partial x} - \frac{\partial\left(\bar{U}_i - u^*\right)}{\partial y}\right)dy\right]_{OUT}$$

where $v^*$ is the y component of the primary motion

$$\approx \left[-\int_0^{\delta_s}\left(\bar{U}_i - u^*\right)\frac{\partial\left(\bar{U}_i - u^*\right)}{\partial y}\,dy\right]_{IN} - \left[-\int_0^{\delta_s}\left(\bar{U}_i - u^*\right)\frac{\partial\left(\bar{U}_i - u^*\right)}{\partial y}\,dy\right]_{OUT}$$

$$= \left[-\frac{1}{2}\int_0^{\delta_s} d\left(\bar{U}_i - u^*\right)^2\right]_{IN} - \left[-\frac{1}{2}\int_0^{\delta_s} d\left(\bar{U}_i - u^*\right)\right]_{OUT}$$

$$= 0 \qquad (2.9)$$

since the velocities at y=o and at $y=\delta_s$ are unchanged throughout the breakdown process. It follows from (2.9) that if any discrete vorticity is generated within the control volume, it must appear in the form of contra-rotating vortex pairs of equal and opposite sign. This will evidently be the case. Inspection of the primary

velocity distribution indicates that its viscous development is accompanied by a steady net transfer of vorticity from the inner to the outer part of the growing sublayer, so that over the complete development phase, the vorticity is reduced close to the wall and increased near the edge of the sublayer. Within the short breakdown region, the initial distribution of vorticity must be rapidly restored. This can only be achieved if the excess vorticity accumulated in the outer part of the sublayer is transferred to discrete vortices having the same rotational sense; while the vorticity in the inner part of the sublayer is "boosted" by the generation of discrete vortices of opposite sign. This process can, perhaps, be more readily understood if the development of the primary motion is viewed as a process of viscous distortion of the basic (initial) primary distribution which emerges from the breakdown region. If we consider only the distortion itself, rather than the entire velocity distribution, we see that it comprises a growing profile similar to that of a free jet (Figure 5). The subsequent reversion of the primary motion to its original (initial) form can be logically explained by the breakdown of the distortion profile into contra-rotating vortices in a manner similar to the breakdown of the two-dimensional laminar jet. (It is not suggested, however, that the cause of instability is necessarily the same as that of laminar free shear layer instability since the addition of the

initial primary profile eliminates the inflexion point evident in the distortion profile alone.)

The only major modification likely to be introduced by the evident three-dimensionality of the actual flow structure relates to the geometry of the discrete vortex elements created and shed by the instability. Since, in practice, the instability region has only finite lateral extent, the two-dimensional infinitely long vortex pair in the simple model above must now be replaced by a vortex pair of finite extent whose ends are linked by trailing vortices to form a closed vortex-ring (Figure 6).

Thus the requirements governing the conservation of mass, momentum, energy and vorticity in the unstable region within the sublayer are generally satisfied if we assume that breakdown of the primary flow is accompanied by:

1. The generation and shedding of ring vortices at some characteristic rate evidently determined by the precise nature and strength of the instability.

2. The transfer of accumulated energy within the sublayer to this vortex system;

3. A local jet-like eruption of fluid away from the wall, and

4. An associated, non-viscous transfer of momentum which the mean motion "sees" as a turbulent shear stress gradient.

The vortex rings once created will subsequently be convected in part by the primary motion and in part by their own self-induced flow field. The convective action of the primary motion is two-fold. In the first place it will tend to "blow away" the vortices "upstream" from their point of origin; it will, however, at the same time shear the vortex rings so that the plane containing each ring steadily rotates about the z-axis and the trailing elements in each ring are progressively stretched. On the other hand, the self-induced flow field of the vortex tends at any instant to propel the vortex along a line normal to its own plane. Consequently, as the vortex ring is rotated by the primary motion, the outer spanwise element will be convected outwards from the wall by the steadily increasing vertical component of the induced flow field. Since (in the moving-axis system considered) the primary velocity decreases with distance from wall, the path of the outer spanwise element will curve progressively away from the wall (Figure 7).

The inner spanwise element, however, will not move away from the wall as it is convected "upstream" by the primary motion, since the vertical component of the induced flow field is cancelled very close to the wall by the vortex image system reflected in the wall. Consequently, the inner and outer spanwise elements move steadily apart thereby continuously stretching the linking trailing vortices. The inner element can now be neglected on the

the grounds (1) that its effect on the flow is almost entirely neutralized by the proximity of its image in the wall and (2) that it will rapidly diffuse as a result of its proximity to the wall. Thus, in effect, the discrete vortices shed by the instability can be regarded as horseshoe vortices whose feet are attached to, and fixed relative to the wall and whose outer spanwise (hereafter referred to simply as spanwise) elements are carried outwards from the wall thereby stretching the trailing legs (Figure 7).

While the horseshoe vortices move continuously away "upstream" and outwards from their point of origin, they do so through a surface which is fixed relative to the instability. This surface comprises a "front" defined by the characteristic path of the spanwise element and by the lateral extent of the instability; and two "sides" which contain the loci of all points in the trailing vortex elements. Thus, the vortices do not in any real sense "blow away" from their point of origin but instead establish and maintain a vortex structure which moves with the instabilities downstream.

If it is assumed that the rate of generation of vortices by each instability is relatively high, then the surface defined above may contain a number of vortices in various stages of evolution at any given instant. If, in particular, the

frequency of generation were infinite (with each vortex infinitely weak to provide the finite rate of vorticity transport required) then the surface would comprise a vortex sheet, fixed in the moving-axis system, through which the primary motion consequently passes.

In practice, such a sheet would be unstable and would rapidly breakdown into the discrete horseshoe vortex elements actually proposed in the present model. However, the concept of the surface as a vortex sheet is both valid and useful in analyzing the interaction between the multiple-horseshoe vortex system proposed and the primary motion which passes "upstream" through it.

The suggestion that the turbulence mechanism in wall shear layers is controlled by horseshoe vortices is not, in itself, a new one. Theodorsen[12] in 1952, proposed a model of wall turbulence which features discrete, characteristic horseshoe vortices of a type very similar to the individual elements within the horseshoe structure proposed herein, and suggested that the turbulent transport mechanisms were generated by the interaction between these vortices and the basic flow. The relationship between Theodorsen's model and the present one is discussed briefly in Section 2.6.

## 2.4 The Self-Induced Motion of the Vortex Structure.

So far we have considered the self-induced motion of a simple ring or horseshoe vortex element only. However, the composite vortex structure, which may comprise a number of these vortex elements, and which we may now regard tentatively as a horseshoe vortex sheet, will induce a more general three-dimensional flow field in its vicinity. In particular, it will induce, within itself, an outflow of fluid from the wall which is, of course, consistent with mass continuity requirements in the breakdown region as discussed earlier (Figure 4a).

Of immediate interest, however, is the self-induced streamwise component motion of the vortex system. In determining the nature of this motion, we may reasonably neglect the contribution of the trailing vortex elements in the sides of the horseshoe sheet, since the associated vorticity vectors are rapidly rotated by the shearing action of the primary motion and hence quickly cease to provide a streamwise component of velocity. Consequently, the induced streamwise motion will be determined essentially by the spanwise vorticity in the front of the sheet. In order to obtain a first approximation to this motion, we shall make the following simplifying assumptions, namely;

(1) that the front of the vortex structure is plane and normal to the wall (whereas, in fact, it is curved and inclined in the 'upstream' direction).

(2) that despite the finite lateral extent of the sheet, the induced flow may be regarded as a two-dimensional motion in the ( $\chi - \bar{U}_i t, y$) plane, and

(3) that the vortex structure extends outwards some distance $\Delta$ from the wall, where $\Delta$ is comparable with the boundary layer thickness $\delta$.

We therefore consider a plane normal to the $(\chi-\bar{U}_i t)$ axis in which z-vorticity is distributed smoothly between the wall and some point $y=\Delta$ (Figure 8). We will assume for the moment that the vorticity density per unit distance from the wall is some function $\gamma(y)$ of y. Then the self-induced streamwise velocity $u_\gamma(y)$ at a point in the vortex sheet is given by

$$u_\gamma(y) = \frac{1}{2\pi} \int_0^\Delta \frac{\gamma dy'}{y'-y} + \frac{1}{2\pi} \int_0^\Delta \frac{\gamma dy'}{y'+y} \qquad 2.10$$

where the first term on the right-hand side comprises the contribution of the sheet itself and the second term that of the image system required to satisfy the boundary condition $v_\gamma=0$ at the wall. In order to evaluate equation 2.10, the vorticity density distribution $\gamma(y)$ must first be determined. The following simple considerations reveal a significant property of the vortex system.

Suppose the discrete horseshoe vortices, of which the sheet is actually composed, are shed by the instability at some frequency, n, and with individual strength $\Gamma(y)$ which may in

general vary as the vortex moves out through the layer. The velocity $v_\gamma$ with which the spanwise elements move outwards is induced essentially by the associated trailing elements, also of strength $\Gamma(y)$, and is given by

$$v_\gamma = \text{const.} \quad \frac{\Gamma}{l_z} \qquad 2.11$$

where $l_z$ is the lateral extent of the instability, that is, the distance between the trailing elements. Then the vorticity flux in the sheet at any $z$ will be

$$n\Gamma = v_\gamma \gamma \qquad 2.12$$

and so from 2.11

$$\gamma \propto \frac{n\Gamma l_z}{\Gamma}$$

$$\propto n\, l_z \qquad 2.13$$

Hence $\gamma$ is independent of $z$, irrespective of how the individual strength of each vortex element may vary with $z$.

Since n and $l_z$ will evidently scale on the sublayer parameters $\nu$ and $\bar{U}_\tau$ ($\equiv \sqrt{\frac{\bar{\tau}_o}{\rho}}$) it follows that

$$n \propto \frac{\bar{U}_\tau^2}{\nu} \qquad 2.14$$

$$\text{and } l_z \propto \frac{\nu}{\bar{U}_\tau} \qquad 2.15$$

so that, from 2.13

$$\gamma \propto \bar{U}_\tau = k\bar{U}_\tau \text{ (say)} \qquad 2.16$$

Equation 2.10 may now be integrated with due consideration for the singularity at y=y' , to give

$$u_\gamma = \frac{\gamma}{\pi}\left[ - \ln \frac{y}{\Delta} + \ln \left( \sqrt{1 - \left(\frac{y}{\Delta}\right)^2} \right.\right.$$

$$= \frac{k\overline{U}_\tau}{\pi}\left[ - \ln \frac{y}{\Delta} + \ln \left( \sqrt{1 - \left(\frac{y}{\Delta}\right)^2} \right.\right] \qquad (2.17)$$

The second term on the right hand side above is significant only near the outer limit of the vortex sheet (i.e., near y =Δ). Consequently the self-induced streamwise velocities of the spanwise elements in the vortex system will have a distribution which is essentially logarthmic throughout most of the layer i.e.,

$$\frac{u_\gamma}{\overline{U}_\tau} = - \ln \frac{k}{\pi} \ln \frac{y}{\Delta} \qquad (2.18)$$

In view of its fundamental role in controlling the turbulent shear stress mechanism, which will shortly become clear, this distribution will be refered to as the INTRINSIC TURBULENT or simply the INTRINSIC velocity distribution. We note that it may also be expressed in the form of a 'law of the wall'.

$$\frac{u_\gamma}{\overline{U}_\tau} = - \frac{k}{\pi} \ln \frac{y\overline{U}_\tau}{\nu} + \frac{k}{\pi} \ln \frac{\Delta\overline{U}_\tau}{\nu} \qquad (2.19)$$

containing the parameter $\frac{\Delta\overline{U}_\tau}{\nu}$ .

While several gross assumptions and approximations are embodied in eq. 2.19, the functional form of the intrinsic distribution obtained is encouraging in the light of the observed logarithmic behaviour of the mean flow in the fully turbulent regime. However, a question now arises as to the relationship between this intrinsic profile and the primary motion which was credited earlier with the streamwise convection of the vortex structure. In this regard, it seems reasonable to expect that if the primary motion entering the vortex system conformed precisely to the intrinsic distribution, then no dynamic interaction involving streamwise momentum exchange should occur. If, however, as will generally be the case, there is some degree of mismatch between the intrinsic and entrant primary profiles, dynamic interaction accompanied by streamwise momentum and energy exchange between the primary flow and vortex system must evidently take place. As a result the primary velocity distribution will undergo a rapid change as it passes through the vortex structure.

In order to accomplish the exchange of mementum and consequent modification of the primary motion, the vortex structure must impose on the primary flow, an effective

shear stress gradient which we shall refer to as the vortex shear stress gradient. Then, in accord with the fundamental precept of the Instability Hypotheses, this gradient must account for the turbulent shear stress gradient experienced by the mean motion. Since the strength of the gradient is invariant in the transformation from the moving axis system $(x-\overline{U}_i t,y,z)$, to the conventional fixed reference frame $(x,y,z)$, the mean turbulent shear stress $\tau_T$ is simply the space average of the vortex shear stress $\tau_V$ taken over a complete development/breakdown cycle. Thus if the vortex shear stress is assumed to act over a portion $\lambda l_x$ of the complete cycle $l_x$ $(\lambda<<1)$,

$$\tau_T = \lambda \tau_V \qquad (2.20)$$

If this conclusion is correct, it is evident that

(1) the so-called turbulent shear stress is a highly intermittent phenomenon which is synchronized with the passage of vortex systems and thus would be recorded by a $u'v'$ hot-wire probe, for example, as extremely short bursts occuring with a characteristic mean frequency,

$$f = \frac{\overline{U}_i}{\overline{l}_x}$$

(2) the instantaneous magnitude of the stress when present, is perhaps several orders of magnitude higher than its mean value, $\tau_T$ (depending on the actual magnitude of $\lambda$ ).

Since the mean turbulent shear stress gradient exhibits both positive and negative values at any streamwise station, the corresponding vortex shear stress will also have both positive and negative values depending on y. Consequently, the vortex shear stress mechanism is such that the momentum, and hence the energy exchange between the primary motion and the vortex structure can and do occur in either direction; that is, the mechanism involved is reversible in the thermodynamic sense.

The crucial problem now concerns the extent to which the primary motion entering a particular vortex system is altered as a result of incompatibility with the intrinsic distribution of the system. Here we might be tempted to infer, in accord with the classical concept of wall turbulence, that this change is determined by the vortex shear stress gradient. This is precisely equivalent to the statement that the mean motion is governed by the turbulent shear stresses and merely rephrases the classical problem concerning the nature and

magnitude of turbulent shear stress.

However, when we take into consideration the fact that the interaction is caused in the first place by mismatch between the primary and intrinsic distributions, then we are led to precisely the opposite conclusion embodied in the following Compatibility Hypotheses.

"The nature of the interaction (that is, the magnitude and sense of the vortex shear stress gradient generated by the interaction) between the vortex system and primary motion is such that, irrespective of the entrant condition of the primary motion, the primary velocity distribution at exit is always identical to the intrinsic distribution." According to this hypothesis, the intrinsic profile, which is determined essentially by the local flow properties, provided a "master copy" to which the primary motion is periodically forced to conform. The development of the primary motion may thus be viewed as a conflict between the vortex interaction mechanism which seeks to establish and maintain the intrinsic (logarithmic) profile, and viscosity which, were it not for the repeated breakdown of the sublayer, would continue to alter the intrinsic profile until finally a laminar (Blasius) profile was established.

The so-called "turbulent shear stresses" now appear as a result of and not as the cause of the flow development: that is, the interaction mechanism is such that it generates precisely the vortex shear stress gradient required to impose the intrinsic distribution of velocity on the primary motion passing through the vortex system. This gradient and hence, throught equation (2.20), the turbulent shear stress gradient are thus governed by a combination of the intrinsic distribution and the effects of viscosity and pressure gradient which distort this distribution between successive vortex systems.

Since the mean motion is effectively determined once the intrinsic distribution and its subsequent distortion by viscosity and pressure gradient are known, it follows that neither consideration of the vortex shear stresses, nor of the mean "turbulent" shear stresses plays any role whatsoever in the solution of the mean motion. The need to determine the nature and magnitude of the turbulent shear stress, which is classically regarded as an essential step in the mean flow problem, is thus removed completely by the Compatibility Hypothesis. Turbulent shear stress is now seen merely as an "end product" of the flow mechanism and is correctly determined by the Reynolds' equations once the mean motion has been otherwise calculated.

However, while the vortex shear stresses play no governing role in determining the mean motion, they do impose real forces on the flow and effect an exchange of momentum and energy between vortex system and primary motion. In particular, as we shall see, they are primarily responsible for the fluctuating pressure field imposed on the wall, and consequently will be considered in some detail shortly.

The next step, however, is to consider the manner in which the primary motion develops between successive vortex systems.

## 2.5 The Primary Motion

If we neglect temporal variation associated with Reynolds' number growth, the primary motion, viewed in the moving-axis system ( $x - \overline{U}_i t$, $y,z$) comprises a steady motion which develops upstream from one vortex system to the next. On leaving each instability, the velocity distribution, according to the Compatability Hypothesis of section 2.4, has the intrinsic form of equation (2.19). As the motion develops "upstream", this distribution is progressively modified by the viscous shear stress gradient near the wall and by streamwise pressure gradient, if present. As suggested earlier, the action of the viscous shear stress gradient is to accelerate the primary motion close to the wall in the "upstream" direction. Positive (adverse) pressure gradient will also accelerate the primary flow in the "upstream" sense while negative pressure gradient will retard it. The influence of pressure gradient should be fairly uniform across the layer, except very close to the wall where the pressure gradient will be opposed directly by viscous stresses.

Thus after a complete development cycle the primary motion will enter the next vortex system "upstream" with increased velocities within the sublayer and velocities elsewhere either increased or reduced depending on the sign of the pressure gradient if one exists. The resultant mismatch between this developed profile and the intrinsic profile in the next vortex system will generate a vortex shear stress gradient which will have positive slope in the sublayer as deduced earlier, (see Figure 4b). Negative or positive pressure gradient will respectively provide negative or positive contribution to this gradient outside the sublayer. These statements are summarized below.

| Nature Of Influence On Developing Primary Motion | Effect On "Upstream" Primary Motion (Moving Axis System) | Region of Influence. | Contribution To Vortex and Mean Turbulent Shear Stress Gradients |
|---|---|---|---|
| Viscous Shear Stress Gradient | Accelerative, | Sublayer | Positive |
| Positive Pressure Gradient | Accelerative, | Mainly Outside Sublayer | Positive |
| Negative Pressure Gradient | Decelerative | Mainly Outside Sublayer | Negative |

These various influences, together with the effect of downstream (Reynolds number) growth, which will be considered later, combine to distort the intrinsic profile progressively "upstream" of one vortex system and hence establish the vortex shear stress gradient in the next system according to the degree of distortion produced.

We shall now obtain a first, simple solution for the developing primary motion considering first, the zero pressure gradient case. In so doing, it will be convenient to revert to the fixed axis system ( x,y,z) and to treat the primary motion accordingly as a time-dependent one. Physically, the problem is stated as follows:

At time t=o (say) the passage of a vortex system causes the primary motion at a fixed x– station to breakdown and revert to the intrinsic form which in the moving-axis

system was given by equation (2.19). This distribution transformed to the fixed-axis system provides the initial condition $u^*(0)$ of the time dependent primary motion, thus

$$u^*(0) = \overline{U}_i - u_\gamma$$
$$= \overline{U}_i + \overline{U}_\tau \frac{k}{\pi} \ln \frac{y}{\Delta}$$

or
$$\frac{u^*(0)}{\overline{U}_\tau} = \frac{k}{\pi} \ln \frac{y\overline{U}_\tau}{\nu} + \frac{\overline{U}_i}{\overline{U}_\tau} - \frac{k}{\pi} \ln \frac{\Delta\overline{U}_\tau}{\nu}$$

$$= A + B \ln \frac{y\overline{U}_\tau}{\nu} \text{ (say)} \qquad (2.21)$$

where
$$A = \frac{\overline{U}_i}{\overline{U}_\tau} - \frac{k}{\pi} \ln \frac{\Delta\overline{U}_\tau}{\nu} \qquad (2.22)$$

$$B = k = \text{constant} \qquad (2.23)$$

according to equation (2.16)

While little is known at this stage of the terms $\frac{\overline{U}_i}{\overline{U}_\tau}$ and $\frac{k}{\pi} \ln \frac{\Delta\overline{U}_\tau}{\nu}$ in equation (2.22) it is scarcely likely that they can be more than weakly dependent on Reynolds' number. We shall therefore treat both A and B as constants for the present, bearing in mind the possibility that A and indeed B may in practice exhibit some weak Reynolds' number dependency even in the case of constant pressure layers.

For $t>0$, the initial profile $u^*(0)$ will be progressively modified by viscosity until the arrival of the next vortex system at $t=T$ (where

$$T = \frac{\overline{I}_x}{\overline{U}_i} \qquad (2.24)$$

whereupon the primary motion again reverts to the initial intrinsic condition and the next cycle commences. We are thus concerned with the viscous time-dependent development of the primary motion $u^*$, subject to the following boundary conditions:

$$t=0\ , \qquad \frac{u^*}{\bar{U}_\tau} = A + B \ln \frac{y\,\bar{U}_\tau}{\nu} \qquad (2.25)$$

$$0<t \leq T,\ y = 0 \quad u^* = 0 \ (\text{zero slip condition}) \qquad (2.26)$$

and

$$y\to\infty, \qquad \frac{u^*}{\bar{U}_\tau} \to A + B \ln \frac{y\,\bar{U}_\tau}{\nu} \qquad (2.27)$$

in accord with the supposition that the influence of viscosity originates at and spreads outwards from the wall thus leaving the flow unaffected far from the wall at finite t.

In the light of the basic assumption that no significant interference occurs between the flows in adjacent instability bands, it seems reasonable to treat the developing primary motion essentially as a two-dimensional one governed by the viscous time-dependent boundary-layer equation

$$\frac{\partial u^*}{\partial t} + u^* \frac{\partial u^*}{\partial x} + v^* \frac{\partial u^*}{\partial y} = \nu \frac{\partial^2 u^*}{\partial y^2} \qquad (2.28)$$

and the continuity equation,

$$\frac{\partial u^*}{\partial x} + \frac{\partial v^*}{\partial y} = 0 \qquad (2.29)$$

We shall further simplify the problem at this stage by making

an assumption commonly employed in the analysis of impulsively generated motions; namely that at least for a short time following the initiation of the motion, the convective acceleration terms may be neglected in comparison with the temporal acceleration. With this assumption, equations (2.28) and (2.29) reduce to the diffusion equation

$$\frac{\partial u^*}{\partial t} = \nu \frac{\partial^2 u^*}{\partial y^2} \tag{2.30}$$

Equation (2.30), with the boundary conditions (2.25) - (2.27) has the solution

$$\frac{u^*}{\overline{U}_T} = \left( a + \frac{b}{4} \ln \frac{t}{T} \right) \int_o^h e^{-h^2}\, dh + b \int_o^h e^{-h^2} \int_o^h e^{+h^2} \int_o^h e^{-h^2}\, dh\, dh\, dh \tag{2.31}$$

where

$$h = \frac{y}{2\sqrt{\nu t}} \tag{2.32}$$

a and b are constants of integration and the periodic time, T, of the cycle is introduced for mathematical convenience.

An auxiliary relationship between a, b, and T is immediately obtained by invoking the mean shear stress relationship at the wall i.e.

$$\begin{aligned} \overline{\tau}_o &= \mu \left( \frac{d\overline{u}}{dy} \right)_{y=0} \\ &= \mu \left( \frac{\overline{du^*}}{dy} \right)_{y=0} \end{aligned} \tag{2.33}$$

Differentiating equation (2.31) with respect to y and evaluating at y = 0 we obtain

$$\left[\frac{\partial u^*/\overline{U}_\tau}{\partial y}\right]_{y=0} = \left[\frac{1}{2\sqrt{\nu t}}\left\{\left(a + \frac{b}{4}\ln\frac{t}{T}\right)e^{-h^2} + be^{-h^2}\int_o^h e^{+h^2}\int_o^h e^{-h^2}\,dh\,dh\right\}\right]_{y=0} = \frac{1}{2\sqrt{\nu t}}\left(a + \frac{b}{4}\ln\frac{t}{T}\right) \qquad (2.34)$$

then

$$\frac{\overline{\tau}_o}{\rho} \equiv \overline{U}_\tau^2$$

$$= \frac{\nu}{T}\int_o^T \left(\frac{\partial u^*}{\partial y}\right)_{y=0} dt$$

$$= \frac{\nu\overline{U}_\tau}{T}\int_o^T \frac{\left(a + \frac{b}{4}\ln\frac{t}{T}\right)}{2\sqrt{\nu t}}\,dt$$

$$= \left(a - \frac{b}{2}\right)\overline{U}_\tau\sqrt{\frac{\nu}{T}}$$

or

$$\overline{U}_\tau\sqrt{\frac{T}{\nu}} = \left(a - \frac{b}{2}\right) \qquad (2.35)$$

Noting that the second integral in equation 2.31 has the asymptotic form

$$\left[\int_0^h e^{-h^2} \int_0^h e^{+h^2} \int_0^h e^{-h^2}\, dh\, dh\, dh\right]_{h\to\infty} \longrightarrow \frac{\sqrt{\pi}}{4} \ln h + c \tag{2.36}$$

Where c is a constant whose value has been computed as 0.136, we obtain the asymptotic expression for the primary motion

$$\left[\frac{u^*}{\bar{U}_\tau}\right]_{h\to\infty} \longrightarrow \left(a + \frac{b}{4} \ln \frac{t}{T}\right) \frac{\sqrt{\pi}}{2} + b\left(\frac{\sqrt{\pi}}{4} \ln h + c\right)$$

$$= a \frac{\sqrt{\pi}}{2} + bc + b \frac{\sqrt{\pi}}{4} \ln H$$

$$= a \frac{\sqrt{\pi}}{2} + bc - b \frac{\sqrt{\pi}}{4} \ln\left(2\bar{U}_\tau \sqrt{\frac{T}{\nu}}\right)$$

$$+ b \frac{\sqrt{\pi}}{4} \ln \frac{y\bar{U}_\tau}{\nu} \tag{2.37}$$

where

$$H = \frac{y}{2\sqrt{\nu T}} \tag{2.38}$$

Since equation (2.37) does not contain t, it evidently also gives the form of the mean motion outside the sphere of influence of viscosity, that is, outside the sublayer.

We now obtain by comparison of equation (2.37) with the boundary condition (2.27),

$$A = a\frac{\sqrt{\pi}}{2} + bc - b\frac{\sqrt{\pi}}{4}\ln\left(2\,\overline{U}_\tau\sqrt{\frac{T}{\nu}}\right) \tag{2.39}$$

and

$$B = b\frac{\sqrt{\pi}}{4} \tag{2.40}$$

These two equations together with equation (2.35) permit evaluation of A,B, a, b and $\overline{U}_\tau\sqrt{\frac{T}{\nu}}$ when any two are known. Evidently $\overline{U}_\tau\sqrt{\frac{T}{\nu}}$ is a dimensionless stability parameter which must be determined from an appropriate stability analysis of the primary motion, while B(=k) clearly is a measure of the strength of the vortex system (see equation 2.16) and must be determined from a detailed consideration of the process of vortex generation controlled by the sublayer instability. Both these calculations, however, are outside the scope of the present simple model and must await a more rigorous treatment of the problem. For present purposes, therefore, the various constants will be determined empirically by ascribing to A and B values consistent with the experimentally determined logarithmic law of the wall. The specific values assigned to A and B will be those suggested by Coles[11] i.e.

$$\begin{aligned} A &= 5.1 \\ B &= 2.5 \end{aligned} \tag{2.41}$$

(The precise choice of values does not significantly affect the present analysis). With these values we obtain from equations (2.39), (2.40) and (2.35),

$$a = 13.6 \tag{2.42}$$

$$b = 5.64 \tag{2.43}$$

and

$$\overline{U}_\tau \sqrt{\frac{T}{\nu}} = 10.7 \tag{2.44}$$

We now obtain the mean motion as

$$\frac{\overline{u}}{\overline{U}_\tau} = \frac{1}{T}\int_0^T \left(\frac{u^*}{\overline{U}_\tau}\right) dt$$

$$= \frac{1}{T}\int_0^T \left[ (a + \frac{b}{4} \ln \frac{t}{T}) \int_0^h e^{-h^2}\, dh + b \int_0^h e^{-h^2} \int_0^h e^{h^2} \int_0^h e^{-h^2}\, dh\, dh\, dh \right] dt$$

$$= (a - \tfrac{3}{4} b) \left[ (1 + 2H^2) \int_0^H e^{-h^2} dh + He^{-H^2} - H^2 \sqrt{\pi} \right]$$

$$+ b \left[ (1 + 2H^2) \int_0^H e^{-h^2} \int_0^h e^{h^2} \int_0^h e^{-h^2}\, dh\, dh\, dh \right.$$

$$+ He^{-H^2} \int_0^H e^{h^2} \int_0^h e^{-h^2}\, dh\, dh - 2H^2 (c + \frac{\sqrt{\pi}}{4} \ln H)$$

$$\left. + \tfrac{1}{2} \int_0^H e^{-h^2}\, dh \right] \tag{2.45}$$

and note that it has the same asymptotic form as the primary motion at large distances from the wall, i.e.

$$\left[\frac{\overline{u}}{\overline{U}_\tau}\right]_{H \to \infty} \longrightarrow a \frac{\sqrt{\pi}}{2} + bc + b \frac{\sqrt{\pi}}{4} \ln H \tag{2.46}$$

in agreement with equation (2.37). The distribution of primary velocity and mean velocity, determined from equations (2.31) and (2.45) with the values of a,b, and $\overline{U}_\tau \sqrt{\frac{T}{\nu}}$ as given in equations (2.42) - (2.44) are plotted respectively in Figures 9 and 10.

The curves are presented in the familiar 'Law of the Wall' form making use of the relationships,

$$h = \frac{y}{2\sqrt{\nu t}} = \frac{y\,\overline{U}_\tau}{\nu} \quad \frac{1}{2\overline{U}_\tau \sqrt{\frac{T}{\nu}}} \quad \frac{1}{\sqrt{\frac{t}{T}}} \tag{2.47}$$

and

$$H = \frac{y}{2\sqrt{\nu T}} = \frac{y\overline{U}_\tau}{\nu} \quad \frac{1}{2\overline{U}_\tau \sqrt{\frac{T}{\nu}}} \tag{2.48}$$

It is seen that the time-dependent primary profile exhibits a progressive distortion of the initial intrinsic (logarithmic) profile, which originates at the wall and spreads steadily outwards. The primary velocities steadily decrease with time near the wall (corresponding to an "upstream" acceleration of the flow when viewed in the moving-axis system, as deduced earlier). If we now formally redefine the sublayer as that region within which measurable viscous distortion of the initial intrinsic profile occurs within the development period T, (say, for example, at least 1% change in velocity) then it is seen from Figure 9 that the sublayer thickness $\delta_s$ is obtained as

$$\frac{\delta_s \overline{U}_\tau}{\nu} \doteq 50 \tag{2.49}$$

The mean velocity distribution, shown if Figure 10,

displays excellent agreement with the tabulated experimental data of Coles (11) throughout the entire sublayer, so-called blending region* and fully turbulent regime.

To complete this preliminary analysis of the primary motion, the effects of streamwise pressure gradient will now be determined. The appropriate governing equation in this case is

$$\frac{\partial u^*}{\partial t} = \nu \frac{\partial^2 u^*}{\partial y^2} - \frac{1}{\rho} \frac{dp}{dx} \tag{2.50}$$

Since this equation is linear, we may write

$$u^* \left(\frac{dp}{dx}\right) = u^*(0) + \Delta u_p^* \tag{2.51}$$

where the pressure gradient contribution $\Delta u^*_p$ is obtained as a solution of equation (2.50) with the boundary conditions,

$$t = 0, \quad \Delta u^*_p = 0 \tag{2.52}$$

$$0 < t \leq T \quad y = 0, \quad \Delta u^*_p = 0 \tag{2.53}$$

$$y \to \infty \quad \Delta u^*_p \to \frac{t}{\rho} \frac{dp}{dx} \tag{2.54}$$

The last boundary condition arises from the fact that the viscous term in equation (2.50) becomes negligibly small at large y

*The new definition of sublayer thickness proposed herein, makes the definition of a blending region unnecessary and indeed the concept of viscous and turbulent stresses 'blending' is no longer meaningful if the present theory is accepted.

so that the equation has the simple asymptotic solution given by equation (2.54). This boundary condition further suggests that we seek a solution of the form

$$\Delta u^*_p = - \frac{t}{\rho} \frac{dp}{dx} f(h) \tag{2.55}$$

such that

$$f(0) = 0$$

and

$$f(\infty) = 1 \tag{2.56}$$

We thus obtain the equation

$$f(h) - 1 - \frac{h}{2} f'(h) - \tfrac{1}{4} f''(h) = 0 \tag{2.57}$$

which has the solution

$$f(h) = \frac{2}{\sqrt{\pi}} \left[ (1 + 2h^2) \int_o^h e^{-h^2} dh - \sqrt{\pi}\ h^2 + h e^{-h^2} \right] \tag{2.58}$$

so that from equation (2.55)

$$\frac{\Delta u^*_p}{\overline{U}_\tau} = - \frac{t}{T} .P. \frac{\overline{U}_\tau^2 T}{\nu} \cdot \frac{2}{\sqrt{\pi}} \left[ (1 + 2h^2) \int_o^h e^{-h^2} dh - \sqrt{\pi} h^2 + h e^{-h^2} \right] \tag{2.59}$$

where P is the pressure gradient parameter defined as

$$P = \frac{\nu}{\rho \overline{U}^3_\tau} \frac{dp}{dx} \tag{2.60}$$

and $\frac{\overline{U}_\tau^2 T}{\nu}$ is the square of the stability parameter defined earlier.

Equation (2.59) yields a distribution which increases monotonically from the wall out and attains a constant asymptotic form

$$\left[\frac{\Delta u_p^*}{\overline{U}_\tau}\right]_{h\to\infty} \longrightarrow -\frac{t}{T} \cdot P \cdot \frac{\overline{U}_\tau^2 T}{\nu} \tag{2.61}$$

We need only consider here the asymptotic value of the pressure gradient contribution to the mean motion. This value is attained approximately within the sublayer thickness so that outside the sublayer, the mean pressure gradient term $\Delta\overline{u}_p$ is given by

$$\left[\frac{\Delta\overline{u}_p}{\overline{U}_\tau}\right]_{y > \delta_s} = \left[\frac{\Delta u_p^*}{\overline{U}_\tau}\right]_{y > \delta_s} = -\frac{P}{2}\frac{\overline{U}_\tau^2 T}{\nu} \tag{2.62}$$

Consequently, positive pressure gradient provides a negative contribution to the primary and mean motions in the fixed-axis system, and hence a positive contribution to the primary motion as viewed in the moving-axis system. This contribution to the mean motion alters the constant A in the fully turbulent region by the amount $-\frac{P}{2}\frac{\overline{U}_\tau^2 T}{\nu}$ so that:

$$\frac{\overline{u}}{\overline{U}_\tau} = \left(A - \frac{P}{2}\frac{\overline{U}_\tau^2 T}{\nu}\right) + B \ln \frac{y\overline{U}_\tau}{\nu} \tag{2.63}$$

The quantity $-\frac{P}{2}\frac{\overline{U}_\tau^2 T}{\nu}$ is generally small compared with A. (For example, a pressure gradient in which the freestream velocity falls from (say) 200 to 100 ft/sec in 5 feet with a mean $\overline{U}_\tau$ of 5 ft/sec and $\nu = 1.4 \times 10^{-4}$ ft$^2$/sec yields a value of $P \approx -0.022$ which, with $\overline{U}_\tau \sqrt{\frac{T}{\nu}} = 10.7$, increases the constant in the logarithmic law by 0.26). However, the intense local pressure gradient imposed on the boundary layer in the vicinity of shock systems and steps in supersonic flow may result in much larger values of this increment.

The total distortion of the intrinsic profile effected by the pressure gradient over a complete cycle is twice the mean incremental velocity, i.e.

$$\frac{\Delta u^*_P}{\overline{U}_\tau} = -P\frac{\overline{U}_\tau^2 T}{\nu} \qquad (2.64)$$

This quantity determines the contribution of the pressure gradient to the vortex shear stress gradient within the next vortex system and hence to the mean turbulent shear stress gradient.

We shall now complete the preliminary analysis of the primary motion by considering briefly the effect of downstream (Reynolds' number) growth. Consider, therefore, in the fixed-axis system (x,y,z) the passage of a particular vortex system past a fixed x-station, $x_o$, at time $t_o$ (say). Subsequently the vortex system moves downstream with velocity $\overline{U}_i$, while a fluid particle initially at $(x_o,y)$ will move downstream with velocity $u^* < \overline{U}_i$, ( random, turbulent velocity fluctuations are here neglected) where $u^*$ initially has the intrinsic value given by

$$\frac{u^*}{\overline{U}_\tau} = A + B \ln \frac{y\overline{U}_\tau}{\nu} \quad . \qquad (2.65)$$

If we omit the sublayer from our consideration, the viscous shear stress gradient acting on the particle will be negligibly small, while, as we have seen, the effect of moderate pressure gradient is weak, so that the particle will continue to travel downstream at almost constant velocity until it is overtaken by the next vortex system. This will occur, as indicated in Figure 11 at a point x given by

$$\frac{(x - x_o)}{u^*} = \frac{x - x_o + \bar{l}_x}{\overline{U}_i} = \frac{x - x_o}{\overline{U}_i} + T \qquad (2.66)$$

It is now evident that since the velocity of the particle has not changed significantly since leaving the station $x_o$, it will not match the intrinsic velocity of the second vortex system which is governed by the local wall shear stress. In travelling from $x_o$ to x, the strength of the intrinsic profile will change by an amount $\Delta u^*$ given by

$$\begin{aligned}\Delta u^* &= u^*(x) - u^*(x_o) \\ &= \overline{U}_\tau(x)\left(A + B\ln\frac{y\overline{U}_\tau(x)}{\nu}\right) - \overline{U}_\tau(x_o)\left(A + B\ln\frac{y\overline{U}_\tau(x_o)}{\nu}\right)\end{aligned} \qquad (2.67)$$

In the case of constant pressure layers, for example, $\overline{U}_\tau(x) < \overline{U}_\tau\ x_o)$ since $x > x_o$, and hence the quantity $\Delta u^*$ will be negative, that is to say, the particle will have excess downstream velocity (relative to the intrinsic profile) when it is overtaken by the second vortex system. The resultant vortex shear stress gradient generated will thus have negative slope as in the case of negative pressure gradient. Since equations (2.66) and (2.67) indicate that the distance

traveled by a fluid particle between successive encounters with vortex systems, and hence the excess velocity $\Delta u^*$, increases with increasing $u^*$, it follows that $\Delta u^*$must increase with y. Consequently the resultant negative contribution to the vortex and mean turbulent shear stress gradients will be strongest in the outer region of the flow. We can now complete the table of section 3, by including the influence of Reynolds number growth as follows

**Table A**

| Nature Of Influence On Developing Primary Motion | Effect On 'Upstream' Primary Motion In Moving Axis System | Region Of Influence | Contribution To Vortex and Mean Turbulent Shear Stress Gradient |
|---|---|---|---|
| Viscous Shear Stress Gradient | Accelerative | Sublayer | Positive |
| Positive Pressure Gradient | Accelerative | Mainly Outside Sublayer | Positive |
| Negative Pressure Gradient | Decelerative | | Negative |
| Reynolds' Number Growth | Decelerative | Increases Toward Edge of Boundary Layer | Negative |

Thus the actual mean turbulent shear stress gradient at any station is determined by a combination of the influences tabulated above.

In passing, it may be noted that equation (2.66) provides an interesting explanation of the large observed variation across the layer of the time of response of the flow to artificially induced disturbances. Klebanoff and Diehl,[15] for example, found that while a disturbance introduced near the wall disappeared within a relatively short distance downstream, a similar disturbance produced in the outer region of the flow persists over much longer distances extending possibly over many boundary layer thickness. According to the present model, a disturbance introduced at any point in the flow will remain relatively undisturbed until overtaken by the next vortex system, which according to the Compatability Hypothesis will remove <u>any</u> local departure from the intrinsic profile. The furtherest distance $\hat{\Delta x}$ over which a disturbance at any y can persist without encountering a vortex system is given by equation (2.66) as

$$\hat{\Delta x} = \frac{T}{\frac{1}{u^*} - \frac{1}{\overline{U}_i}} = \frac{u^* \overline{U}_i T}{\overline{U}_i - u^*} \qquad (2.68)$$

It is seen that $\hat{\Delta x}$ varies from zero at the wall ($u^* = 0$) to $\infty$ at the point at which $u^* = \overline{U}_i$ thus explaining in principle the large variation in flow response time.

## 2.6 The Vortex Shear Stress Mechanism

While a detailed analysis of the interaction between the primary motion and the vortex system is beyond the scope of this preliminary flow model, some insight into the nature of the vortex shear stress mechanism can be gained by invoking a simple aerodynamic analogy. It is apparent that from a kinematic viewpoint, the generation of each horseshoe element and its subsequent interaction with the primary motion is very similar to the initiation and development of circulation around a finite airfoil. This analogy is first explored in Figure 12 from a two-dimensional standpoint (for reasons which will become apparent, the flow around an airfoil at negative angle of attack is considered). If the flow around such an airfoil is inviscid, the potential flow field illustrated in Figure 12a is established and the airfoil experiences no net aerodynamic force. For the sake of completeness, it may be noted that this case is analogous to that in which the primary motion suffers no instability or breakdown and hence no vortex shear stress.

In a real fluid, however, the flow around the airfoil cannot negotiate the sharp trailing edge as required by the poential solution and consequently separates there, thus creating a starting vortex (Figure 12b). Since the net vorticity must remain zero, bound vorticity of equal strength but opposite sense is simultaneously established around the airfoil. This process is precisely analogous to that involved in the generation of the

inner and outer spanwise vortices by the sublayer instability (see Figure 4c). Subsequent to the initiation process, the starting vortex in the airfoil case, and the inner vortex in the boundary layer are convected away downstream leaving vorticity bound, in one case to the airfoil and, in the other, to the spanwise vortex front (Figure 12c).

If the airfoil has finite span, the bound and starting vortices are linked by trailing elements to form a closed system in accord with Helmholz's requirement relating to the continuity of vortex lines in a fluid. This system is then very similar to the ring or horseshoe elements which comprise the proposed vortex structure in the boundary layer case (Figure 12d).

So far, the analogy has concerned only kinematic aspects of the flow fields around the airfoil and horseshoe elements. In considering the dynamics of the respective systems, care must be taken since vortices, unlike lifting surfaces, cannot of themselves support aerodynamic loads. For the moment, however, we shall ignore this difficulty and assume that we can, for analytical purposes, treat the spanwise elements in the horseshoe vortices as equivalent lifting surfaces of identical span and circulation; and that we can consequently, draw valid conclusions regarding the dynamic interaction between the primary motion and vortex structure.

Let us then consider the case of finite lifting airfoil fixed in a flow whose velocity relative to the airfoil is $U_{Rel}$ (Figure 13a). At the location of the airfoil, the trailing vortex

system induces a vertical component of velocity, $\vec{v}_y$ which compounds with $\vec{U}_{Rel}$ to produce an effective velocity vector $\vec{U}_{EFF}$ and effectively reduces the angle of attack of the airfoil. As a result, the resultant force vector is tilted rearwards to provide an induced drag component $D_i$ parallel to the relative flow, $\vec{U}_{Rel}$ as well as a normal lift component, L. The energy lost by the free-stream at the rate $D_i U_\infty$ is transferred to the trailing vortices and hence transported downstream from the airfoil as rotational energy.

It is important to note that this process of energy transfer is irreversible <u>not</u> because the energy in the trailing vortices is irrecoverable in the thermodynamic sense, but merely because the vorticity thus created is continuously blown away from the airfoil. The elementary ring or horseshoe vortex in the vortex structure has the important difference that the trailing vortices are merely stretched, and not convected by the basic flow, so that, if viscous diffusion is neglected during their relatively short lifetime, they are to be considered as conservative rather than dissipative systems from an energy viewpoint. We shall see now that this conservative property makes possible energy transfer in either direction between the vortex system and the primary motion. We shall consider two specific cases; first, that in which the primary motion enters the vortex structure with velocity greater than the local intrinsic velocity of the system, and secondly, that in which the entrant velocity is less than the intrinsic value.

In considering the dynamic interaction involved in each of these cases by analogy with the flow around the finite airfoil, we note that even when the flow is viewed in the moving axis system $(x - \bar{U}_i t, y, z)$ in which the vortex structure is fixed, the individual spanwise elements are in motion under the combined inductive effect of their trailing elements and the other spanwise elements. As explained earlier, this inductive effect translates the elements "upstream" with velocity $u_\gamma$ and away from the wall with velocity $v_\gamma$. In order to analyze the primary flow past the spanwise elements on a quasi-steady basis, we choose an axis system fixed in these elements, i.e. the system $\left[(x-\bar{U}_i t + u_\gamma t)\ (y- v_\gamma t)\ z\right]$. To obtain the relative motion $U_{Rel}$ past the element, we therefore compound the primary motion entering the vortex system, $\left[\overline{\bar{U}_i - u^*(T)}\right]$, with the induced velocities $-\vec{u}_\gamma$ and $-\vec{v}_\gamma$ as shown for each case considered in Figures 13b and 13c. Finally, we obtain the effective velocity vector, $\vec{U}_{EFF}$, as in the airfoil case previously considered, by compounding $\vec{U}_{Rel}$ with the velocity induced by the trailing vortices, $\vec{v}_\gamma$. In each case, we note that the relative velocity $U_{Rel}$ carries the primary motion from the downstream side to the upstream side of the vortex system as required. However, in the first case (Figure 13b) in which the entrant velocity is greater than the intrinsic value $(\bar{U}_i - u^*(T) > u_\gamma)$ $U_{Rel}$ is directed "upstream" and towards the wall, while in the second case (Figure 13c) in which $\bar{U}_i - u^*(T) < u_\gamma$, it is directed "downstream" and towards the wall. The corresponding effective velocity vectors, $\vec{U}_{EFF}$, are parallel to the wall, being directed "upstream" in the first

case and "downstream" in the second. Of particular significance is the fact that the magnitude of the effective velocity is equal to the difference between the entrant primary velocity and the intrinsic velocity, i.e.

$$U_{EFF} = (\overline{U}_i - u^*(T)) - u_\gamma \qquad (2.69)$$

We now invoke the analogy with the finite lifting surface as proposed, and obtain the resultant force per unit-span on the spanwise element as

$$R = \rho U_{EFF} \Gamma \qquad (2.70)$$

We are principally concerned, however, with the reaction (-R) which this force imposes on the primary motion and, in particular, with the components $F_n$, $F_s$ of this reaction normal to and parallel to the relative velocity $U_{Rel}$.

In each case considered, the normal reaction $F_n$, (which corresponds to the lift reaction imposed by the finite airfoil on the flow around it) does no work on the primary motion but merely deflects it as it passes through the frontal vortex sheet. The component $F_s$, however, acts parallel to the relative motion and hence effects an energy transfer to or from that motion, as it passes through the vortex system. In the first case (Figure 13b) in which the primary motion enters the vortex system with excess velocity ($\overline{U}_i - u^*(T) > u_\gamma$), the reaction component $F_s$ works against the primary motion to abstract energy from it and hence decelerate it. The energy thus abstracted must clearly feed into the horseshoe

vortex, and because of the conservative nature of that system, must increase its strength, $\Gamma$ . The primary motion emerging "upstream" from the vortex system with reduced energy will attribute this loss of energy to the action of a shear stress gradient within the vortex structure, i.e. to the action of the vortex shear stress gradient as hypothesised earlier. In this case the vortex shear stress gradient (and hence mean turbulent shear stress gradient) is positive, the mechanism involved being analogous to the induced drag mechanism on the finite lifting airfoil.

In the second case, however $(\overline{U}_i - u^*(T) < u_\gamma)$ the parallel reactive component $F_s$ acts <u>with</u> the primary motion to increase its energy flux as it passes through the vortex sheet, and thus effectively provides negative vortex and turbulent shear stress gradient. This energy is supplied to the primary motion at the expense of the strength of the vortex element, a process corresponding to the impossible case of 'induced thrust' in the analogous airfoil system.

As noted earlier, the foregoing argument, while kinematically valid, is not acceptable as it stands since the spanwise vortex elements cannot of themselves support the aerodynamic loads required of the model. This difficulty is easily removed, however, and the kinematic validity of the model retained, if it is postulated that the reactive stresses on the primary motion are applied instead by local static pressure gradients established by the vortex system. This step, it should be noted is only made possible

by the fact that the required resultant stress vectors (as seen in Figures 13b and 13c) are always normal to the wall. Thus while these stresses cannot be supported directly by the spanwise vortices, they can be supported indirectly by the wall directly beneath the vortices, through the medium of a normal static pressure gradient of suitable strength and sense. Thus in the case where the entrant primary motion is greater than the intrinsic value at some distance from the wall (as in Figure 13b), the static pressure directly below the spanwise vortex increases towards the wall to provide the required reactive stress directed away from the wall. In the other case (Figure 13c) in which the entrant primary velocity is less than the local intrinsic value, the pressure below the spanwise vortex concerned decreases towards the wall to provide a reactive stress on the primary motion directed towards the wall. The foregoing statements imply the existence of a characteristic pressure field in the vicinity of the vortex structure and, in particular, of a characteristic pressure distribution on the wall immediately beneath the vortex system. The nature of this pressure field will be examined in the next section.

The tentative argument developed in the present section provides qualitative support for the Compatability Hypothesis in that it presents a plausible mechanism whereby the energy of the primary motion is increased or decreased by interaction with the vortex system in proportion to the difference between the entrant primary velocity and the local intrinsic velocity. The Hypothesis, however goes beyond this in asserting that the energy transfer is

such that the primary motion emerges from the vortex system with precisely the intrinsic distribution of velocity, irrespective of the entrant condition. Confirmation of this statement must await a more detailed analysis of the interaction phenomenon. While the present preliminary study considered the primary flow past discrete vortex elements, it would seem that a detailed analysis should treat the vortex structure as a homogeneous vortex sheet as suggested earlier. Such an analysis would bear interesting comparison with that relating to compressible flow through an inclined shock.

To summarize the present section, it is concluded that the non-viscous transfer of momentum within the layer, which the mean motion experiences as a turbulent shear stress gradient, is achieved by the horseshoe elements within the vortex structure in much the same way as a finite lifting surface imposes an induced drag on the flow past it. These vortices, which cannot of themselves support or impose forces on the flow, effectively utilize the wall directly beneath them as a composite finite airfoil or lifting surface to impose the required stresses on the primary motion across the entire boundary layer. This "remote" application of stress by the wall is achieved through the medium of intense normal pressure gradients which result in a characteristic pressure signature on the wall beneath the vortex system. Thus, in a sense, the "secret" of turbulent wall shear flow lies in its ability to transfer momentum from wall to flow not only through the action of tangential viscous shearing stresses at the wall but also through the normal pressure field on the wall. In this sense the role of the vortex systems is twofold; first, to establish intense localized normal

pressure gradients and secondly to deflect and steer the local primary flow through these pressure gradients in such a way that they abstract energy from it or supply energy to it as required. In the light of this physical picture, the wall pressure field below turbulent shear flow can no longer be regarded merely as an end product of random, turbulent motions characteristic of the shear layer. Instead, it plays (at least in part) a dominant role in the non-viscous momentum transfer mechanism. Since this mechanism, according to the theory, is a relatively well-organized one with characteristic frequency and length scales, it follows that that part of the wall pressure field directly related to this mechanism must exhibit the same degree of order. Finally, it seems intuitively obvious that since the organized vortex structures must account for a major portion of the total energy contained in the unsteady motions within the layer, most of the energy in the wall pressure field will likewise be contained in those components directly related to the momentum transfer mechanism. The theory thus offers hope in particular of an essentially deterministic approach to the analysis of the wall pressure field. This possibility is explored further in the next section.

As mentioned earlier, there are certain fundamental similarities between the present model of wall turbulence and that proposed by Theodorsen.[12] While a detailed discussion of the relationship between the two models lies outside the scope of the present study, it is worth noting briefly the principal similarities

and dissimilarities between the two physical pictures developed.

The horseshoe vortices in each case result from an inherent instability in the basic shear flow. They originate in planes essentially normal to the basic flow and subsequently stretch outwards and downstream so that their planes rotate to present a steadily decreasing angle with the wall. The rotational sense of each vortex is the same so that a strong associated outflow of fluid from the wall occurs within it. The vortex systems in each model are distributed uniformly over the wall, and in each case they undergo a finite life cycle of growth and decay. However, whereas Theodorsen's turbulence 'units' comprise a single vortex each, the vortex structure in the present model contains a number of vortex elements at any given time, and while each of these elements has a comparatively short lifetime, the structure as a whole is maintained for much longer periods by the continuous creation of new elements which replace the older members.

Theodorsen's vortices are stretched downstream and outwards by lift and drag forces generated by the relative motion between the spanwise element of the horseshoe and the basic flow which has a velocity higher than that of the element. In the present model, the outward and streamwise motion of the spanwise front of each horseshoe vortex is self-induced by the vortex structure itself. The relative velocity between the basic flow and the vortex front at any point in the layer can and does

have either positive or negative sense and the associated 'lift' and 'drag' forces are correspondingly positive or negative to provide either positive or negative turbulent shear stress as required. Despite these significant differences, however, there are clearly fundamental similarities between the two models which warrent further study elsewhere.

## 2.7 THE WALL PRESSURE SIGNATURE OF THE VORTEX SYSTEM

In order to establish more precisely the nature of the wall pressure signature of the vortex system, it is useful to summarize in tabulated form the following principle features of the vortex shear stress mechanism.

| Vortex and Turbulent Shear Stress Gradients | Primary Velocity Entering Vortex System | Primary Energy Change Through Vortex System | Local Change in Strength of Vortex Elements | Local Normal Pressure Gradient Generated by Interaction | Resultant Contribution to Wall Pressure Relative to Ambient Pressure |
|---|---|---|---|---|---|
| 0 | $=u_\gamma$ | 0 | 0 | 0 | 0 |
| + | $>u_\gamma$ | - | + | - | + |
| - | $<u_\gamma$ | + | - | + | - |

We will now assume for the moment that the vortex shear stress goes to zero at the outer edge of the vortex front (this will not generally be the case, as discussed in the next section, but the assumption permits a simple first approach to the study of the wall pressure signature). Then if the vortex front were normal to the wall, the local variation in pressure across the layer $-\frac{\partial p}{\partial y}$, required to effect the necessary momentum and energy exchange as described in the previous section, would simply integrate to zero from y=0 to y=$\Delta$, (since the corresponding integral of the vortex shear stress gradient is zero) and hence would provide no net contribution to the pressure on the wall directly beneath the front. The vortex front,(i.e. the characteristic path

of the spanwise elements,) slopes "upstream" from the generating instability in the sublayer, so that each y-point in the front corresponds to a different, $(x-\bar{U}_i t)$ point on the wall directly below it. If we consider any short segment of the vortex path, as shown in Figure 14a, then the pressure load over its projected area on the wall directly below will, according to the present argument, be equal to that aerodynamic load which the equivalent finite lifting surface would sustain if it replaced the spanwise vorticity over that segment of the front. The reactive force is transmitted to the primary flow passing through the segment by a normal pressure gradient between the segment and its projection on the wall, the sense of which is determined qualitatively from the table above (a more detailed analysis would provide a quantitative relationship between the various quantities listed in that table). As indicated in the table, the strength of the pressure gradient and hence the pressure on the wall below the segment is governed by the local mismatch between the primary and intrinsic velocities and is therefore directly related to the mean turbulent shear stress gradient at that point.

We can now sketch a typical pressure signature, as in Figure 14b, from a knowledge of the turbulent shear stress distribution, the geometry of the vortex front, and the qualitative relationships expressed in the table. In a typical well-behaved layer, the turbulent shear stress increases rapidly from the wall, exhibiting maximum positive gradient just within the sublayer and attaining maximum value just outside it. Because of the small ratio of sublayer thickness to boundary layer thickness, that

portion of the wall under the corresponding portion of the vortex front will be small in relation to the total projected area of the front. Over this short section of the wall immediately "upstream" of the instability, the pressure, according to the above table, will rise rapidly above ambient (freestream) value to a maximum at that point corresponding (via the vortex front geometry) to the point of maximum turbulent shear stress gradient, and then will fall rapidly to the ambient value at the point on the wall corresponding to the point of maximum turbulent shear stress (zero gradient). The wall pressure will then fall below the ambient value, with increasing distance upstream, but at a much lower rate (since the turbulent shear stress gradient beyond the point of maximum shear is relatively weak). The pressure will attain a minimum value at that point corresponding to minimum shear stress gradient, and subsequently rise to the ambient value at a point below the outer extremity of the vortex sheet. It should be noted that this pressure distribution is entirely consistent with the kinematic character of the primary flow in the vicinity of the vortex system; the "downstream" positive pressure region will deflect the primary motion near the wall outwards in the form of a coherent eruptive jet, while the weaker, longer, negative portion of the field will pull the flow back parallel to the wall in the outer region of the layer.

While the foregoing picture is undoubtedly oversimplified, it does provide some useful insight into the fundamental

structure of the wall pressure field. First, it suggests that the wall pressure, like the turbulent shear stress, should scale basically on the wall shear stress, $\overline{\tau_o}$ Secondly, it suggests that the distribution of pressure over the wall beneath the vortex structure will be related to the local distribution of turbulent shear stress gradient across the layer as indicated in Figure 14 b (although this relationship is clearly complicated by the strength distribution and geometry of the vortex front which provides the linking mechanism between the wall pressure and the shear stress distributions.) Thirdly, it indicates that the height, $\Delta$, of the vortex structure (identified, for the present, with the boundary layer thickness, $\delta$,) will play some role in determining the strength of the pressure signature (we shall return to this question later). Finally, it indicates clearly the general effect of pressure gradient on the pressure signature.

To determine the effect of pressure gradient, consider three boundary layers of the same thickness, having zero, negative and positive streamwise pressure gradients respectively (Figure 15). It is readily seen that the lower values of turbulent shear stress and shear stress gradient in the case of negative pressure gradient will generate a relatively weak pressure signature on the wall, while positive pressure gradient will increase the strength of the pressure signature relative to the zero-pressure gradient case.

Thus, it may be concluded that the pressure signature

imposed on the wall by the vortex shear stress mechanisms will be governed broadly by the local wall shear stress $\overline{\tau}_o$, the local height of the vortex system, $\Delta$, and the local streamwise pressure gradient parameter which ( we may infer from eq. 2.60 ) is $\frac{\nu}{\rho \overline{U}_\tau^3} \frac{dp}{dx}$ The precise form of the pressure signature will depend on the form of the local turbulent shear stress distribution, and on the strength and geometry of the vortex front.

## 2.8 The Outer Flow Mechanism

In the simple vortex model examined in the previous section, it was assumed that the vortex shear stress decreased to zero at the outer edge $\Delta$ of the vortex front. In general, this will not be the case. The actual residual vortex shear stress at $y = \Delta$ will depend, as can be seen from table **A** , on the relative magnitudes of

1. the viscous shear stress gradient near the wall,
2. the streamwise pressure gradient, if one exists, and
3. the Reynold's number growth effect described in section 2.5.

The last of these effects is very weak in comparison with that of the viscous shear stress gradient which provides the basic positive contribution to the vortex shear stress gradient. Consequently, in the absence of pressure gradient, there will be a residual positive vortex shear stress at $y = \Delta$ . Positive pressure gradient will increase this residual value, since its contribution to the vortex shear stress gradient is also positive. Negative pressure gradient will reduce the residual shear stress, and if precisely tailored to the boundary layer development, will completely remove it to provide a "closed solution" to the flow in the vicinity of the

vortex structure. This occurs in the special case of pipe and channel flow in which the favorable pressure gradient precisely balances the mean shear stress gradient. It could also occur in boundary layers with strong negative pressure gradient. Such special "closed" flows will exhibit no outer or "wake" mechanism because the residual vortex shear stress vanishes at the edge of the layer and thus no additional "smoothing" process is required to remove it. In such cases (see figure 16a) the strength of the horseshoe vortex elements will also vanish at the edge of the layer, implying a delicate balance between the rate at which they gain energy from the primary motion in the region of positive vortex shear stress gradient near the wall; the rate at which they feed energy back into the primary motion through the remainder of the layer, and the rate at which they lose energy to turbulence production and viscous dissipation. As indicated in the previous section, the mean signature pressure in such cases will be zero.

In general, however, there will be a residual vortex shear stress at $y = \Delta$, which must be removed by some additional mechanism to satisfy the condition $\overline{\tau} = 0$ outside the layer. We obtain a clue as to the nature of this mechanism from the knowledge that a residual vortex shear stress will be accompanied by residual energy in the horseshoe vortices as they reach $y = \Delta$, and consequently, a residual outflow of fluid

at that point. If we consider a control volume enclosing and fixed relative to the entire vortex system (i.e., extending from the wall to $y = \Delta$ ) it is evident that since the net change in primary momentum flux through the volume is precisely balanced by the residual vortex shear stress, the outflow can carry no streamwise momentum outside the volume. It thus follows that the local intrinsic velocity $u_\gamma$ at $y = \Delta$ must be zero (as already satisfied by equation 2.18), and furthermore, that the wave velocity of the instability and associated vortex over the wall must be given (from equation 2.21) by

$$\frac{\bar{U}_i}{\bar{U}_\tau} = A + B \ln \frac{\Delta u_\gamma}{\nu} \qquad (2.71)$$

We also note that the y- momentum carried out of the volume by the outflow at $y = \Delta$ , is balanced by the residual pressure in the signature on the wall beneath the vortex. This residual pressure, averaged over the complete development/breakdown cycle, accounts for the outflow of the mean motion associated with the local rate of growth of the layer.

It is now apparent that the residual vortex shear stress is finally "removed" by the momentum drag which the outflow imposes on the freestream. The magnitude of this drag per unit width of layer, $D_\Delta$ , will be

$$D_\Delta = \rho \, Q_\Delta \, (U_\infty - \bar{U}_i) \qquad (2.72)$$

where $Q_\Delta$ is the outflow per unit width.
Since the distance to which this outflow will penetrate the freestream is likely to be small compared with the boundary layer thickness, a discrete velocity "jump" ($U_\infty - U_i$) will effectively be established at $y = \Delta$ . The outflow, which will take the form of a fairly concentrated jet, will also effect and control the entrainment of freestream fluid into the boundary layer.

The strength of this "outer" flow mechanism will depend on the magnitude of the residual vortex stress at $y = \Delta$ . Consequently, it will be relatively weak in cases of negative pressure gradient and relatively strong in cases of positive pressure gradient.

## 2.9 Application of the Ideal Flow Model to the Real Case

The flow model developed thus far assumes perfect regularity and constant strength of the vortex systems which control the non-viscous (i.e., turbulent) transfer of momentum and turbulent energy production. It is clear however that in an actual wall shear layer, the spacing, strength and wave velocity of individual systems will vary considerably for a number of reasons. In the first place, the instability responsible for the generation and maintenance of each vortex sheet will undoubtedly be sensitive to local turbulence levels in the layer and consequently will maintain an imprecise control of the rate of energy transfer to the vortex system. Secondly, as evident in Equation 2.44, the periodic time of each cycle is a function of the local wall shear stress, so that the frequency of passage of vortex systems over the wall must vary with Reynolds' number, a process which requires a net rate of decay of some existing systems or the generation of some additional ones. This process of selective decay or regeneration excludes the possibility of a smooth, continuous variation of individual spacing and wave velocity with Reynolds' number, so that local variation in these parameters from cycle to cycle are inevitable. Apart from this enforced mean rate of change of vortex system density distribution over the wall, it is almost certain that random decay and generation will also occur concurrently, due, for example, to a chance amalgamation of two existing systems, or to the chance occurrence of a new instability due to transient local conditions in the flow. Finally, interaction between adjacent bands of vortex systems, which has so far been neglected, may also give rise to local irregularities in the characteristic properties of the vortex systems (i.e. wave velocity, strength, spacing, etc.)

We can incorporate all the aforementioned effects into the flow model, without having to consider each in detail, by

assuming that the characteristic properties of the vortex systems exhibit some specified random variation about their respective mean values. In the new, more realistic and more complex physical picture which we thus obtain, we can retain intact the basic building-block of the theory (i.e. the horseshoe vortex system). The size, $\Delta$ (and hence the strength) the wave velocity, $U_i$, and the spacing, $l_x$, of individual systems are now described, however, by appropriate distributions of probability density about their mean values $\overline{\Delta}$, $\overline{U}_i$ and $\overline{l}_x$, used previously.

The first step is then to determine the practical limits of variation of each of these parameters. The variation in $\Delta$ is easily established, since the smallest system present (e.g. one newly generated by a fresh instability) will be comparable with the sublayer dimensions, i.e.

$$\overset{v}{\Delta} = (0)\,\frac{50\nu}{\overline{U}_\tau} \tag{2.73}$$

and hence

$$\frac{\overset{v}{\Delta}u_\tau}{\nu} = \text{constant} \tag{2.74}$$

while the largest systems present will actually define the edge of the boundary layer, i.e.

$$\overset{\Lambda}{\Delta} = (0)\,\delta \tag{2.75}$$

or

$$\frac{\overset{\Lambda}{\Delta}}{\delta} = \text{constant} \tag{2.76}$$

It is important to note that the ratio of the sizes of the largest and smallest systems present will not maintain a constant value with change in Reynolds' number. The reason for this is apparent if we note that according to present model, the x-rate of growth of the boundary layer, $d\delta/dx$ is actually due to the steady growth of the vortex systems, $d\Delta/dt$ as they move downstream with velocity $U_i$ so that

$$\frac{d\delta}{dx} = \frac{1}{U_{i_{\hat{\Delta}}}} \cdot \frac{d\hat{\Delta}}{dt} = \frac{v_{\gamma_{\hat{\Delta}}}}{U_{i_{\hat{\Delta}}}} \tag{2.77}$$

where $v_{\gamma_{\hat{\Delta}}}$ is the residual outflow velocity at the outer edge of the largest system. The corresponding rate of growth of the sub-layer is

$$\frac{d\delta_s}{dx} = \frac{d}{dx}\left(\frac{50\nu}{\overline{U}_\tau}\right) = -\frac{50\nu}{\overline{U}_\tau^2}\frac{d\overline{U}_\tau}{dx} \tag{2.78}$$

Since $v_{\gamma_\Delta}(\hat{\Delta})$ will be determined as an integral function of the vortex-interaction mechanism across the entire layer, while $d\overline{U}_\tau/dx$ is strictly a local property of the flow at the wall, it is evident that the ratio of $d\delta/dx \,/\, d\delta_s/dx$ and hence of $\hat{\Delta}/\Delta$ will vary in general with Reynolds' number. Specifically, from Equations 2.74 and 2.76,

$$\frac{\hat{\Delta}}{v_{\hat{\Delta}}} \propto \frac{\delta\overline{U}_\tau}{\nu} \tag{2.79}$$

The above conclusion has far-reaching implications in regard to

the spectral characteristics of all fluctuating quantities (i.e. wall pressure, turbulent velocities, etc.) within the layer, as will be seen shortly. The quantity $\delta \overline{U}_\tau/\nu$ which is of course known to vary with Reynolds' number, thus emerges as a key parameter in the present analysis.

The corresponding range of variation of the wave velocity, $U_i$, can also be determined without much difficulty. Simple considerations of the net change in primary momentum flux through the vortex system suggests that the intrinsic velocity distribution in the fixed axis system (x,y,z) as given by Equation 2.21 will be invariant with respect to the size and wave velocity of individual systems. It then follows that Equation 2.71 holds not only for the ideal "mean" vortex syste, but for all systems, that is, in general

$$\frac{U_i}{\overline{U}_\tau} = A + B \ln \frac{\Delta \overline{U}_\tau}{\nu} \qquad (2.80)$$

where A and B are the well known constants in the logarithmic law of the wall. Putting $\Delta = 50\ \nu/u_\tau$ we thus obtain an approximate estimate of $\overset{v}{U}_i$ as

$$\frac{\overset{v}{U}_i}{\overline{U}_\tau} = 14.9 \qquad (2.81)$$

or $\overset{v}{U}_i \approx 0.6\ U_\infty$ in a typical case

Putting $\Delta = \delta$, we obtain, from 2.

$$\frac{\overset{\Lambda}{U}_i}{\overline{U}_\tau} = A + B \ln \frac{\delta \overline{U}_\tau}{\nu} \qquad (2.82)$$

or making use of Coles law of the wake,

$$U_i = U_\infty - u_w \tag{2.83}$$

where $u_w$ is the wake component at the edge of the layer. For a typical constant pressure layer, then $\hat{U}_i \simeq 0.9\ U_\infty$. We thus find that the smaller vortex systems travel over the wall with a wave velocity less than the mean value, while the larger systems travel more rapidly than those of average size. This conclusion would seem to be relevant to the experimental observation that the low frequency components of the wall pressure field have higher convection velocities than the high frequency components. The probable variation in $l_x$ from cycle to cycle is more difficult to determine. However, some simple considerations reveal a possible feedback mechanism which may play a significant role in maintaining a fairly small variation in $l_x$ from cycle to cycle.

Let us consider, for example, a vortex system whose distance from the next one immediately downstream is less than the mean spacing, $\overline{l}_x$. Then the corresponding development time T for the intervening cycle will be less than $\overline{T}$ and hence the amount of excess energy flux accumulated by the primary motion during that cycle will be less than the average quantity. It thus follows that the upstream vortex system will be starved of energy and will consequently be a "weak" one. Its wave velocity will therefore be low, and it will consequently increase its distance from the system ahead (which we will assume is a "normal" system of mean strength and wave velocity). As the weak system falls progressively behind, however, $l_x$ and hence the energy available to it will increase so that it becomes progressively stronger. As it does so however, its wave velocity will also increase until it

eventually attains the mean value. Thus a weak, slow-moving system will fall behind and grow stronger while conversely, a strong-fast-moving system will tend to reduce its distance from the system ahead and at the same time grow weaker. This process will tend to re-establish order within the distribution of vortex systems and consequently will oppose the disorganizing influences discussed earlier. The actual probability distributions of strength, size, wave-velocity and spacing will thus depend on the relative magnitudes of these conflicting influences. It seems intuitively probable that while the size of individual systems will vary by a very large factor (i.e. $\delta u_\tau / 50\ \nu$) the variation in both wave velocity and spacing will probably be of the order of 10% to 50%.

The physical picture developed is thus one in which vortex-systems of widely and randomly-varying size and strength move over the wall with individual wave velocity and spacing which vary but little from their characteristic mean values. This picture, together with the model of the vortex-system discussed earlier, provides a new basis for the theoretical study of all mean and statistical flow properties in the turbulent wall shear layer. In this new approach, the need to consider turbulent processes arises only in cases where the microstructure itself is of specific interest. In all other cases, the "random" nature of the flow is expressed completely in the probability density distribution of vortex-system amplitude and (to a lesser extent) of the wave velocity and spacing of these systems.

The key to the macroscopic analyses of wall turbulence thus lies mainly in the knowledge of the probability distribution of vortex-system amplitude. In the particular case of boundary layer flows, a fairly direct experimental measurement of this distribution is afforded by the phenomenon through which it physically manifests itself, namely the intermittency phenomenon.

If the present model is correct, intermittency arises from the movement over the wall of the irregular interface which at any instant, marks and bounds the extremities of the randomly distributed vortex systems and their residual jet-like eruptions, as illustrated in Figure 17. The intermittency factor should thus be closely related to the probability density distribution of vortex system height in the boundary layer. The measured values of intermittency factor correspond closely to a Gaussian curve suggesting, as might be expected, that the probability distribution of vortex-system amplitude is also Gaussian.

The wake-type departure of the mean velocity distribution from the intrinsic logarithmic form in the outer part of the layer, is thus explained by the random distribution across the layer of the "velocity jumps" maintained by the individual vortex systems at $y = \Delta$. Corrsin, Ref. 13, has previously suggested that the assumption of a migrating velocity jump associated with a laminar "superlayer" at the outer edge of the flow, could provide a basis for analyzing the flow in the outer region, while Sarnecki, Ref. 14, has shown that an analysis of this type provides a good quantitative description of the mean velocity distribution in that region. The present theory provides a rational physical argument in support of these analyses and provides a firm basis for more detailed studies of the mean flow structure.

Finally, the theory provides a new deterministic approach to the study of fluctuating flow phenomena in wall turbulence. This approach can be illustrated briefly in relation to the wall pressure field under turbulent layers. As discussed earlier, each individual vortex system imposes a characteristic pressure signature on the wall which moves with the system downstream at the wave velocity, $U_i$. If the vortex systems were all identical in strength,

size, velocity and spacing as assumed in the preliminary "ideal" flow model, the resultant pressure signal recorded (say) by a pressure transducer fixed in the wall would have the perfectly regular, highly-skewed "spiky" form illustrated in Fig. 18a. The power spectral density distribution of this "ideal" signal, for example, would exhibit discrete lines at the "carrier" frequency and its appropriate harmonics.

In practice, however, the signal recorded will be of the form illustrated in Fig. 18b, where the amplitude and, to a lesser extent, the spacing of individual signature pulses, vary randomly from cycle to cycle.

This type of pulse train bears some resemblance to that encountered in P.A.M. (Pulse Amplitude Modulated) Multiplex communication systems as used extensively in telemetry systems, in which rectangular pulses of random amplitude are transmitted at a fixed carrier frequency. It is interesting to note that the frequency spectrum of such a pulse system has both discrete and continuous components, the latter increasing monotonically with decreasing frequency to a finite asymptotic value at zero frequency. While the individual pressure pulses generated by the vortex systems are not rectangular, the resultant frequency spectrum can nevertheless be expected to be similar to that of the rectangular pulse train, with the principle difference that the additional random variation in the "carrier" frequency and individual form of each wall pressure pulse will tend to "smear out" and thus largely eliminate the discrete line components of the spectrum. In this respect, it is interesting to note that measured spectra of fluctuating quantities (e.g. pressure and velocity) in wall turbulence sometimes appear to exhibit discrete frequency components, particularly at the high-frequency end of the spectrum (see, for example, the velocity spectra obtained by Bakewell, Ref. 15.)

If, as seems intuitively probable, the major contribution not only to the wall pressure, but to all fluctuating phenomena within the turbulent wall layers, comes directly from the vortex systems as they move over the wall, the key requisites for the detailed study of these phenomena are

1) a knowledge of the precise nature of a single "fluctuation" caused by the vortex system, combined with

2) knowledge of the probability distributions of strength, velocity and spacing of the vortex systems within the layer.

With this information, the statistical properties of all fluctuating quantities (including for example, pressure, velocity, temperature, particle concentration etc.) can be analyzed in detail.

# 3. SCALING LAWS FOR THE TURBULENT WALL PRESSURE FIELD

## 3.1 THE INCOMPRESSIBLE SCALING LAWS

The theoretical approach developed in Section 2 clearly provides a new basis for a detailed analytical study of the turbulent wall pressure field. Such a study would utilize a model of the proposed horseshoe vortex system similar to but more detailed than that described in Section 2, to obtain a quantitative relationship between the strength and shape of the vortex wall pressure signature and the distribution of vortex shear stress within the system. This relationship, combined with some assumed probability functions describing the distributions of vortex system amplitude spacing and wave velocity in the layer would permit calculation of, for example, the resultant wall pressure spectrum.

Such an analysis lies beyond the scope of the present study. However, the physical picture which the theory provides of the mechanics of wall turbulence also suggests new scaling laws through which experimental data can be analyzed and correlated. The development and application of these scaling laws constitutes a primary objective of the study and will now be considered.

It has already been shown that the strength of the pressure signature beneath the hypothesized horseshoe-vortex systems will generally be determined by the local wall shear stress, $\overline{\tau}_o$.

If we now consider a particular class of vortex systems of height, $\Delta$, having a mean spacing $l_x$, and wave velocity $U_i$, then the mean frequency of passage of those particular systems over the wall will be $\frac{U_i}{l_x}$. We, therefore, expect that the contribution of these vortex systems to the overall wall pressure spectrum should scale on $\overline{\tau}_o$ and $\frac{U_i}{l_x}$,

$$\text{i.e.} \qquad \left[\frac{d\overline{p}^2 / \overline{\tau}_o^2}{d\left(\frac{\omega l}{U_i}\right)}\right]_\Delta = f\left(\frac{\omega l_x}{U_i}\right) \qquad (3.1)$$

According to the present theory, the actual flow in the boundary layer comprises a wide range of such systems varying in size approximately from the sublayer thickness to the boundary layer thickness. Consequently, we may consider the wall pressure spectrum as comprising a wide range of components of the form given in equation 3.1 for (o) $\delta_s \leq \Delta \leq$ (o) $\delta$.

While a detailed study would require analysis of all the components within this spectrum, we need only consider, for present purposes, the contribution of two general classes of vortex systems; namely, those of size $\Delta$ comparable with the sublayer thickness $\delta_s$, and those of size comparable with the boundary layer thickness, $\delta$. The scaling laws obtained from a dimensional analysis of these two classes should apply respectively to the high and low frequency portions of the wall pressure spectrum.

If we consider first the smaller systems,

it is evident that the average spacing of these systems will be comparable with the basic length of the development/breakdown cycle,

i.e. $$\ell \approx U_i T \qquad (3.2.)$$

or according to equation 2.44,

$$\ell \propto \frac{U_i \nu}{\bar{U}_\tau^2} \qquad (3.3)$$

Hence, for the small vortex systems ($\Delta \approx \delta_s$)

$$\frac{d\bar{P}^2/\bar{\tau}_o^2}{d\left(\frac{\omega\nu}{\bar{U}_\tau^2}\right)} = f\left(\frac{\omega\nu}{\bar{U}_\tau^2}\right) \qquad (3.4)$$

For the large vortex system ($\Delta=\delta$) the average spacing between the systems will be proportionately longer, so that

$$\ell \approx \delta \qquad (3.5)$$

and

$$\frac{d\bar{P}^2/\bar{\tau}_o^2}{d\left(\frac{\omega\delta}{U_i}\right)} = f\left(\frac{\omega\delta}{U_i}\right) \qquad (3.6)$$

From equation 2.80, we may rewrite equation 3.6 as

$$\frac{d\bar{P}^2/\bar{\tau}_o^2}{d\left(\frac{\omega\delta}{\bar{U}_\tau}\right)} = f\left(\frac{\omega\delta}{\bar{U}_\tau}\right) \qquad (3.7)$$

The scaling laws 3.4 and 3.7 should be respectively applicable to the high-and low-frequency portions of the wall pressure spectrum. However, it will be more convenient to apply them, not the power spectra themselves, but to the distributions

of the first moment of the power spectral density, which according to equations 3.4 and 3.7 should exhibit the functional forms.

$$\frac{\omega}{\bar{\tau}_o^2}\,\frac{d\bar{P}^2}{d\omega} = f\left(\frac{\omega\nu}{\bar{U}_\tau^2}\right) \qquad (3.8)$$

at the higher frequencies and

$$\frac{\omega}{\bar{\tau}_o^2}\,\frac{d\bar{P}^2}{d\omega} = f\left(\frac{\omega\delta}{\bar{U}_\tau}\right) \qquad (3.9)$$

at the lower frequencies. These forms will be referred to hereafter as the high-frequency and low-frequency data plots respectively.

It should be noted that the dimensionless frequencies in equations 3.8 and 3.9 are related by the parameter $\frac{\delta \bar{U}_\tau}{\nu}$, and that, consequently, the overall R.M.S. intensity of the pressure field must have the functional form

$$\frac{\sqrt{\bar{P}^2}}{\bar{\tau}_o} = f\left(\frac{\delta \bar{U}_\tau}{\nu}\right) \qquad (3.10)$$

The effect of pressure gradient, will be expressed, according to equation 2.60, through the pressure gradient parameter

$$P\left(= \frac{\nu}{\rho \bar{U}_\tau^3}\,\frac{dp}{dx}\right)$$

so that in the presence of pressure gradient, equations 3.8 and 3.9 will become, respectively

$$\frac{\omega}{\bar{\tau}_o^2}\,\frac{d\bar{P}^2}{d\omega} = f\left(\frac{\omega\nu}{\bar{U}_\tau^2}, P\right) \qquad (3.11)$$

and

$$\frac{\omega}{\bar{\tau}_o^2}\,\frac{d\bar{P}^2}{d\omega} = f\left(\frac{\omega\delta}{\bar{U}_\gamma}, P\right) \qquad (3.12)$$

Physically, the effect of adverse or favorable pressure gradient will be to increase or decrease respectively the energy levels of the spectra, as explained in section 2.7. Calculation of the magnitude of the pressure gradient contribution to the wall pressure spectrum must, however, await a quantitative analysis of the vortex shear stress mechanism on the basis laid down in that section.

## 3.2 THE EFFECT OF COMPRESSIBILITY ON THE SCALING LAWS

The theoretical model of wall turbulence on which the present study is based has been developed initially for the case of incompressible flow. Compressibility will clearly modify the model in a number of fundamental ways. In the first place, the presence of a significant temperature gradient in the sublayer region will undoubtedly effect the instability mechanism responsible for the generation of the horseshoe-vortex systems. Thus, the characteristic periodic time, T, of the development/breakdown cycle and the associated values of vortex system spacing and wave velocity may be altered. Secondly, the associated variation in viscosity may significantly alter the distribution of primary velocity through the layer, and hence the rate and distribution of energy transfer between the primary motion and vortex systems. Thirdly, the variation in fluid density will also modify the energy transfer

mechanism and hence the distribution of vortex strength of the horseshoe elements across the layer. These last two effects will combine to modify both the strength and composition of the vortex wall pressure signature and hence the composition and intensity of the wall pressure spectrum.

The above mentioned compressibility effects would necessarily be considered in detail in any rigorous analysis of the flow structure of supersonic turbulent layers. For the present purpose of developing valid scaling laws for the wall pressure field, however, it seems reasonable to assume that these effects can be adequately accounted for, at least up to supersonic Mach numbers of (say) 3 or 4, by utilizing average representative values of the local fluid properties within the flow regime of interest. Thus, in particular, we may assume the validity of equation 2.44 for the mean periodic time, $\overline{T}$ of the development/breakdown cycle, if we use the local value of viscosity at the wall, $\nu_o$, and define the friction velocity $\overline{U}_\tau$ in terms of the value of fluid density at the wall $\rho_o$ thus

$$\overline{U}_\tau \equiv \sqrt{\frac{\overline{\tau}_o}{\rho_o}} \qquad (3.13)$$

In the scaling law for the high-frequency portion of the supersonic wall pressure spectrum, we likewise define the strength and size of the small vortex systems in terms of the local, wall

values of the fluid properties, ie.

$$\overset{v}{\Delta} \propto \frac{\nu_o}{\bar{U}_\tau} \qquad (3.14)$$

where $\bar{U}_\tau$ is defined as in equation 3.13.

In the low-frequency law, the effects of compressibility on the strength and size of the larger vortex-systems is implicity expressed through the boundary layer thickness, $\delta$, which is known to vary with Mach numbers for given Reynolds' number. Thus the proposed fundamental scaling laws for the supersonic spectrum are:

$$\frac{\omega}{\bar{\tau}_o^2}\frac{d\bar{p}^2}{d\omega} = f\left(\frac{\omega\nu_o}{\bar{U}_\tau^2}\right) \qquad (3.15)$$

for the high frequency components, and

$$\frac{\omega}{\bar{\tau}_o^2}\frac{d\bar{p}^2}{d\omega} = f\left(\frac{\omega\delta}{\bar{U}_\tau}\right) \qquad (3.16)$$

for the low frequency components.

As in the incompressible case, the spectrum shape, and overall R.M.S. intensity of the wall pressure fluctuations will vary with Reynolds numbers as a function of the ratio of overall boundary layer thickness to sublayer thickness, i.e. as a function of

$$\frac{\delta\bar{U}_\tau}{\nu_o}$$

The analysis of selected subsonic and supersonic data on the basis of the scaling laws 3.8 and 3.9, and 3.15 and 3.16 is discussed in the following section.

## 4.0 Analysis of Experimental Data

### 4.1 Selection of Experimental Data

Prior to the data analysis described herein, a literature search was conducted to collect all the available experimental information relating to the wall pressure field under turbulent layers. In addition, letters of inquiring were transmitted to selected private firms, universities and research organizations to obtain futher unpublished data which might be available. The data collected included measurements in both subsonic and supersonic flows. More reliabilty can generally be placed on subsonic data than on those obtained in supersonic flows in which, for example, unwanted shock configurations and high background noise levels make accurate and consistent pressure measurements considerably more difficult. Verification of the proposed scaling laws in the case of subsonic data is thus an essential step in the more general analysis of supersonic data.

Not all the data collected was analysed. The scaling laws developed in section 2. require, for their application, accurate knowledge of local flow parameters such as boundary layer thickness and wall shear stress, as well as local fluid properties, (i.e. density and viscosity at the wall). The supersonic data, in particular can generally be graded in quality according to its source. Measurements obtained in

wind-tunnels and other experimental facilities such as pipes and ducts, generally provide the most accurate and detailed information. Data obtained from aircraft in flight provide less information concerning the local state of the flow, and are generally obtained in less well-behaved and well-defined regimes than those established in experimental facilities. Finally data obtained on missiles and space vehicles generally comprise no more than the fluctuating wall pressured itself. Considerably uncertainty exists regarding the relevant shock, acoustic and local flow enviromentas.

Much more weight must consequently be placed for example, on the wind-tunnel data of Speaker and Ailman[16] than that measured on (say) the Titan III[17] booster vehicle.

The subsonic and supersonic data finally selected for analysis is shown in Tables I, II, III which includes the reference source as well as the relevant local boundary layer parameters obtained as described in section 4.2 below.

## 4.2 Boundary layer Parameters

Application of the scaling laws derived in section 3, requires a knowledge of local boundary layer parameters, and of local flow properties. In many cases, the listing of these quantities was incomplete and in some cases totally absent. In such cases, the required boundary layer parameter were calculated from a knowledge of the Reynolds' number.

$$R_N = \frac{U_\infty x}{\nu_\infty}$$

Where $U_\infty$ = freestream velocity

$x$ = distance of transducer downstream from orgin or virtual orgin of boundary layer,

$\nu_\infty$ = freestream kinematic viscosity

Determination of reliable values of x. were generally difficult in the case of flight data, where, for example, the interstage geometry on space vehicles and its effect on boundary layer development along the vehicle, made the location of the virtual orgin of the layer extremely uncertain.

The values of boundary layer thickness, $\delta$, displacement thickness, $\delta^*$, and local skin friction, $C_f$, were subsequently determined from the estimated curves presented by Bies[18] in figures 1, 2 and 4 of that report.

In cases where those parameters had been calculated, rather than measured, by the investigator concerned, the values presented were checked against those predicted by Bies'curves, and in the odd case where a significant discrepancy was found, Bies' predicted values were used for the sake of overall consistency in the analysis.

It was generally found that little or no uncertainly arose in regard to the correct choice of skin friction value.

However, much less confidence can be placed on the calculated values of boundary layer thickness, in cases of supersonic flow. This parameter, which unfortunately, has major significance in the present analysis, is perhaps the most difficult of all local flow quantities to calculate in supersonic layers.

Where necessary, freestream flow properties for flight test data were obtained as a function of known attitude from reference [19].

For the supersonic data, the required values of kinematic viscosity at the wall were subsequently determined from Sutherland's formula

$$\left(\frac{\mu_o}{\mu_\infty}\right) = \left(\frac{\bar{T}_o}{\bar{T}_\infty}\right)^{0.76} \qquad (4.1)$$

with the assumption of adiabatic flow conditions.

## 4.3 Transducer Size Correction

Treatment of the problem of transducer resolution at high frequencies, varied considerably in various experimental studies selected for analysis. Some investigators applied no corrections to their measured pressure data, while others ulitized the various correction techniques developed by Corcos [20], Willmarth and Roos [21] and Gilchrist and Strawderman [22]. For consistency, in the present analysis, Corcos' correction was applied to data and subtituted for other corrections originally applied.

Application of Corcos's correction requires a knowledge of the mean convection velocity of the wall pressure field. While the correction evolved is not very sensitive to the precise choice of convection velocity, the values used in the present case were taken as the mean wave-velocity of the hypothesized vortex systems over the wall, that is the wave-velocity of a vortex-system of mean height equal to half the boundary layer thickness (i.e. $\Delta = \frac{\delta}{2}$). It is easily shown that, for constant pressure layers, this velocity is obtained via equation 2.80, as

$$\frac{\bar{U}_c}{\bar{U}_\tau} = \frac{\bar{U}_i}{\bar{U}_\tau} = \frac{U_\infty}{\bar{U}_\tau} - \frac{U_w}{\bar{U}_\tau} + B \ln \frac{1}{2}$$

where $U_w$ is the value of Coles Wake Component at $y = \delta$; hence

$$\begin{aligned} \frac{\bar{U}_c}{\bar{U}_\tau} &= \frac{U_\infty}{\bar{U}_\tau} - 2.75 - 1.73 \\ &= \frac{U_\infty}{\bar{U}_\tau} - 4.48 \end{aligned} \qquad (4.2)$$

## 4.4. ANALYSIS OF SUBSONIC DATA

The selected subsonic data obtained in constant pressure layers are presented in Figures 19 and 20 in which they are plotted respectively in the non-dimensional form expressed in equations 3.8 and 3.9 of section 3.1. In the 'low frequency' plot, Figure 19, the curves generally exhibit a strong tendency to collapse at low frequency as predicted, the notable exceptions being the data of Schloemer[23] and also the M=0.9 data of Speaker and Ailman,[16] which, as noted by the investigators, may have been obtained in the proximity of a normal shock. As expected, the curves exhibit considerable scatter at high frequencies in the plot. In the high frequency plot of Figure 20, the curves now oonverge markedly at high frequencies, the exceptions in this case being the high subsonic Mach number data of Speaker and Ailman.

It may be noted that in the high frequency plot of Figure 20, the curves generally exhibit maxima in the region of the dimensionless mean 'carrier' frequency of the vortex system given by equation 2.44,ie.

$$\frac{\omega\nu}{\bar{U}_\tau^2} = \frac{2\pi\nu}{T\,\bar{U}_\tau^2} = 0.056 \qquad (4.3)$$

As predicted by the present theory.

In Figures 21 and 22, low and high frequency plots of the subsonic pressure gradient data obtained by Schloemer[23] and Bradshaw.[24] are presented. It is clear that, as discussed

in section 3.1, the scaling laws as they stand do not fully account for the effect of pressure gradient on the overall level of the spectra, that is, the adverse and favorable gradient data still exhibit higher and lower levels respectively than the corresponding constant pressure curves. While an analysis of the quantitative effect of pressure gradient lies outside the scope of the present program, the curves are included since they provide qualitative confirmation of the predicted effect of pressure gradient and are relevant to the study of the intense fluctuating pressure field in the vicinity of impinging shocks and surface steps.

The shift in frequency of the maxima in the various spectra in the high frequency plot (Fig. 22) can be plausibly explained as follows. In the case of adverse pressure gradient, according to section 2.7, all vortex systems will increase in strength, thus modifying the probability density distribution of vortex system size in favor of the larger system. This, in turn, must result in a shift of energy content in the pressure spectrum towards the lower frequencies relative to the mean "carrier" frequency of the vortex systems $\left( \bar{\omega} = 0.056 \frac{\bar{U}_\tau^2}{\nu} \right)$. Thus, the high frequency plot, in which frequency is essentially made non-dimensionless with respect to the carrier frequency, $\bar{\omega}$, will exhibit a shift to lower frequencies in the maximum power spectral density in the case of adverse pressure gradient and, conversely, a shift to higher frequencies in the case of favorable pressure gradient,

as evident in Figure 22.

This shift in power spectral density maxima will not, however, be so pronounced in the low frequency plot, Figure 21, since the change in frequency at which the maxima occur will be largely countered by the corresponding change in $\frac{\delta \bar{U}_r}{\nu}$ which provides the scaling factor between the dimensionless frequencies in the respective plots.

In summary it may be stated that the constant pressure gradient spectra obtained at subsonic speeds clearly exhibit the predicted dimensionless behavior at low and high frequencies and the anticipated maxima at the mean "carrier" frequency of the vortex systems. The pressure gradient data exhibits the expected trend towards high and lower levels respectively with adverse and favorable gradients, and an associated shift in maxima below and above the mean carrier frequency.

## 4.5 ANALYSIS OF SUPERSONIC DATA

The supersonic data accepted for analysis is listed in Table III, together with the source references and pertinent boundary layer parameters.

In Figures 23 and 24, the spectra measured by Speaker and Ailman at one particular location (x=o) are presented in low and high frequency plots respectively for the complete Mach number range $0.42 \leq M \leq 3.45$.

Included in each figure are shaded regions indicating the concentration of data points in the corresponding subsonic cases. It is seen in Figure 23, that at the low frequencies, the supersonic data collapse well within the subsonic data band. For the high frequency plot Figure 24, the supersonic spectra fall below the corresponding subsonic curves. Speaker and Ailman note, however, that the condenser microphone, which was employed at this station, is suspect at the higher frequencies. Furthermore, a lowering of the resonant peak frequencies of the microphones with increasing Mach numbers also made the application of corrections for resonance increasingly difficult to apply at higher frequencies. It is therefore difficult to assess the validity of the high frequency scaling laws on the basis of this evidence.

In Figures 25 and 26, a much wider range of Speaker and

Ailman data is presented, covering not only the full Mach number range, but also a number of different transducer locations.

While there is some considerable data scatter in each plot, there is clearly evident a strong concentration of supersonic data points at low frequency within the subsonic band of Figure 19 in the low frequency plot, Figure 25. In the high frequency plot Figure 26, there is a corresponding, but less evident, tendency for the spectral curves to close. On the evidence available, it is impossible to determine whether

1) the high-frequency scaling law fails or is inadequate at supersonic Mach number or, alternatively
2) the experimental measurements are inaccurate at higher frequencies.

The conspicuous departure of a number of curves from the subsonic data band in Figure 25, can plausibly be explained by the presence of weak shock systems in the experimental facility, as suggested by Speaker and Ailman in their report. In the first case, all the spectra concerned relate to supersonic or transonic flow conditions. Furthermore, the spectra involved generally exhibit increased power at the lower frequencies consistent with the effects of adverse pressure gradient as demonstrated by the subsonic pressure gradient data of Schloemer and Bradshaw, Figures 21 and 22. The behavior of the spectra concerned could,

therefore, be attributed to local adverse pressure gradients imposed on the flow by impinging shocks. This explanation is strengthened by the impinging shock data recorded by Speaker and Ailman, which is clearly characterized by a concentration of energy at the lower frequencies.

While the measurements of Speaker and Ailman undoubtedly provide some of the most detailed and useful data available, they unfortunately do not cover, despite the large range of Mach numbers involved, a significant range of the parameter $\frac{\delta \bar{U}_\tau}{\nu_o}$ which provides the scaling factor between the low and high frequency laws (see Table III). Consequently, they do not provide a good test of the validity of the two-component spectrum model at supersonic Mach numbers.

The effect of the parameter $\frac{\delta \bar{U}_\tau}{\nu_o}$ on the spectra plotted according to the proposed scaling laws can be assessed by comparing Speaker and Ailman supersonic data with that obtained at significantly different values of this parameter. Belcher[25] for example has recorded wall pressure spectra in flight experiment at Mach numbers between 1.3 and 1.9 and at values of $\frac{\delta \bar{U}_\tau}{\nu_o}$ of approximately 24,000. These are presented in the low and high frequency plots in Figures 27 and 28 respectively. In the low frequency plot, Figure 27, the data at low frequencies lies close to the subsonic data band, but with slightly increased power spectral densities. It is unlikely that this discrepancy could be due to a pure Mach

number effect, since Speaker and Ailman's data covering a much wider Mach number range falls well within the subsonic data band. While it could possibly result from errors in the calculated values of Belcher's boundary layer parameters, it is more likely due to an additional Reynold's number effect dependent on $\frac{\delta \bar{U}_\tau}{\nu_o}$ as discussed later in this section.

Belcher's data unfortunately does not extend to sufficiently high frequencies to permit comparison with the high frequency scaling law, Figure 28. However, the various spectra do appear to converge satisfactorily towards the subsonic high-frequency data band.

Figures 29 and 30 present low and high frequency plots of the M=1.0 Titan III data[17][26] as examples of space vehicle data obtained at high values of $\frac{\delta \bar{U}_\tau}{\nu_o}$ $(50 - 100 \times 10^3)$. Unfortunately the degree of scatter in the data and the relatively small frequency range involved makes evaluation difficulty. While the power spectral densities at low frequency appear to be very much higher than the data of Speaker and Ailman, and of Belcher, the scope of the spectra is very much less than that the subsonic low-frequency data band in Figure 29. The Titan spectra, thus, bear a marked resemblance to certain spectra of Speaker and Ailman in Figure 25, which, as discussed, earlier, display evidence of local shock impingement. This will be discussed further in section 4.6.

As can be seen in Figure 30, the small frequency range of the data points does not permit evaluation of the high frequency scaling of the spectra.

In Figures 31 and 32, low and high frequency plots are presented of the data obtained by Hubbard[27] on the Scout Vehicle over a Mach range of 0.67 to 4.08 and by Leech[28] on a F102 aircraft at M=1.16. Included in these figures are the Titan data and the data obtained by Belcher to provide a basis for comparison.

In the low frequency plot, Leech's data falls somewhat below the subsonic data band, while Hubbard's data exhibits a discernible trend to higher power spectral densities with increasing Mach number. Again the slope of the various spectra are generally lower than those of the subsonic data and of the spectra of Belcher, and Speaker and Ailman.

In the high frequency plot, Figure 32, the frequency range again does not extend high enough to permit evaluation of the high frequency scaling law, although it can be said that in general, the data are not incompatible with the subsonic high-frequency band.

Finally, in Figures 33 and 34, the wind-tunnel data obtained by Murphy[29] at M= 3.46, which includes a case of negative pressure gradient, is presented. In Figure 33, the zero-pressure gradient data falls satisfactorily close to the subsonic data band, while,

as expected, the negative pressure gradient data exhibits significantly lower levels. The frequency range does not extend high enough to permit evaluation of the high-frequency scaling law in Figure 34, although the data again is not inconsistent with the subsonic data band.

## 4.6 DISCUSSION OF DATA ANALYSIS

The data discussed in the previous sections may now be interpreted in relation to the subsonic model spectrum established by the scaling laws 3.8 and 3.9, and the behaviour of the subsonic data at low and high frequencies as shown in Figures 19 and 20. This model is illustrated in Figure 35. In the high frequency plot, the spectra (strictly the first moment, Figure 35a, of the spectra as plotted) coincide at high frequencies but diverge with decreasing frequency as shown. In particular, the spectral maxima increase with increasing $\frac{\delta \bar{U}_T}{\nu_o}$. In the low frequency plot, the spectra coincide at low frequencies and diverge with increasing frequency, the maxima again increasing with $\frac{\delta \bar{U}_T}{\nu_o}$.

The departure of some of Speaker and Ailman's spectra at low frequency, as illustrated schematically in Figure 35b, has already been attributed to possible local shock impingement. It may now be seen that the spectra obtained on the Scout and Titan vehicles, display very similar trends, as illustrated in Figure 35c, with the only difference that the curves are translated to higher

powers and frequencies, consistent with the significantly higher values of $\frac{\delta \bar{U}_T}{\nu_o}$ which were obtained in those tests.

Since the presence of impinging shock systems on the Scout and Titan test vehicles in the vicinity of the recording transducers is not unlikely, the foregoing explanation of the apparent discrepancy between the data at low frequencies is entirely plausible (An alternative but similar explanation could also be provided by the presence of extraneous acoustic radiation at the lower Mach numbers. Structural vibration of the transducers should also be considered as a possible explanation of the reduced slope of the spectra at low frequencies for both subsonic and supersonic Mach numbers.)

Failure of the low-frequency scaling laws because of some unaccounted Mach number effect provides a much less plausible explanation of the observed discrepancies, in view of the good overall collapse of much of Speaker and Ailman's data into the subsonic low-frequency data band over the entire Mach number range

$$0.4 < M < 3.5$$

With regard to the high frequency scaling law, which appears fairly well-established in the case of the subsonic data, very little of the supersonic data available extends sufficiently far into the relevant high-frequency range to test its validity for compressible flows. All that can safely be stated is that none of the data

examined appeared to be strongly incompatible with the subsonic high-frequency data band.

More experimental data is required in order to establish firmly the validity of the proposed scaling laws in supersonic flows. The present analysis has, however, established clearly the importance of a well-behaved and well-defined flow environments if such tests are to provide meaningful information. In particular, more care is generally required in measuring or otherwise defining the relevant boundary layer parameters, particularly skin friction and overall boundary layer thickness, and the variation of local fluid properties through the layer. Because of the sensitivity of the hypothesized votex structures to local pressure gradient, it would appear essential to ensure the absence of impinging shock systems in the vicinity of the recording transducers. The influence of shock impingement on the wall turbulence mechanism, and hence, on the wall pressure field, is considered one of the most significant implications of the present study.

## 5.0 Conclusions.

It is believed that the broad objectives of the current research program have been achieved in the following respects:

1. A new theoretical model of the structure of wall turbulence has been further developed and extended to provide a clearly defined physical picture, and an explanation of the characteristic pressure field on the wall. Of primary significance in the model is the direct causal relationship established between the basic component of this pressure field (a highly skewed spiky pulse form) and the turbulent shear stress mechanism. This relationship provides a firm basis for a quantitative analysis of the wall pressure field, including determination of the effects of pressure gradients, compressibility, shock boundary layer interaction, flow separation and surface roughness.

The essentially simple nature of the proposed model of the pressure field which comprises an A.M. (amplitude modulated) pulse system with randomly varying amplitude also suggests an analog or even digital approach to the analysis of the field and the associated practical problems of structural vibration and aerodynamic noise.

On a more fundamental level the theoretical model developed suggests new experimental studies of turbulent shear layers to further the understanding of the mechanism of, for example, of shock turbulence interaction, unsteady phenomenon associated with flow separation and reattachment and heat and mass transfer in turbulent layers.

2. Basic scaling laws relating to the turbulent wall pressure spectrum under incompressible and compressible attached shockless flows have been developed. The derivation of these laws is based on the assumption that the wide range of horseshoe vortex systems (which, according to the underlying theory, are present in the actual boundary layer and are responsible for generating the wall pressure field ) can, for scaling purposes, be represented by a two component model in which the small systems are comparable in size to the sublayer thickness and the large systems comparable to the size of the boundary layer thickness. Since these two components will contribute respectively to the higher and lower frequency components of the wall pressure field, the simple model leads to two sets of scaling laws pertaining respectively to the high and low frequency portions of the spectrum. Compressibility effects are incorporated in the scaling laws by suitably accounting for the variation of local fluid properties

across the layer.

While the present study clearly indicates the manner in which the pressure field is affected by the pressure gradient and the nature of the relevant pressure gradient parameter, a quantitative assessment of the pressure gradient effect must await a more detailed analysis of the proposed flow model.

3. Experimental data relating to both the subsonic and supersonic pressure fields under attached flows have been collected, evaluated and used to assess the validity of the proposed scaling laws. These laws appear to be well supported by subsonic data particularly at low frequencies. Of the supersonic data those measured in wind tunnels and those measured on aircraft at low and moderate Reynolds numbers, collapse satisfactorly at low frequencies on the proposed scaling basis. The data of Speaker and Ailman in particular shows consistent agreement at low frequencies with the low frequency scaling law over the entire Mach number range with the exception of some spectra which are suspect because of local impinging shocks. Data obtained on Titan[17][26] and Scout[27] space vehicles at high Reynold's numbers, however are not in good agreement with the proposed scaling basis at low frequencies. It is believed that these

discrepancies are more likely indicative of shock impingement or structural vibrational effects rather than of the failure of the scaling laws at high Reynolds numbers. It is not believed that compressibility effect are responsible,in view of the general compatibility of Speaker and Ailman's data up to maximum Mach number of 3.50 tested. Unfortunately the space vehicle data is also of doubtful value in assessing the validity of the scaling laws in view of the uncertainty regarding the boundary layer parameters(particularly boundary layer thickness and the skin friction) which were obtained during the tests. The validity of the high frequency law could not be generally evaluated from the supersonic data partly because the measured frequency range in most cases did not extend sufficiently high and partly because of uncertainty regarding transducer resolution corrections at the high frequency end of the measured spectra. In almost all cases however, the measured spectra did not appear incompatible with the proposed high frequency scaling law.

4. The scope of the present program did not permit a detailed analitical study of the very high pressure levels associated with the impinging shocks and more generally with regions of separating flows as found in the vicinity of

of surface steps; however the analytical framework established by the program provides, it is believed, a firm basis for further work in these specific problem areas.

# APPENDIX

## APPENDIX

### Symbols

| | |
|---|---|
| A, B | Constants in Logarithmic Law of Wall. |
| a, b | Constants defined in eq. 2.31. |
| c | Constant defined in eq. 2.36. |
| $D_i$ | Induced drag. |
| D | Microphone diameter in inches. |
| E | Energy flux. |
| $F_n$ | Normal component of reactive stress on fluid due to vortex interaction. |
| $F_s$ | Tangential component of reactive stress on fluid due to vortex reaction. |
| f | Denotes functional dependence. |
| H | $= y/2\sqrt{(\nu T)}$. |
| h | $= y/2\sqrt{(\nu t)}$. |
| k | Constant defined in eq. 2.16. |
| L | Lift force. |
| $l_x$ | Streamwise spacing of vortex systems |
| $l_z$ | Width of vortex system. |
| M | Momentum flux, Mach Number. |
| n | Frequency of vortex generation. |
| P | Pressure gradient parameter ( $= \frac{\nu}{\rho \bar{U}_\tau^3} \frac{d\bar{p}}{dx}$ ). |
| p | Static pressure. |
| Q | Volume flow. |
| $Q_\Delta$ | Residual outflow at outer edge of vortex system. |
| q | Instantaneous flow quantity (may be identified as velocity or pressure). |

| | |
|---|---|
| $q'$ | Secondary or turbulent (random) component of q. |
| $q^*$ | Primary (non-random) component of q. |
| $\overline{q}$ | Mean value of q. |
| R | Resultant force. |
| T | Periodic time of breakdown development cycle (also used to denote vorticity flux in fig. 4). (also temperature as used in Section 4.) |
| t | Time. |
| $U_{eff}$ | Effective velocity. |
| $U_i$ | Wave velocity of instability/vortex system. |
| $U_{rel}$ | Relative velocity. |
| $\overline{U}_\tau$ | Mean wall friction velocity ($= \sqrt{\frac{\overline{\tau}_o}{\rho}}$ ). |
| $U_\infty$ | Freestream velocity. |
| u,v,w | Instantaneous velocity components in x,y,z directions. |
| u',v'w' | Secondary (random) components of u,v,w. |
| u*,v* | Primary (non-random) components of u,v. |
| $\Delta u^*_p$ | Pressure gradient contribution to u*. |
| $\overline{u}$ | Mean x-velocity in boundary layer. |
| $u_\gamma$ | 'Intrinsic' streamwise induced velocity of vortex system. |
| $v_\gamma$ | Normal induced velocity of vortex system. |
| x,y,z | Fixed axis system (fixed relative to wall). |
| $x-\overline{U}_i t,y,z$ | Moving axis system (fixed relative to vortex systems). |
| $\Gamma$ | Vorticity. |
| $\gamma$ | Vorticity density per unit length. |

| | |
|---|---|
| $\Delta$ | Height of vortex system. |
| $\delta$ | Boundary layer thickness. |
| $\delta_s$ | Sublayer thickness. |
| $\lambda$ | Ratio of turbulent to vortex shear stress. |
| $\mu$ | Dynamic viscosity. |
| $\nu$ | Kinematic viscosity. |
| $\rho$ | Density. |
| $\tau_T$ | Mean turbulent shear stress. |
| $\tau_{vor}$ | Vortex shear stress. |
| $\overline{\tau}_o$ | Mean wall shear stress. |
| ' | Denotes secondary random turbulent motion. |
| * | Denotes primary, non-random motion. |
| - | Denotes mean value. |
| " " | Denotes reference to moving-axis system. |
| o | Denotes reference to wall conditions. |

## REFERENCES


1. Black, T.J. — "Some Practical Applications of a New Theory of Wall Turbulence" Proceedings of the 1966 Heat Transfer and Fluid Mechanics Institute, Stanford University Press, 1966.

2. Einstein, H.A. Li, H. — "The Viscous Sublayer Along a Smooth Boundary" Proceedings of the A.S.C.E. Journal of Engineering, Mechanics Division, 82, No. E.M. 2, 1956.

3. Townsend, A.A. — "Equilibrium Layers and Wall Turbulence" Journal of Fluid Mechanics, Vol. 11, p. 97, 1961.

4. Grant, H.L. — "The Large Eddies of Turbulent Motion" Journal of Fluid Mechanics, Vol. 4, p. 149, 1958.

5. Malkus, W.V.R. — "Outline of a Theory of Turbulent Shear Flow" Journal of Fluid Mechanics, Vol. 1, p. 521, 1956.

6. Landahl, M.T. — "A Wave-Guide Model for Turbulent Shear Flow" NASA CR-317, Oct. 1965.

7. Benney, D.J. Greenspan, H.P. — "Remarks on Transition and the Stability of Time-Dependent Shear Layers" The Physics of Fluids, Vol. 5, No. 7, July 1962.

8. Kline, S.J. Runstadler, P.W. Reynolds, W.C. — "An Experimental Investigation of the Flow Structure of the Turbulent Boundary Layer" Report MD-8, Thermosciences Division, Department of Mechanical Engineering, Stanford University, 1963.

9. Kline, S.J. Schraub, F.A. — "A Study of the Structure of the Turbulent Boundary Layer With and Without Longitudinal Pressure Gradients" Report MD-12, Thermosciences Division, Department of Mechanical Engineering, Stanford University, 1965.

10. Willmarth, W.W. Tu, B.J. — "An Experimental Study of the Structure of Turbulence Near the Wall Through Correlation Measurements in a Thick Turbulent Boundary Layer"

## REFERENCES


University of Michigan, Department of Aerospace Engineering Aerodynamics Laboratory, ORA Project 02920-3-T, March 1966.

11. Coles, D. — "The Law of the Wake in the Turbulent Boundary Layer" Journal of Fluid Mechanics, Vol. 1, p. 191, 1956.

12. Theodorsen, T. — "Mechanism of Turbulence" Proc. 2nd Midwestern Conf. Fluid Mechanics, The Ohio State University, 1952.

13. Corrsin, S. Kistler, A.L. — "Free-Stream Boundaries of Turbulent Flows." NACA Report 1244, 1955.

14. Sarnecki, A.J. — Ph.D. Thesis, Cambridge University, 1960.

15. Bakewell, H.P. — "An Experimental Investigation of the Viscous Sublayer in Turbulent Pipe Flow" Department of Aerospace Engineering, Pennsylvania State University, 1966.

16. Speaker, W.V. Ailman, C.M. — "Spectra and Space-Time Correlations of the Fluctuating Pressures at a Wall Beneath a Supersonic Turbulent Boundary Layer Perturbed by Steps and Shock Waves," NASA Contractor Report 486, May 1966.

17. Bolt, Beranek, and Newman, Inc. — "Acoustic and Vibration Data From Titan III SSLV-1 Flight," Report No. 1252, May 1965.

18. Bies, A. — "A Review of Flight and Wind Tunnel Measurements of Boundary Layer Pressure Fluctuations and Induced Structural Response," BBN Report No. 1269, January 1966.

19. — "Manual of the ICAO Standard Atmosphere-Calculations by the NACA", NACA TN 3182, May 1954.

20. Corcos, G.M. — "Pressure Fluctuations in Shear Flows," University of California, Institute of Engineering Research, Series 183, Issue No. 2, Berkeley, Calif, July 1962.

## REFERENCES


21. Willmarth, W.W. Roos, F. W. "Resolution and Structure of the Wall Pressure Field Beneath a Turbulent Boundary Layer," J. Fluid Mechanics, Vol. 22, Part 1, May 1965.

22. Gilchrist, R.B. Strawderman, W.A. "Experimental Hydrophone-Size Correction Factor for Boundary Layer Pressure Fluctuations," Journal of the Acoustical Society of America, Vol. 38, No. 2, p. 298, August 1965.

23. Schloemer, H.H. "Effects of Pressure Gradients on Turbulent Boundary Layer Wall Pressure Fluctuations" U.S. Navy Underwater Sound Laboratory, Report No. 747, July 1966.

24. Bradshaw, P. Ferriss, D.H. "The Response of a Retarded Equilibrium Turbulent Boundary Layer to the Sudden Removal of Pressure Gradient," National Physical Laboratory, Aero Report No. 1145, March 1965.

25. Belcher, P.M. "Predictions of Boundary-Layer-Turbulence Spectra and Correlations for Supersonic Flight" 5th Congres International D'Acoustique, Liege, 7-14 September 1965.

26. Bolt, Beranek and Newman, Inc. "Acoustic and Vibration Data from Titan III SSLV-3 Flight," Report No. 1256, July 1965.

27. Hilton, D.A. Bracalente, E.M. Hubbard, H.H. "In-Flight Aerodynamic Noise Measurements on a Scout Launch Vehicle," NASA TND-1818, July 1963.

28. Leech, F.J. Sackschewsky, V.E. "Boundary Layer Noise Measurements of the F-102 Aircraft," Wright-Patterson Air Force Base, Biomedical Laboratory, Tech. Documentary Report No. MRL-TDR-62-71, August 1962.

29. Murphy, J.S. Bies, D.A. Speaker, W.W. Franken, P.A. "Wind Tunnel Investigation of Turbulent Boundary Layer Noise as Related to Design Criteria for High Performance Vehicles," National Aeronautics and Space Administration, TND-2247, April 1964.

## REFERENCES


30. Bull, M.K. "Properties of the Fluctuating Wall-Pressure Field of a Turbulent Boundary Layer," NATO-AGARD Report 455, April 1963.

31. Serafini, J.S. "Wall-Pressure Fluctuations and Pressure-Velocity Correlations in a Turbulent Boundary Layer," NASA TR R-165, December 1963.

32. Bull, M.K. Willis, J.L. "Some Results of Experimental Investigations of the Surface Pressure Fields due to a Turbulent Boundary Layer," University of Southampton, AASU Report No. 199, November 1961.

33. Willmarth, W.W. Wooldridge, C.E. "Measurements of the Fluctuating Pressure at the Wall Beneath a Thick Turbulent Boundary Layer," J. of Fluid Mechanics, Vol. 14, p. 187, 1962.

34. Williams,D.J.M. "Measurements of the Surface Pressure Fluctuations in a Turbulent Boundary Layer in Air at Supersonic Speeds," University of Southampton, AASU Report 162, December 1960.

TABLE I

(SUBSONIC DATA)

| INVESTIGATOR | $U_\infty$(ft/sec) | M | $\delta$(in) | $\delta^*$(in) | $D/\delta^*$ | $\bar{U}_\tau/U_\infty$ | $\frac{\delta \bar{U}_\tau}{\nu_\infty} \times 10^{-3}$ |
|---|---|---|---|---|---|---|---|
| 1. Bull[30] | | 0.3 | .567 | .081 | .371 | .0351 | 3.20 |
| 2. Bull | | 0.3 | 1.04 | .149 | .201 | .0323 | 5.65 |
| 3. Bull | | 0.5 | .4 | .057 | .527 | .03515 | 3.59 |
| 4. Bull | | 0.5 | .882 | .126 | .238 | .0329 | 7.70 |
| 5. Bull | | 0.5 | 1.21 | .173 | .1735 | .0314 | 10.10 |
| 6. Bradshaw[24] | 110 | | 1.25 | | .80 | .0342 | 2.51 |
| 7. Schloemer[23] | 105 | | 1.05 | .1535 | | .0387 | 2.11 |
| 8. Serafini[31] | 656 | 0.6 | 1.29 | .19 | .329 | .0327 | 12.13 |
| 9. Speaker,Ailman[16] | 463 | 0.42 | .493 | .0661 | .907 | .0356 | 5.46 |
| 10. Speaker,Ailman | 634 | 0.59 | .380 | .0560 | 1.071 | .0339 | 5.20 |
| 11. Speaker,Ailman | 906 | 0.90 | .337 | .0514 | 1.17 | .0352 | 4.89 |
| 12. Willis[32] | 22.2 | | .63 | .084 | 2.02 | .0355 | 3.68 |
| 13. Willis | 19.45 | | .285 | .038 | 4.5 | .0397 | 1.635 |
| 14. Willmarth,Roos[21] | | | | | .122 | .03025 | 11.87 |
| 15. Willmarth & Wooldridge[33] | 206 | | 5.04 | .492 | .331 | .0326 | 17.90 |
| 16. Hubbard[27] | 740 | 0.67 | 8.25 | 1.14 | .219 | .0288 | 69.7 |

TABLE II
(PRESSURE GRADIENTS)

| | D | $U_\infty$ (Ft/sec) | $\delta^*$ (in.) | $\delta$ (in.) | $\frac{\nu_o}{\rho \bar{U}_\tau^3} \frac{dp}{dx}$ | $\bar{U}_\tau / U_\infty$ | $\frac{\delta \bar{U}_\tau}{\nu_o} \times 10^{-3}$ |
|---|---|---|---|---|---|---|---|
| 1. Bradshaw[24] | .125 | 110 | | 1.25 | 0 | .0342 | 2.51 |
| 2. Bradshaw | .125 | 110 | .488 | 2.80 | $8.66(10)^{-4}$ | .0366 | 6.06 |
| 3. Bradshaw | .125 | 110 | 1.081 | 4.0 | $34.0(10)^{-4}$ | .0248 | 6.60 |
| 4. Schloemer[23] | .398 | 105 | .1535 | 1.05 | 0 | .0387 | 2.11 |
| 5. Schloemer | .398 | 105 | .227 | 1.102 | $94.4(6)^{-4}$ | .0303 | 1.717 |
| 6. Scholemer | .398 | 157 | .0263 | 0.406 | -32.4 | .0474 | 1.402 |

TABLE III
(SUPERSONIC DATA)

| | $U_\infty$ (ft/sec) | M | $\delta$ (in.) | $\delta^*$ (in.) | $D/\delta^*$ | $\bar{U}_r/U_\infty$ | $\frac{\delta \bar{U}_r}{\nu_o} \times 10^{-3}$ |
|---|---|---|---|---|---|---|---|
| 1. Speaker & Ailman[16] | 1340 | 1.40 | .335 | .0661 | 2.01 | .556 | 3.84 |
| 2. Speaker & Ailman | 1583 | 1.81 | .420 | .1010 | 1.315 | .0359 | 4.27 |
| 3. Speaker & Ailman | 1872 | 2.52 | .580 | .1722 | .772 | .0362 | 4.46 |
| 4. Speaker & Ailman | 2110 | 3.45 | .812 | .3304 | .402 | .0363 | 4.37 |
| 5. Belcher[25] | 1260 | 1.30 | 5.95 | .972 | .257 | .0310 | 24.45 |
| 6. Belcher | 1550 | 1.60 | 5.86 | 1.06 | .236 | .032 | 25.2 |
| 7. Belcher | 1840 | 1.90 | 5.44 | 1.14 | .219 | .032 | 22.4 |
| 8. Williams[34] | 1180 | 1.2 | .108 | .02 | 8.5 | .0583 | .375 |
| 9. Williams | 1347 | 1.44 | .118 | .024 | 7.08 | .0469 | 1.39 |
| 10. Williams | 1417 | 1.54 | .137 | .03 | 5.66 | .0362 | 8.35 |
| 11. Titan III[17][26] | 1046 | 1.0 | 5.69 | .874 | .67 | .0297 | 52.2 |
| 12. Titan III | 1046 | 1.0 | 12.1 | 1.81 | | .0287 | 107.7 |
| 13. Leech[28] | 1180 | 1.16 | 1.13 | .204 | | .0308 | 7.25 |
| 14. Hubbard[27] | 1240 | 1.17 | 8.15 | 1.26 | .199 | .0306 | 84. |
| 15. Hubbard | 1900 | 1.82 | 8.25 | 1.565 | .16 | .030 | 57.8 |
| 16. Hubbard | 2260 | 2.23 | 8.15 | 1.71 | .146 | .0309 | 43.7 |
| 17. Hubbard | 3370 | 3.30 | 8.25 | 2.36 | .106 | .035 | 12.8 |
| 18. Hubbard | 4040 | 4.08 | 9.61 | 3.91 | .064 | .043 | 1.85 |

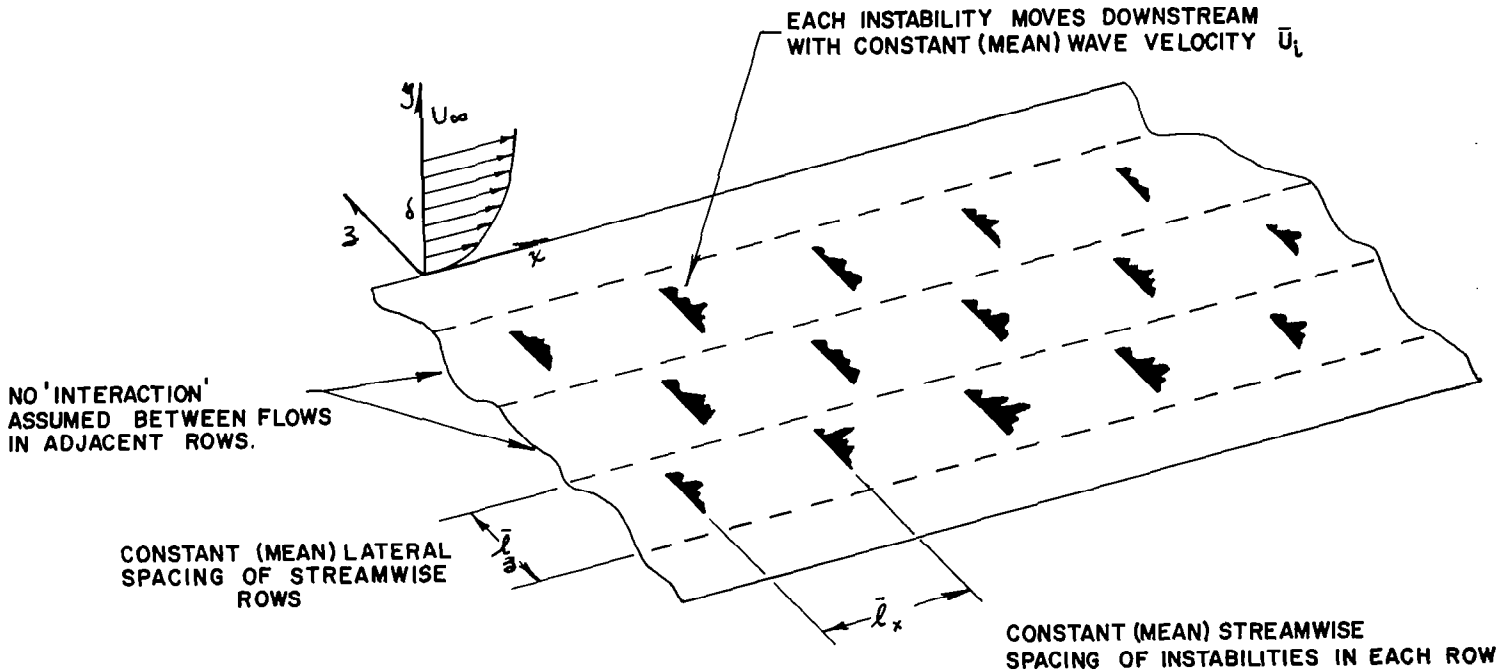


FIGURE 1. SIMPLIFIED MODEL OF INSTABILITY DISTRIBUTION OVER WALL IN FULLY DEVELOPED WALL TURBULENCE.

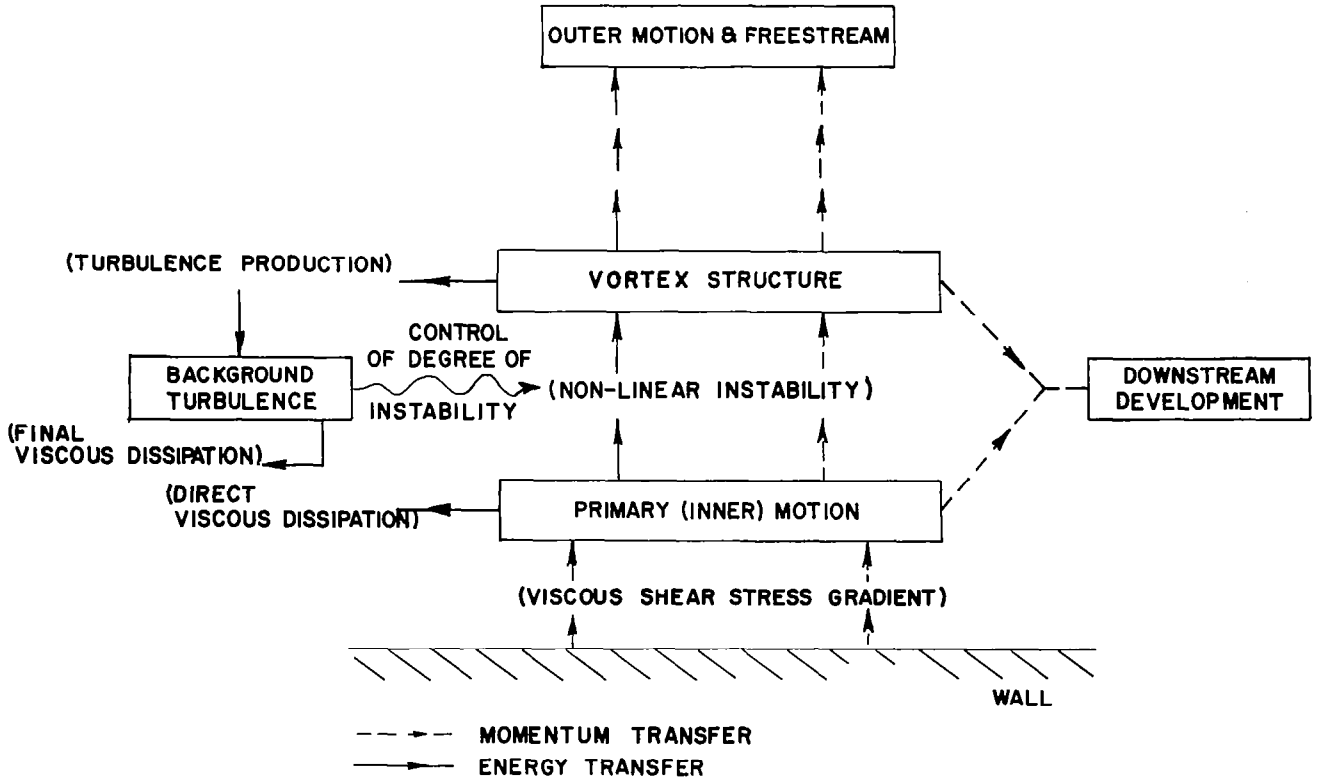


FIGURE 2. SCHEMATIC REPRESENTATION OF THE PROCESS OF ENERGY AND MOMENTUM TRANSFER FROM THE WALL OUTWARDS ACCORDING TO INITIAL FLOW MODEL

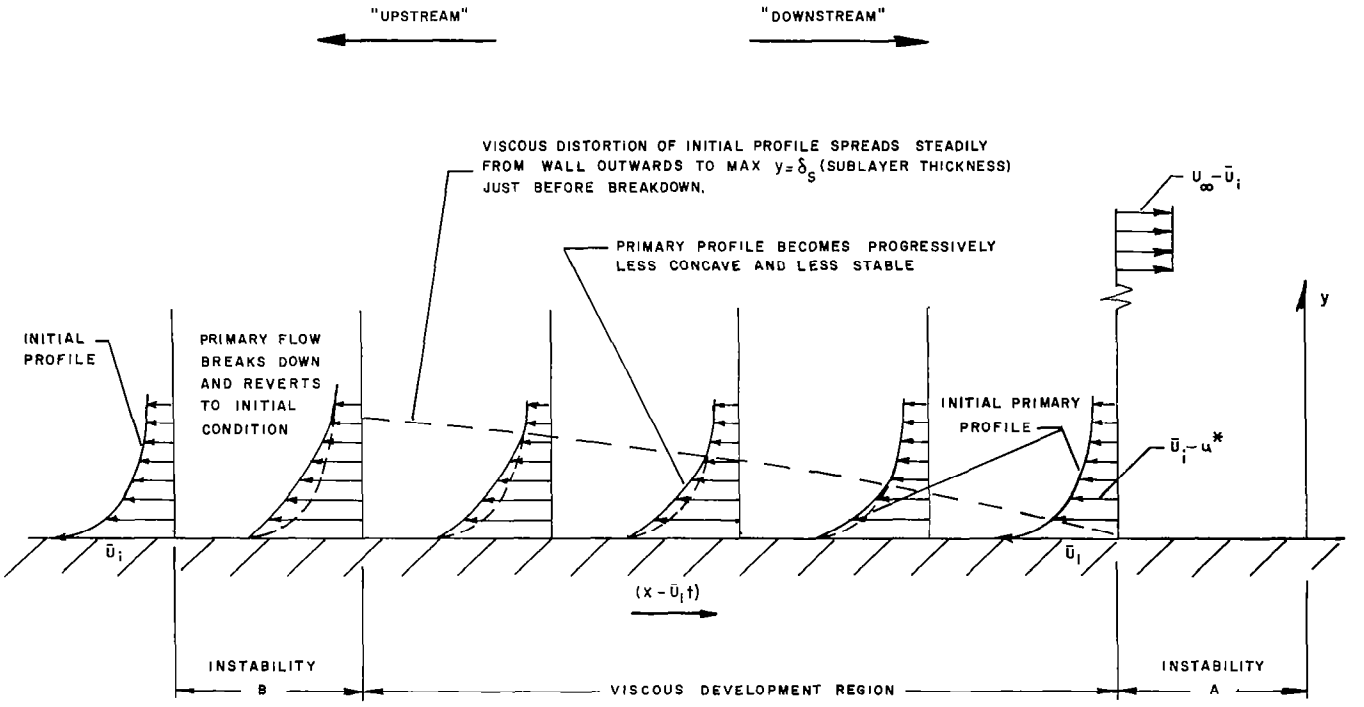


FIGURE 3. DEVELOPMENT AND BREAKDOWN OF PRIMARY MOTION

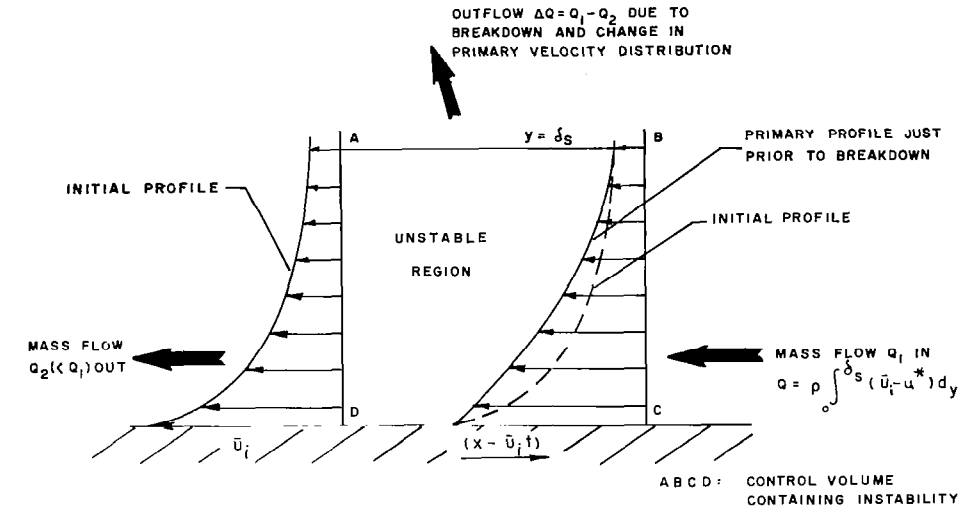


FIGURE 4a MASS TRANSPORT THROUGH BREAKDOWN REGION

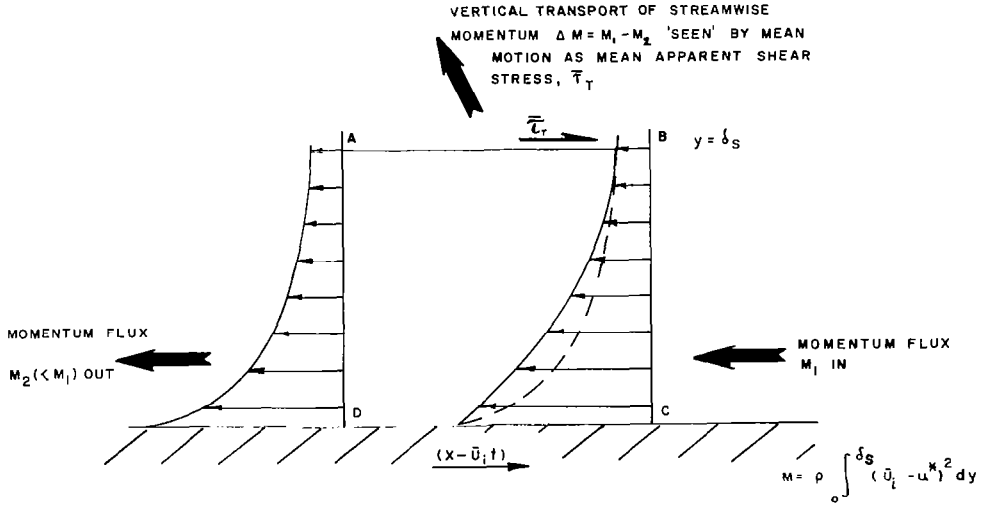


FIGURE 4b MOMENTUM TRANSPORT THROUGH BREAKDOWN REGION

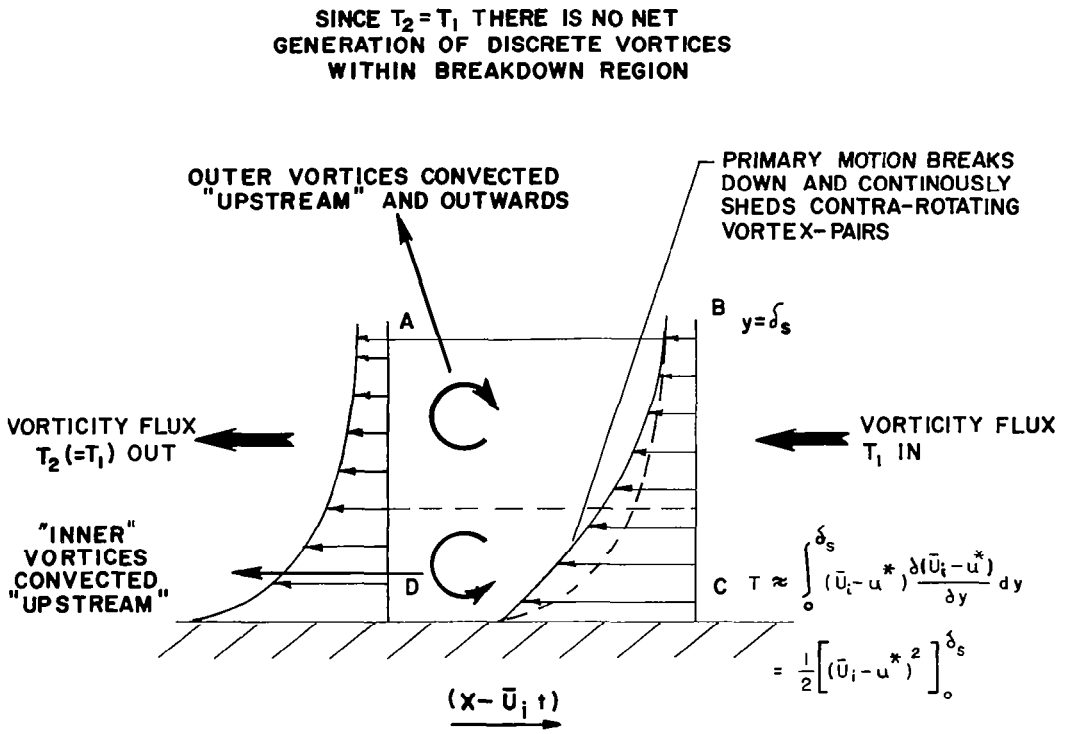


FIGURE 4c. VORTICITY TRANSPORT THROUGH BREAKDOWN REGION

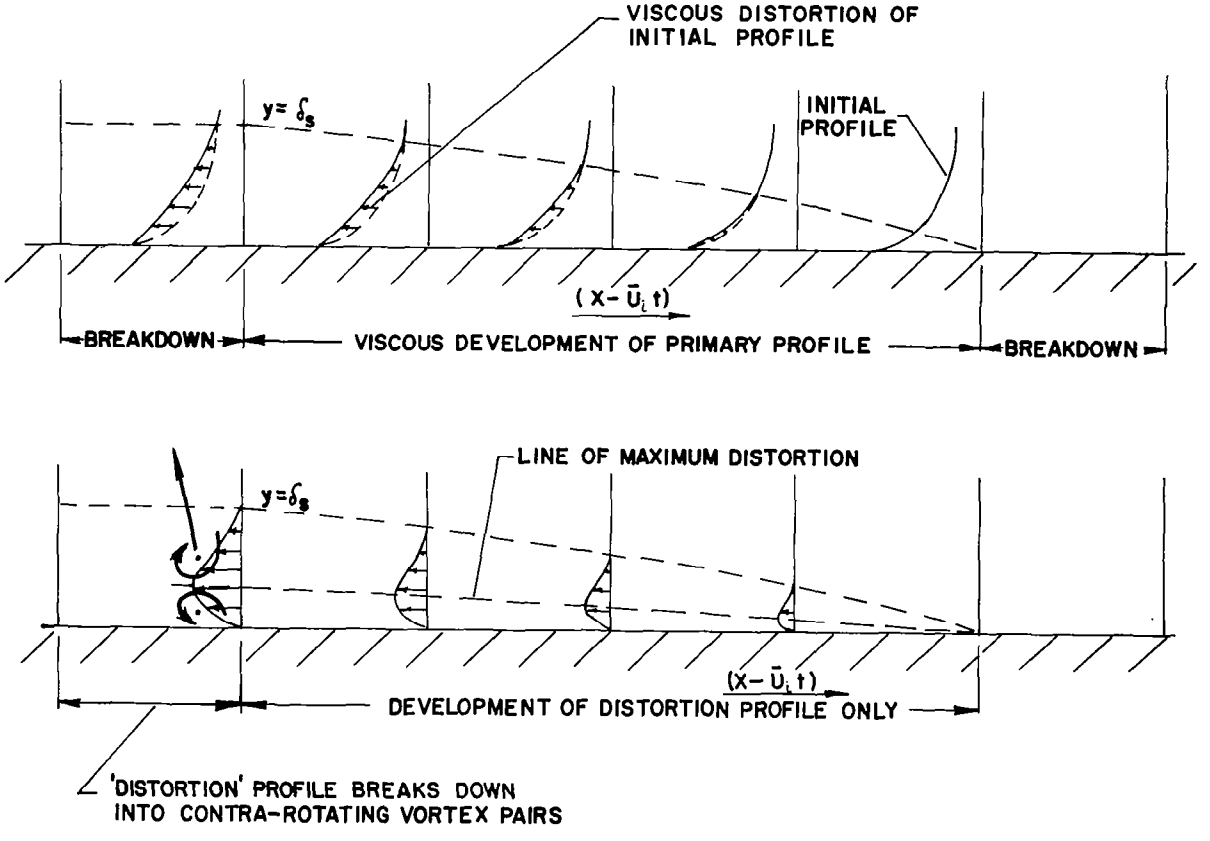


FIGURE 5. VORTEX-PAIR GENERATION EXPLAINED BY BREAKDOWN OF VISCOUS 'DISTORTION' PROFILE

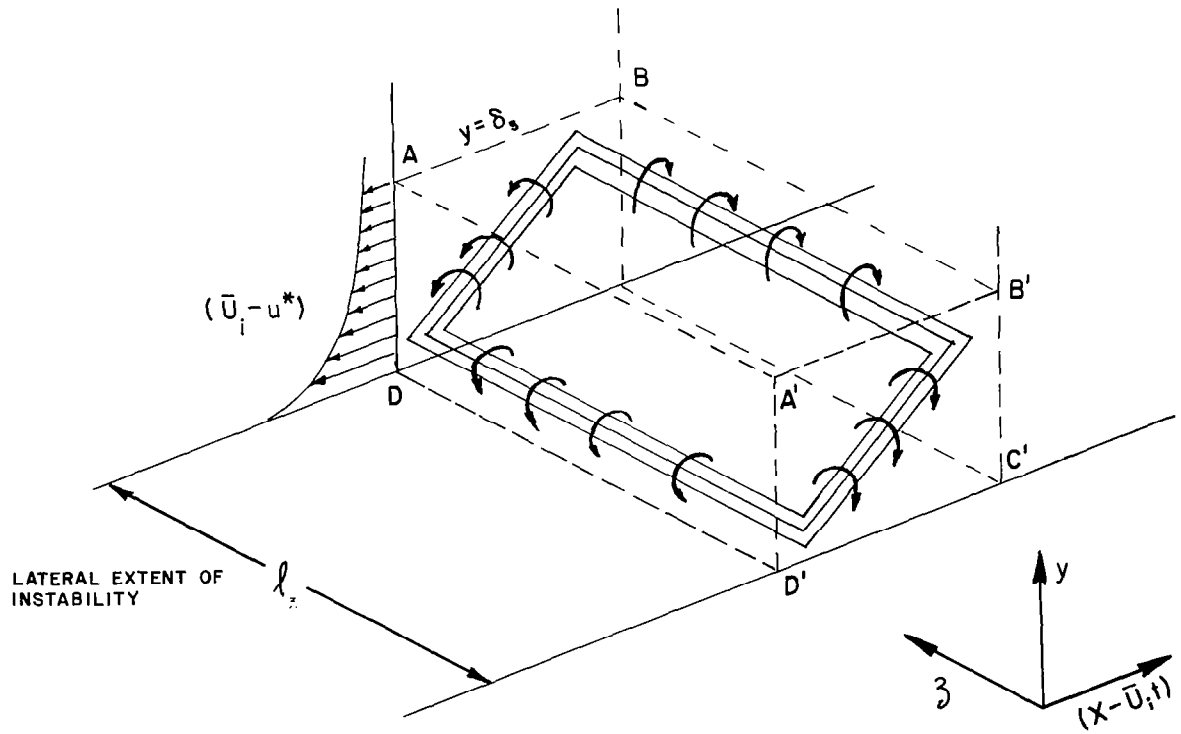


FIGURE 6. GENERATION OF RING-VORTICES BY INSTABILITY IN ACTUAL SHEAR LAYER

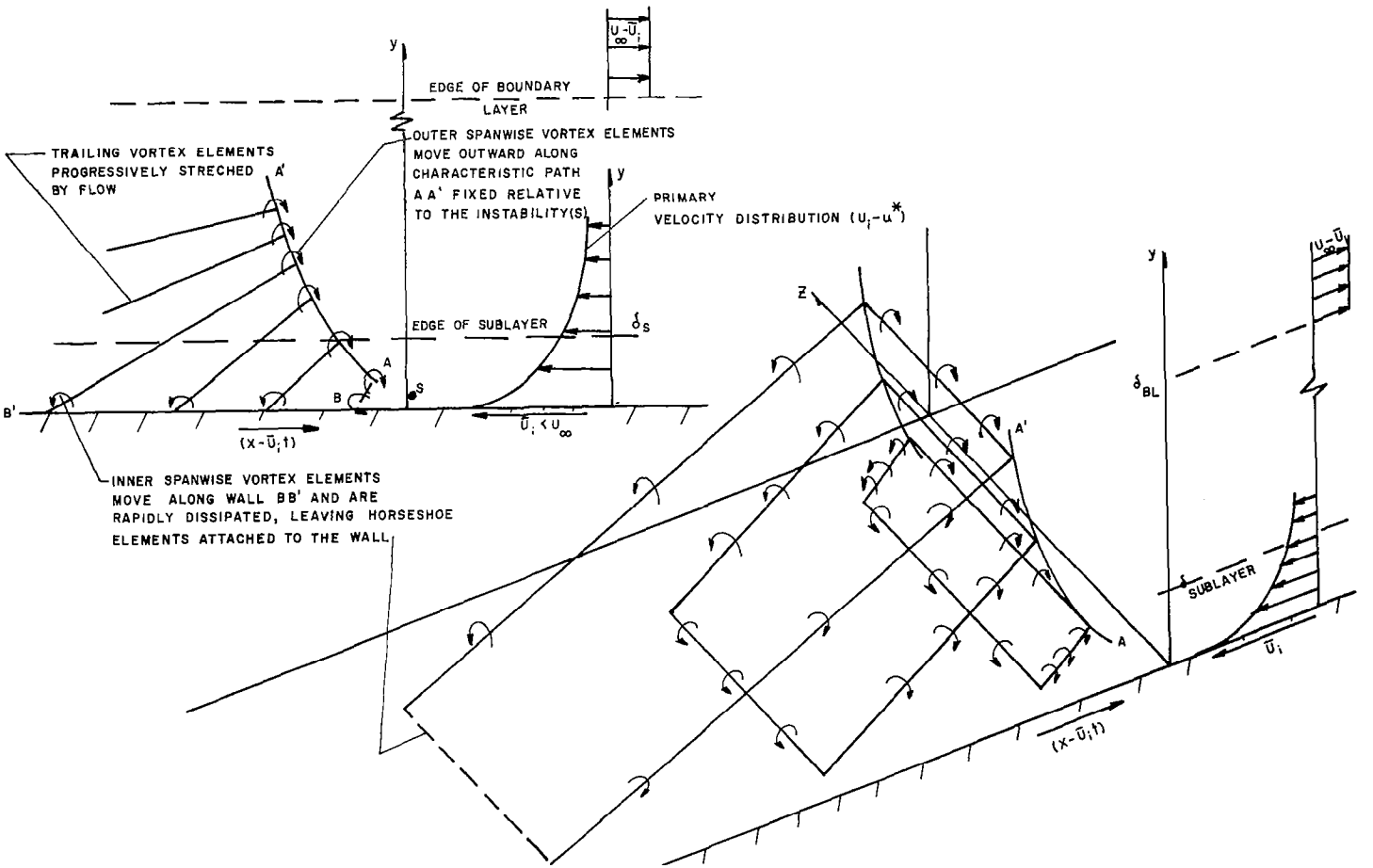


FIGURE 7. SCHEMATIC DIAGRAM OF VORTEX STRUCTURE GENERATED BY INSTABILITY
(MOVING AXES REPRESENTATION)

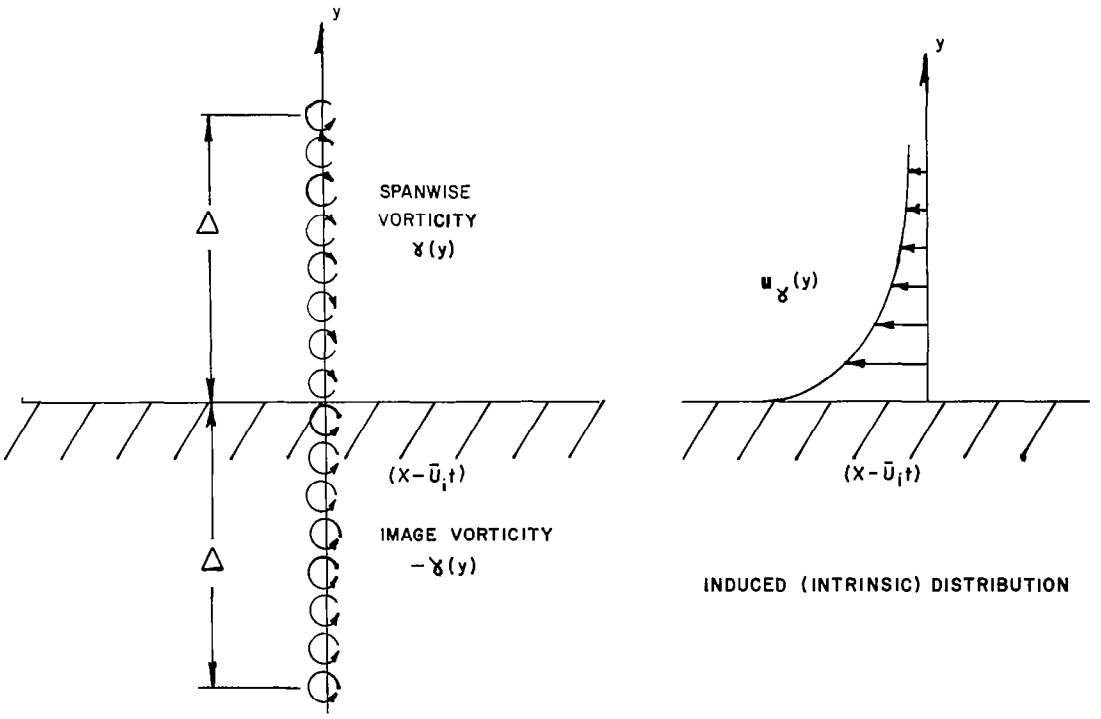


$$u_\gamma(y) = \frac{1}{2\pi}\int_0^\Delta \frac{\gamma\, dy'}{y'-y} + \frac{1}{2\pi}\int_0^\Delta \frac{\gamma\, dy'}{y'+y}$$

SPANWISE VORTICITY IMAGE VORTICITY

FIGURE 8: SELF-INDUCED MOTION OF VORTEX STRUCTURE (INTRINSIC VELOCITY DISTRIBUTION)

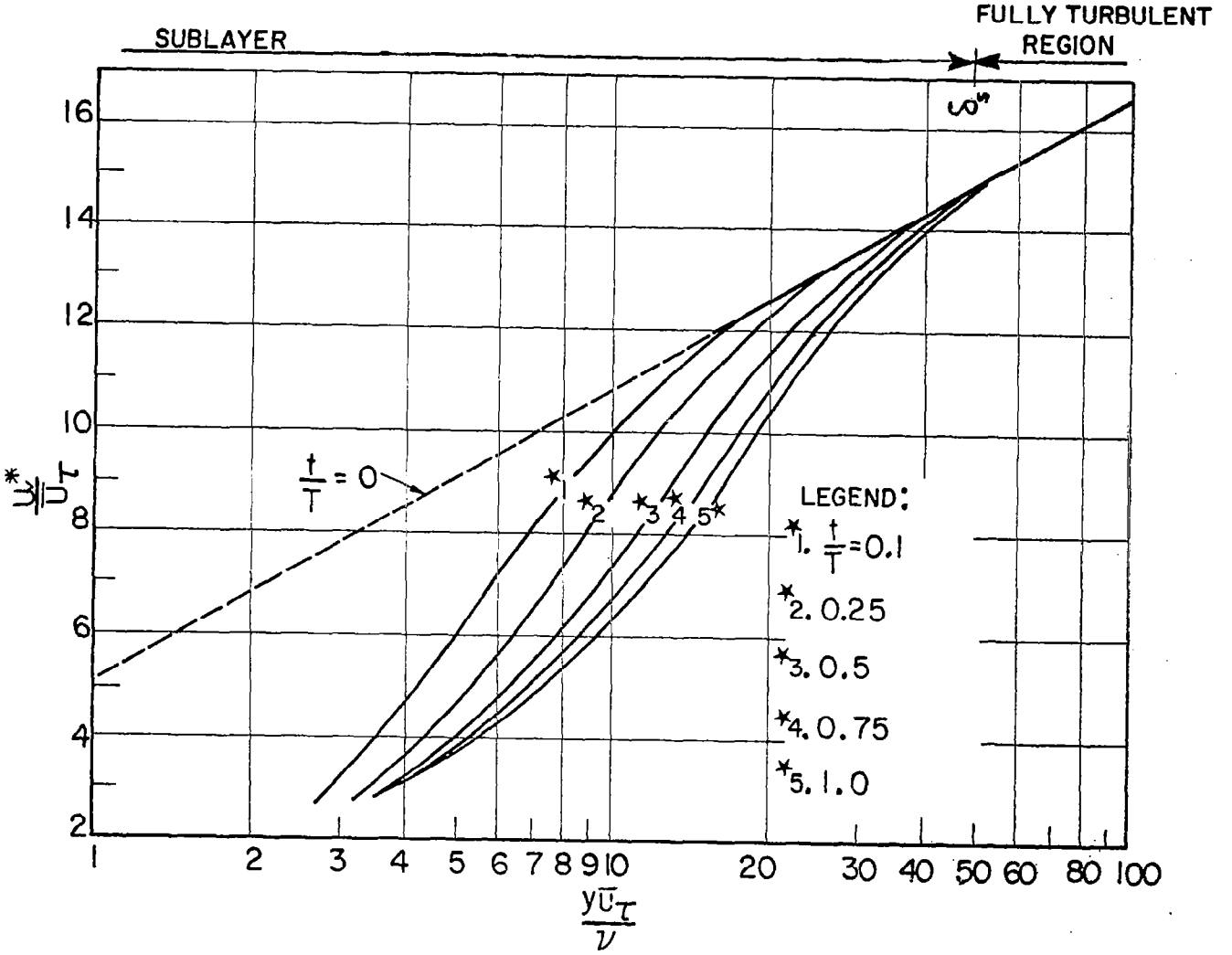


FIGURE 9 PRIMARY VELOCITY DISTRIBUTIONS

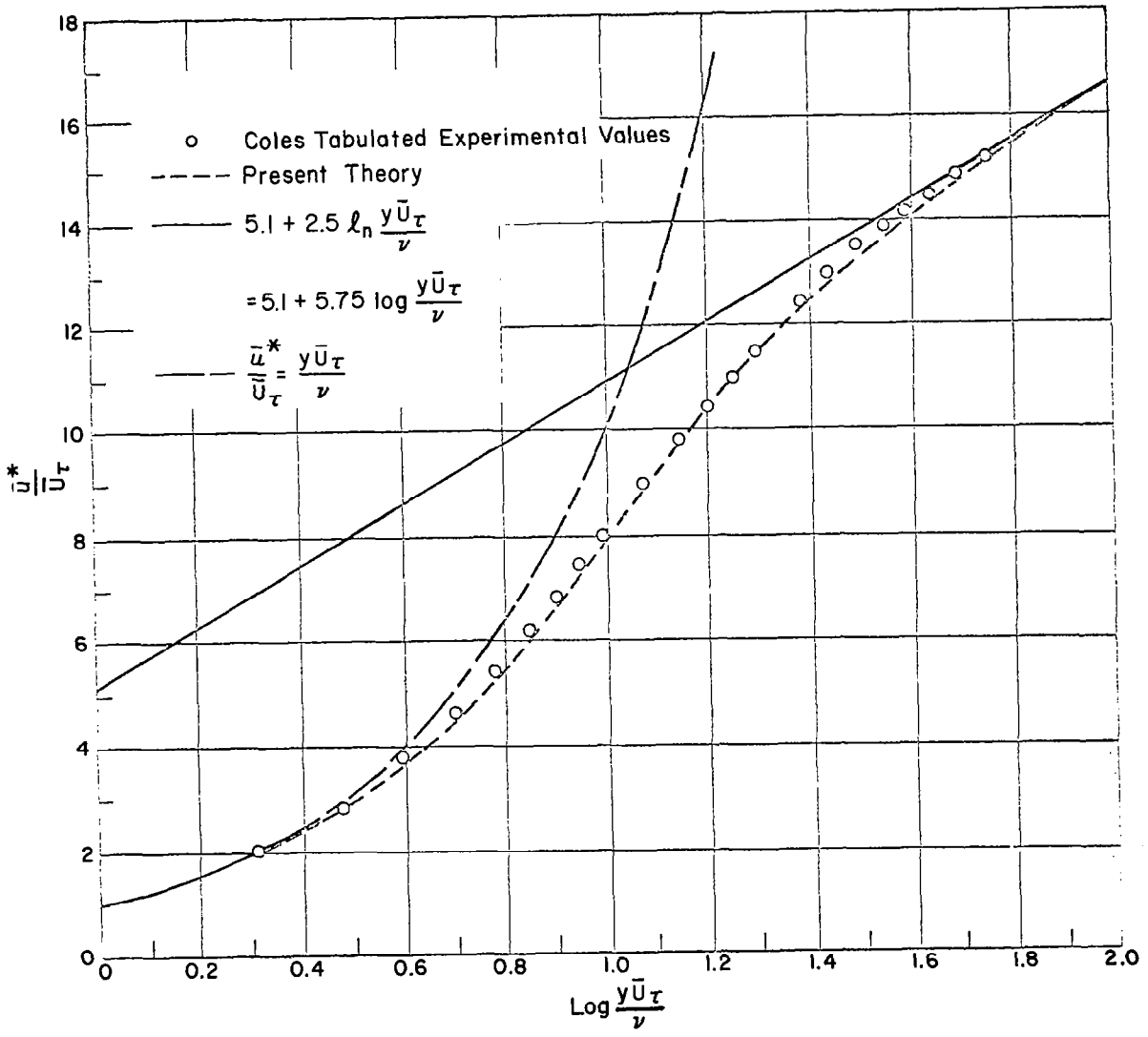


FIGURE 10 MEAN VELOCITY DISTRIBUTION

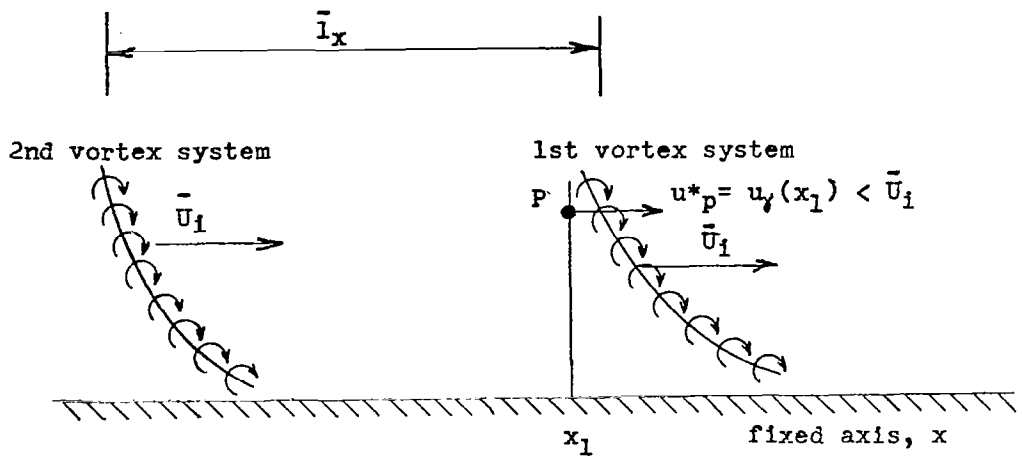


Fig. 11a, $t = t_1$, Particle P at $x_1$ immediately after passage of first vortex system.

$$x_1 - x_2 = \frac{\bar{l}_x\, u^*_p}{(\bar{U}_1 - u^*_p)}, \qquad t_2 - t_1 = \frac{\bar{l}_x}{(\bar{U}_1 - u^*_p)}$$

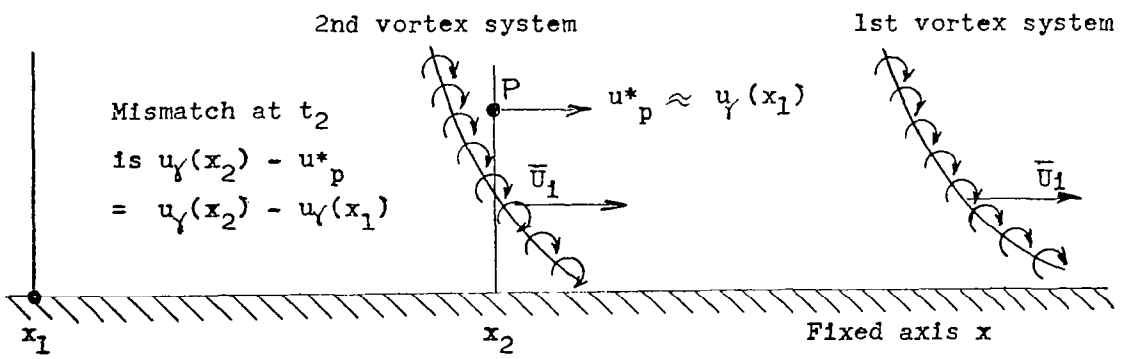


Fig. 11b $t = t_2$, Particle P at $x_2$ immediately before passage of 2nd vortex system

**Fig. 11.** Downstream (Reynold's Number) Growth Effect on Primary Motion.

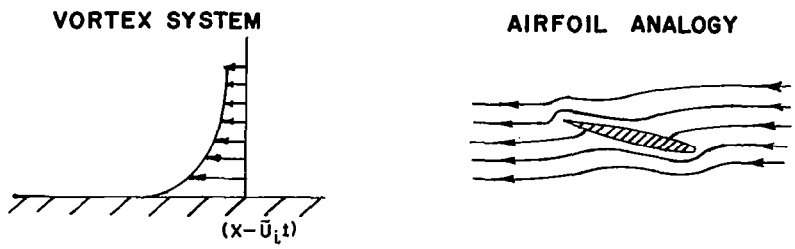


12a. 'POTENTIAL' SOLUTION NO BREAKDOWN, NO VORTEX SHEAR STRESS.

'POTENTIAL' SOLUTION, NO LIFT.

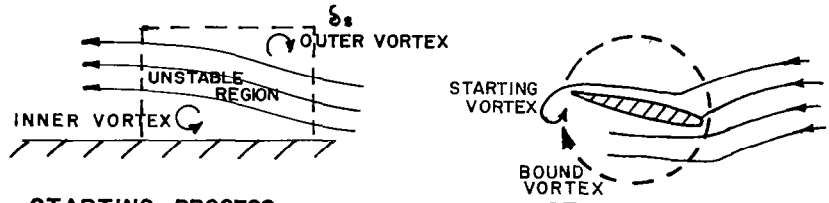


12b. STARTING PROCESS

STARTING PROCESS

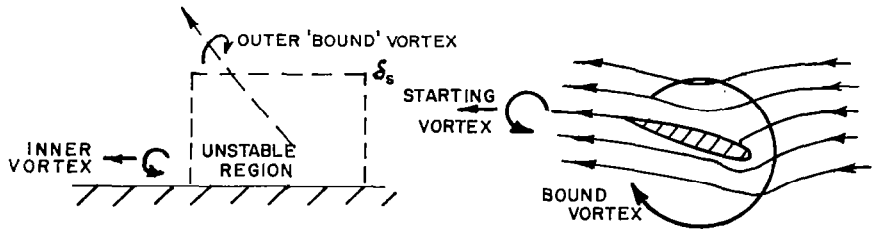


12c. VORTEX SYSTEM ESTABLISHED

LIFT ESTABLISHED

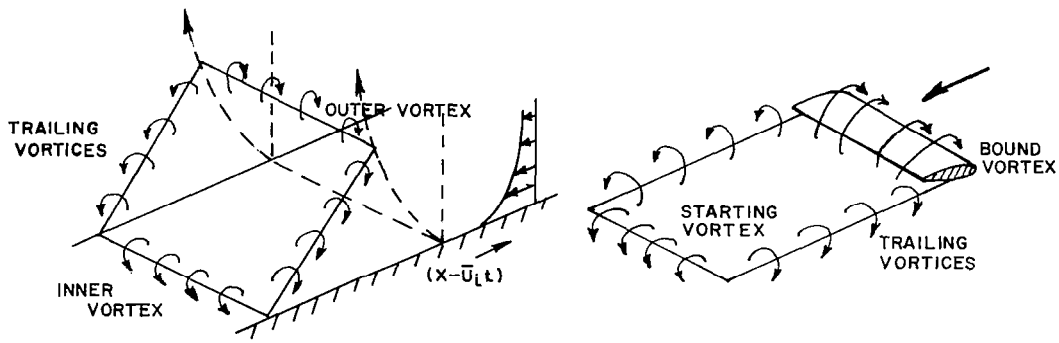


12d. VORTEX SYSTEM FOR INSTABILITY OF FINITE WIDTH

VORTEX SYSTEM FOR FINITE AIRFOIL

FIGURE 12 LIFT AIRFOIL ANALOGY

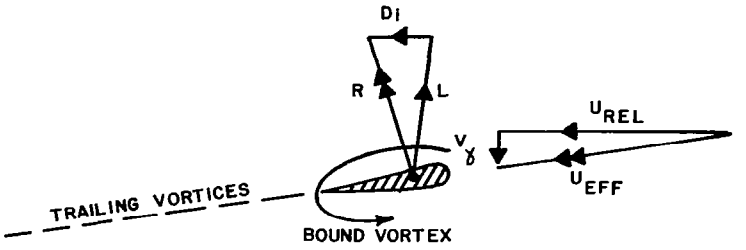


13 a. INDUCED DRAG ON FINITE AIRFOIL

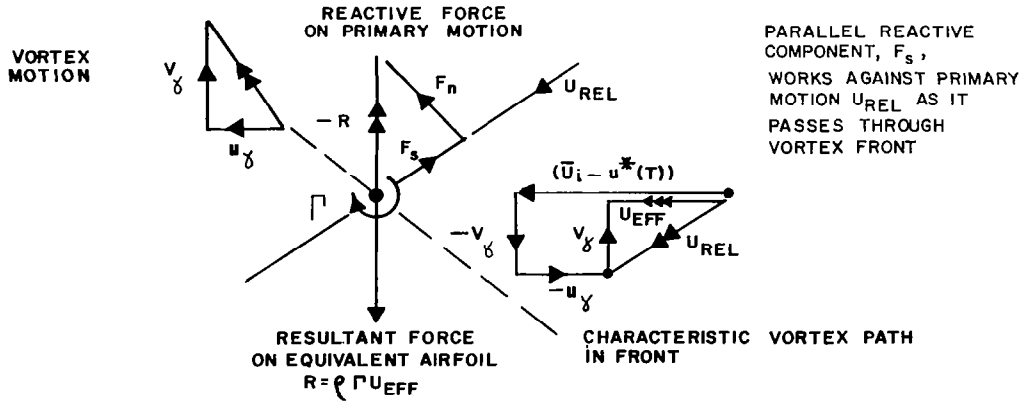


13 b. LIFTING AIRFOIL ANALOGY $\left[\bar{U}_i - u^*(T)\right] > u_\gamma$

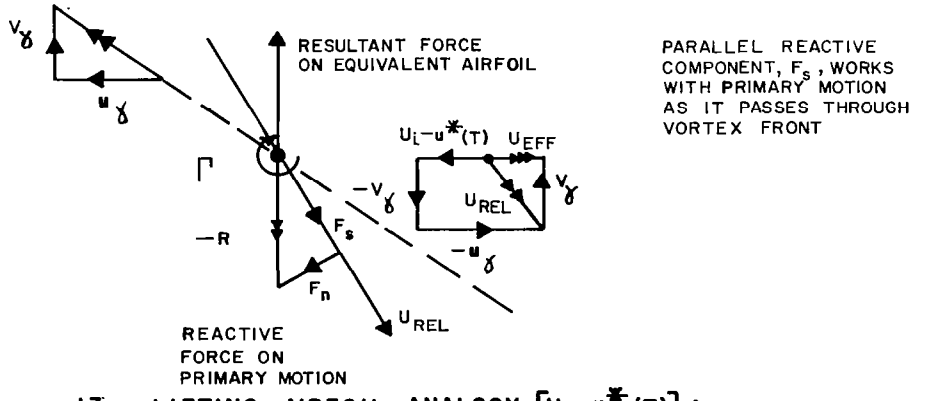


13 c. LIFTING AIRFOIL ANALOGY $\left[U_i - u^*(T)\right] > u_\gamma$

FIGURE 13 ANALOGY BETWEEN VORTEX INTERACTION AND INDUCED DRAG

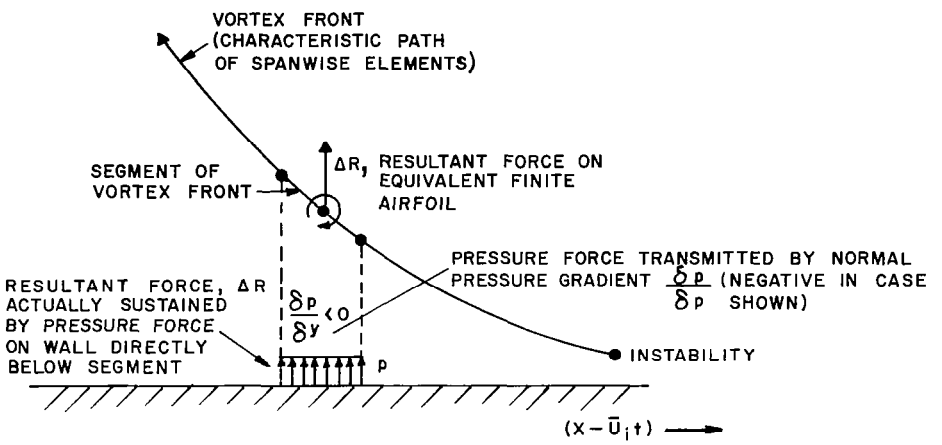


14a. GENERATION OF WALL PRESSURE BY VORTEX INTERACTION

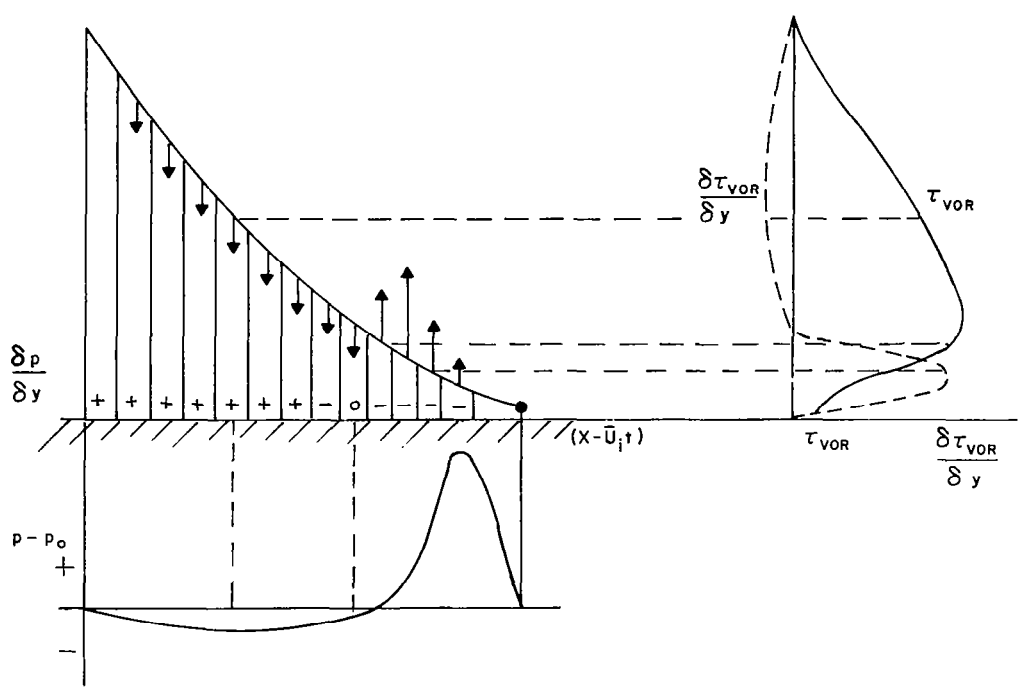


14b. TYPICAL PRESSURE SIGNATURE UNDER VORTEX SYSTEM

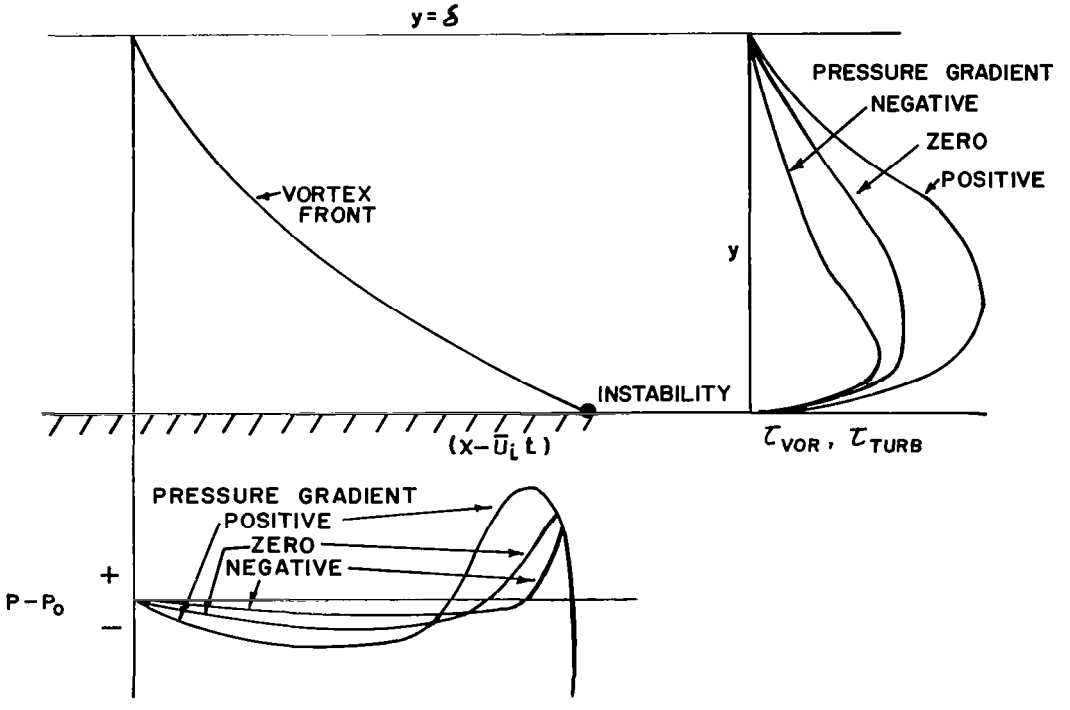


FIGURE 15 EFFECT OF STREAMWISE PRESSURE GRADIENT ON WALL PRESSURE SIGNATURE

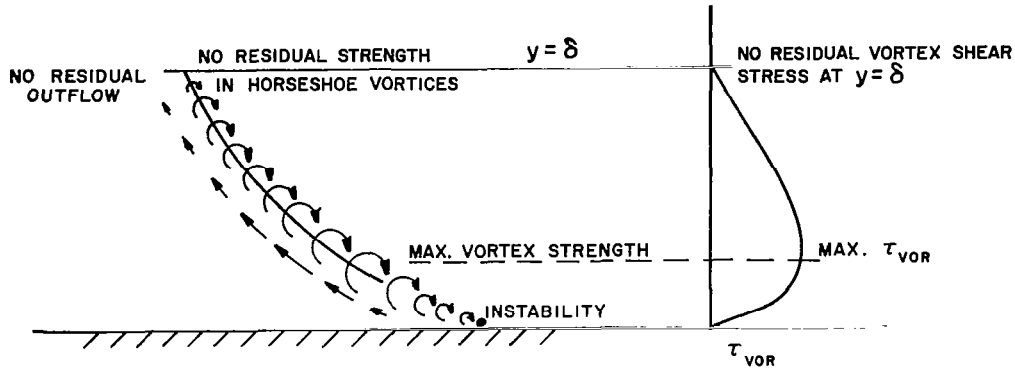


16 a. SPECIAL CASE OF ZERO RESIDUAL VORTEX SHEAR STRESS

(PIPE, CHANNEL FLOWS, AND BOUNDARY LAYER FLOW WITH UNIQUELY PRESCRIBED NEGATIVE PRESSURE GRADIENT.)

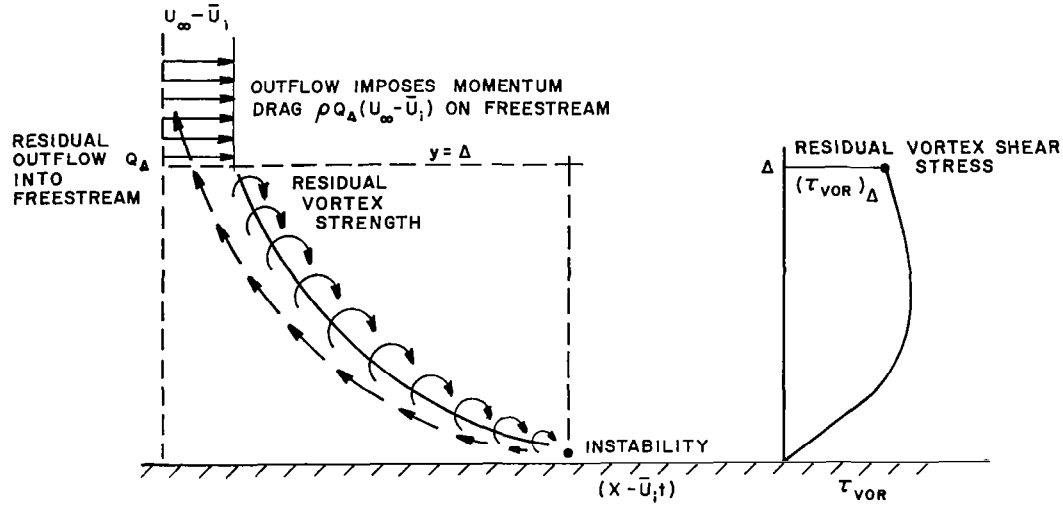


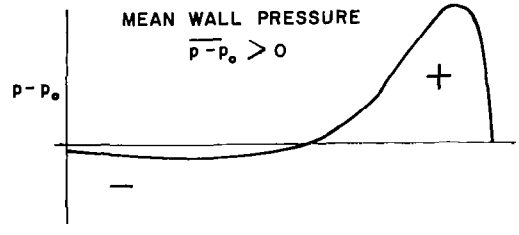


16 b. GENERAL CASE OF RESIDUAL VORTEX SHEAR STRESS

FIGURE 16. 'OUTER' FLOW MECHANISM ARISING FROM RESIDUAL VORTEX SHEAR STRESS

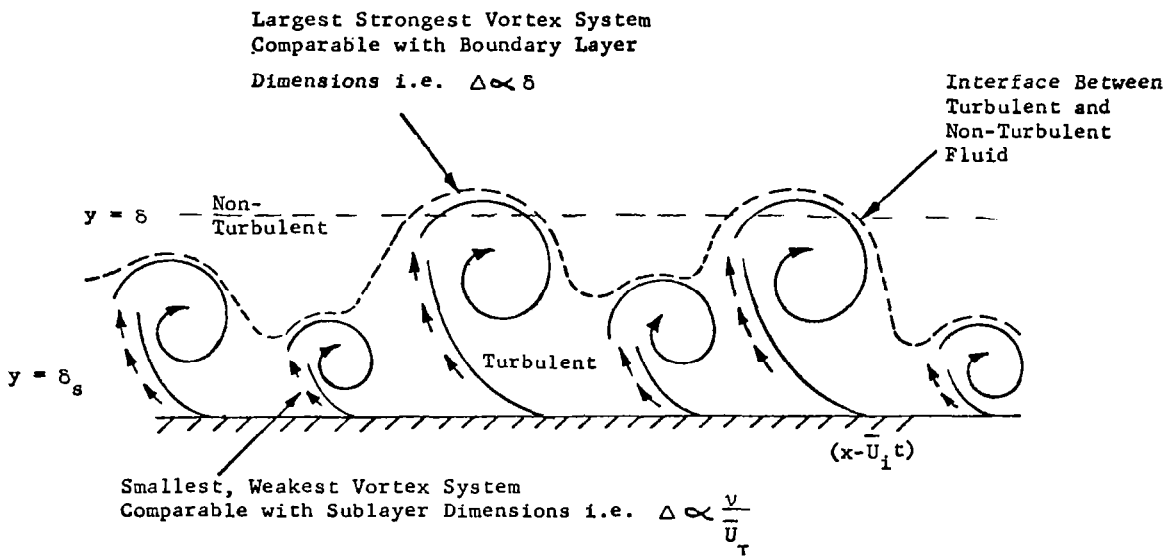


Fig. 17 Intermittency Explained by Random Variation in Strength of Consecutive Vortex Systems

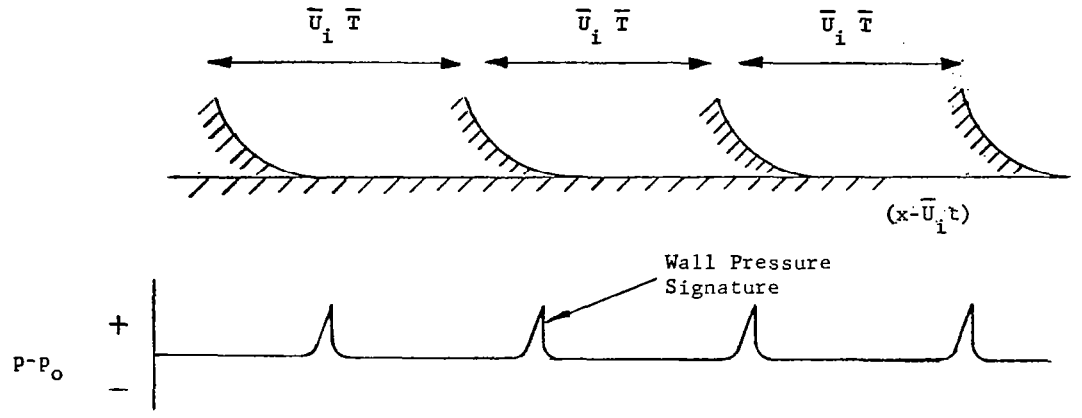


Fig. 18a "Ideal Flow" Model with Regularly Spaced Vortex Systems of Identical Strength.

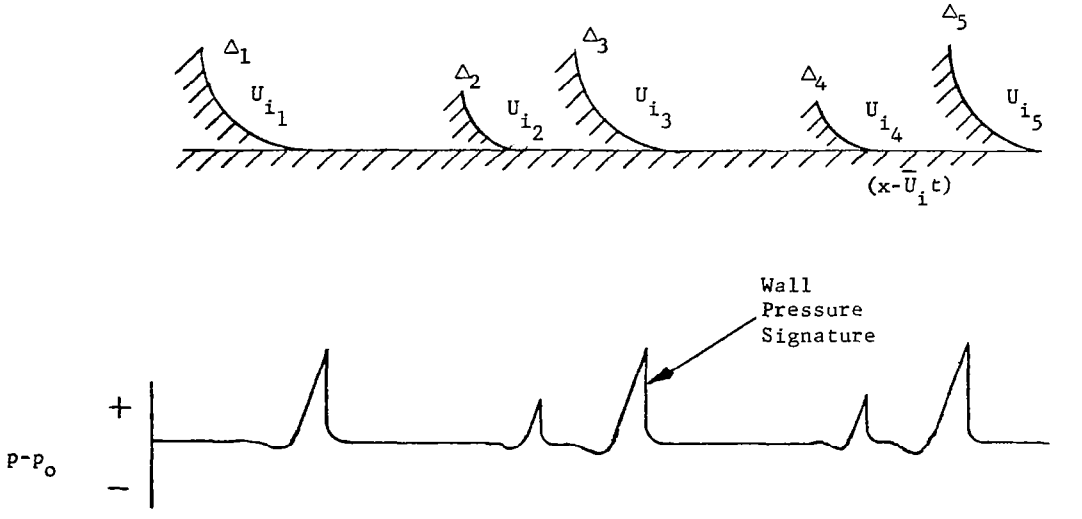


Fig. 18b "Real Flow" Model with Strength, Spacing and Wave Velocity of Vortex Systems Randomly Distributed above Corresponding Mean Values

Fig. 18. "Ideal" and "Real" Flow Models of the Wall Pressure Field

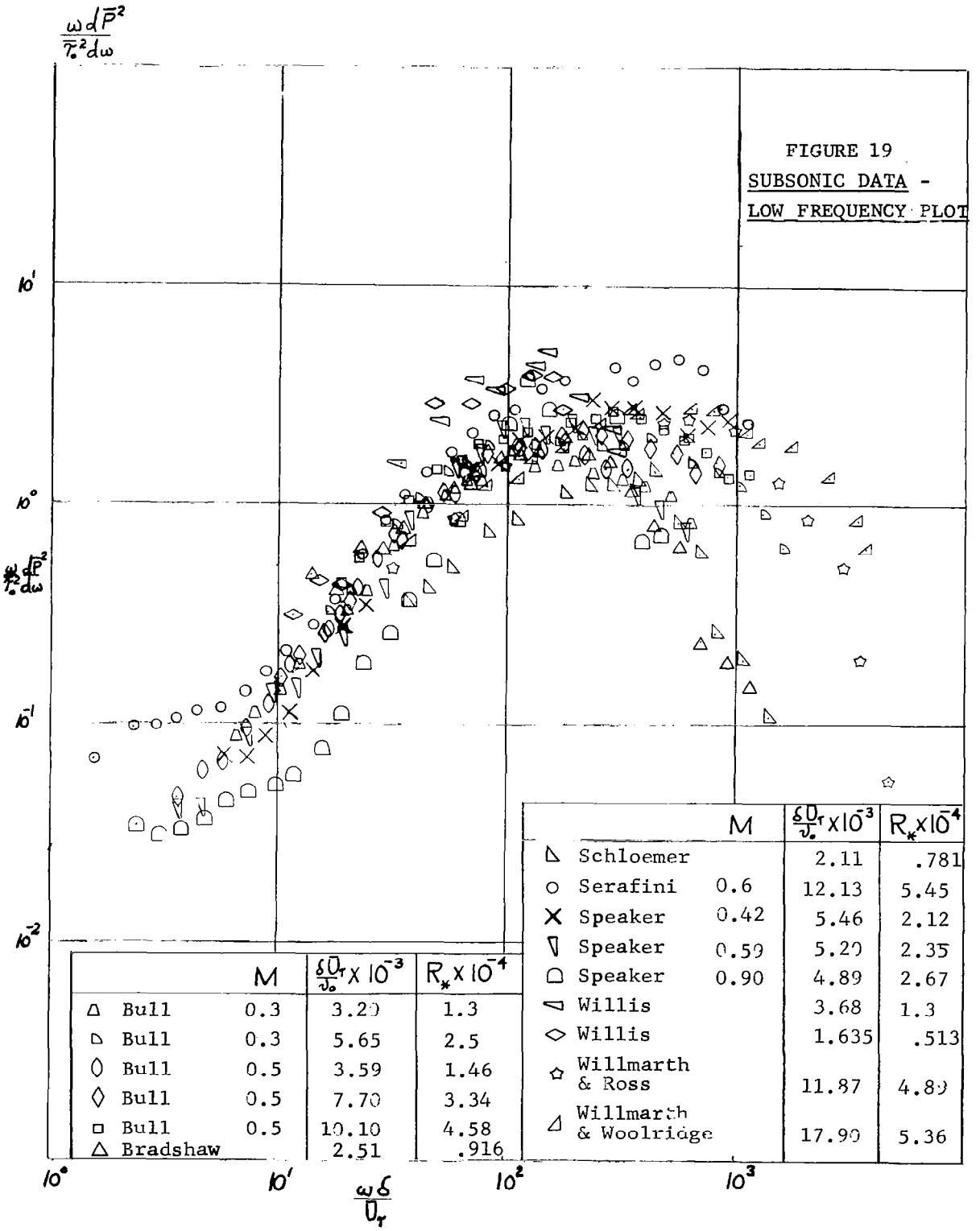


FIGURE 19
SUBSONIC DATA -
LOW FREQUENCY PLOT

| | | M | $\frac{\delta U_\tau}{U_o} \times 10^{-3}$ | $R_* \times 10^{-4}$ |
|---|---|---|---|---|
| △ | Bull | 0.3 | 3.20 | 1.3 |
| ▷ | Bull | 0.3 | 5.65 | 2.5 |
| ◯ | Bull | 0.5 | 3.59 | 1.46 |
| ◇ | Bull | 0.5 | 7.70 | 3.34 |
| □ | Bull | 0.5 | 10.10 | 4.58 |
| △ | Bradshaw | | 2.51 | .916 |

| | | M | $\frac{\delta U_\tau}{U_o} \times 10^{-3}$ | $R_* \times 10^{-4}$ |
|---|---|---|---|---|
| △ | Schloemer | | 2.11 | .781 |
| ○ | Serafini | 0.6 | 12.13 | 5.45 |
| × | Speaker | 0.42 | 5.46 | 2.12 |
| ▽ | Speaker | 0.59 | 5.20 | 2.35 |
| ▢ | Speaker | 0.90 | 4.89 | 2.67 |
| ◁ | Willis | | 3.68 | 1.3 |
| ◇ | Willis | | 1.635 | .513 |
| ☆ | Willmarth & Ross | | 11.87 | 4.89 |
| ◁ | Willmarth & Woolridge | | 17.90 | 5.36 |

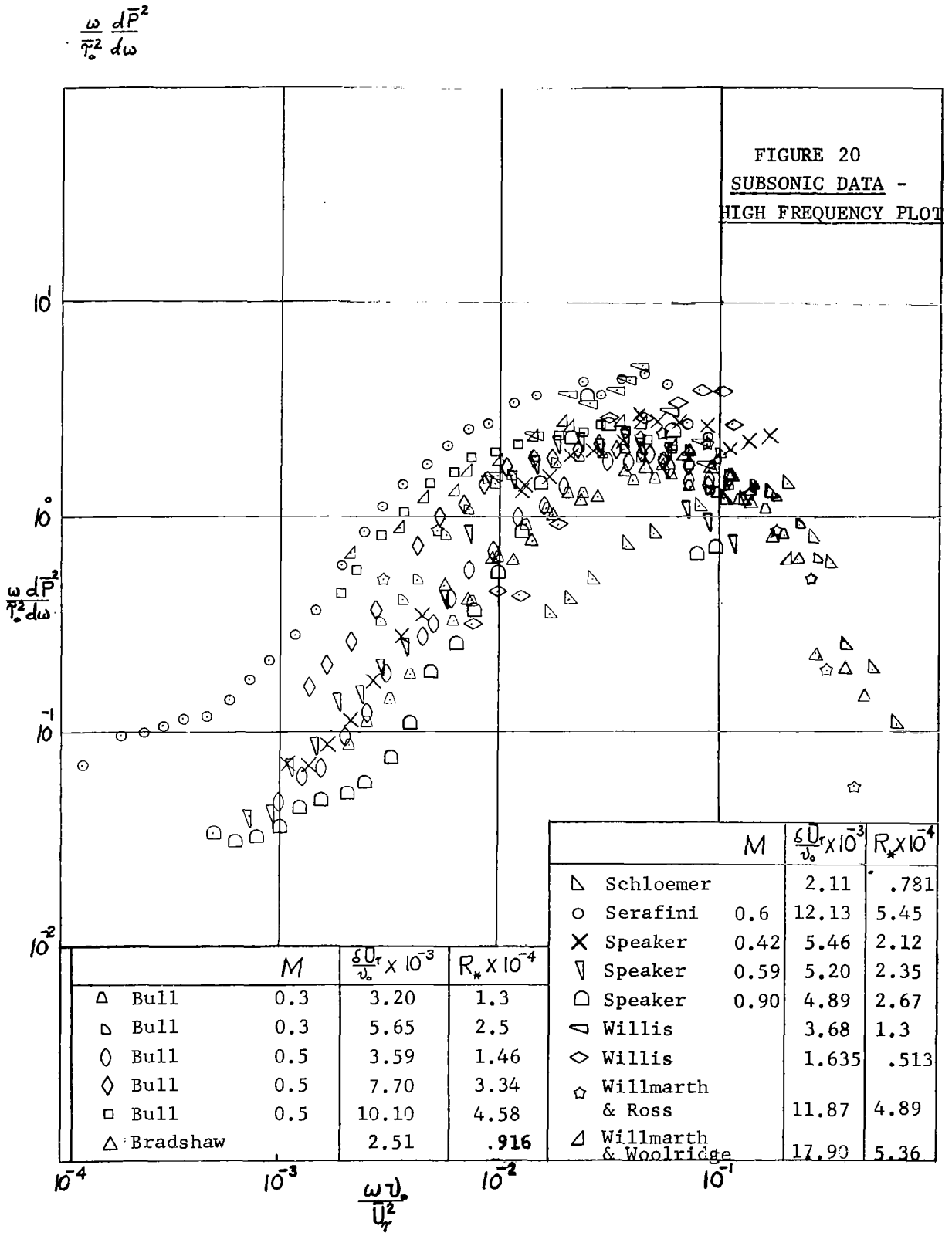
$\frac{\omega}{\bar{\tau}_o^2}\frac{d\bar{P}^2}{d\omega}$
FIGURE 20
SUBSONIC DATA -
HIGH FREQUENCY PLOT
$10^1$
$10^0$
$10^{-1}$
$10^{-2}$
$\frac{\omega d\bar{P}^2}{\bar{\tau}_o^2 d\omega}$
$10^{-4}$
$10^{-3}$
$10^{-2}$
$10^{-1}$
$\frac{\omega v_o}{U_\tau^2}$
M | $\frac{\delta U_\tau}{v_o} \times 10^{-3}$ | $R_* \times 10^{-4}$
Bull 0.3 | 3.20 | 1.3
Bull 0.3 | 5.65 | 2.5
Bull 0.5 | 3.59 | 1.46
Bull 0.5 | 7.70 | 3.34
Bull 0.5 | 10.10 | 4.58
Bradshaw | 2.51 | .916
M | $\frac{\delta U_\tau}{v_o} \times 10^{-3}$ | $R_* \times 10^{-4}$
Schloemer | 2.11 | .781
Serafini 0.6 | 12.13 | 5.45
Speaker 0.42 | 5.46 | 2.12
Speaker 0.59 | 5.20 | 2.35
Speaker 0.90 | 4.89 | 2.67
Willis | 3.68 | 1.3
Willis | 1.635 | .513
Willmarth & Ross | 11.87 | 4.89
Willmarth & Woolridge | 17.90 | 5.36

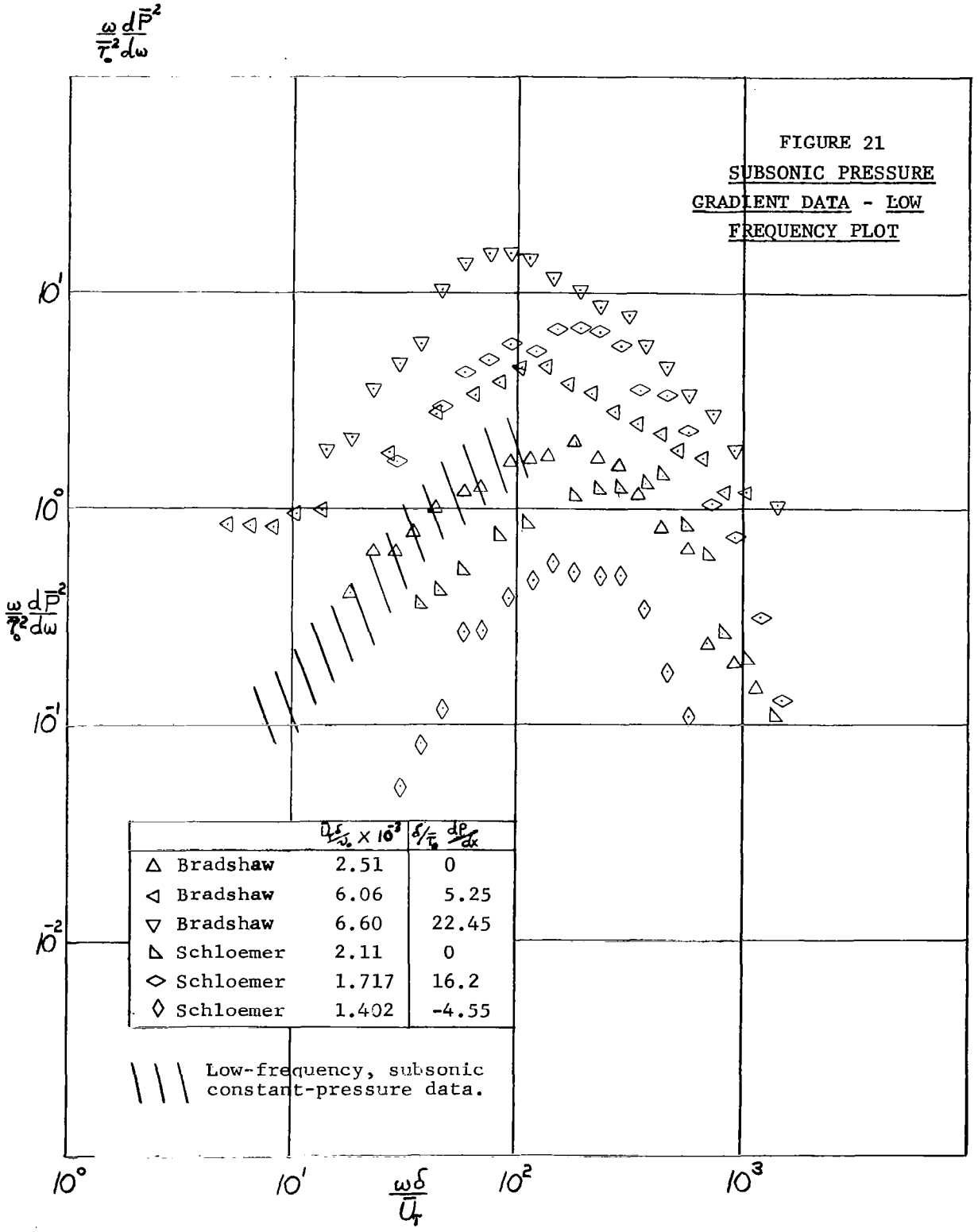
$\frac{\omega}{\bar{\tau}_w^2}\frac{d\bar{P}^2}{d\omega}$
FIGURE 21
SUBSONIC PRESSURE GRADIENT DATA - LOW FREQUENCY PLOT
$10^1$
$10^0$
$10^{-1}$
$10^{-2}$
$\frac{\omega}{\bar{\tau}_w^2}\frac{d\bar{P}^2}{d\omega}$
$10^0$
$10^1$
$10^2$
$10^3$
$\frac{\omega\delta}{\bar{U}_1}$
$\frac{\bar{U}_1\delta}{\nu_w} \times 10^{-3}$
$\frac{\delta}{\bar{\tau}_w}\frac{dp}{dx}$
△ Bradshaw 2.51 0
◁ Bradshaw 6.06 5.25
▽ Bradshaw 6.60 22.45
◺ Schloemer 2.11 0
◇ Schloemer 1.717 16.2
◊ Schloemer 1.402 -4.55
Low-frequency, subsonic constant-pressure data.

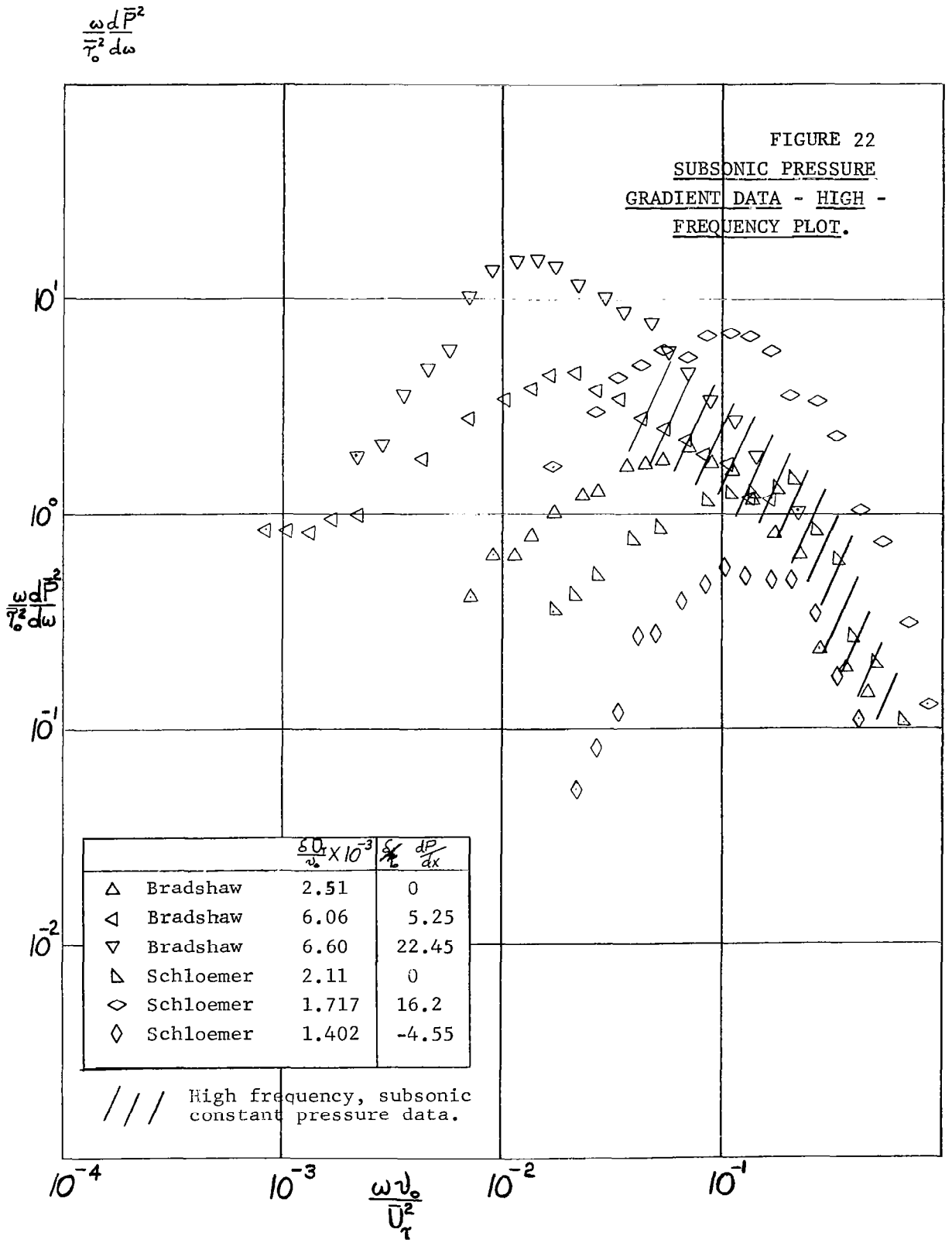


FIGURE 22
SUBSONIC PRESSURE GRADIENT DATA - HIGH - FREQUENCY PLOT.

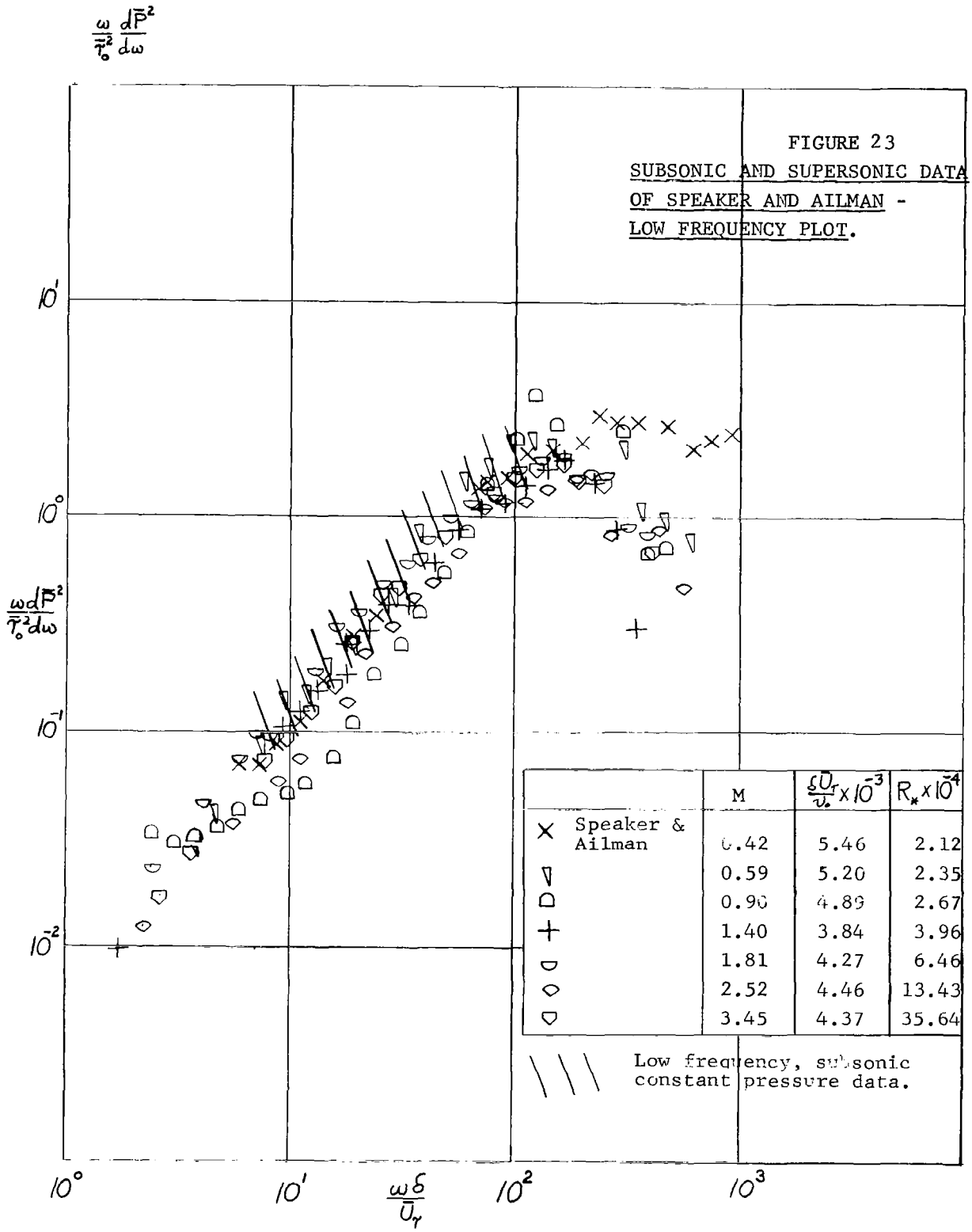


FIGURE 23
SUBSONIC AND SUPERSONIC DATA OF SPEAKER AND AILMAN - LOW FREQUENCY PLOT.

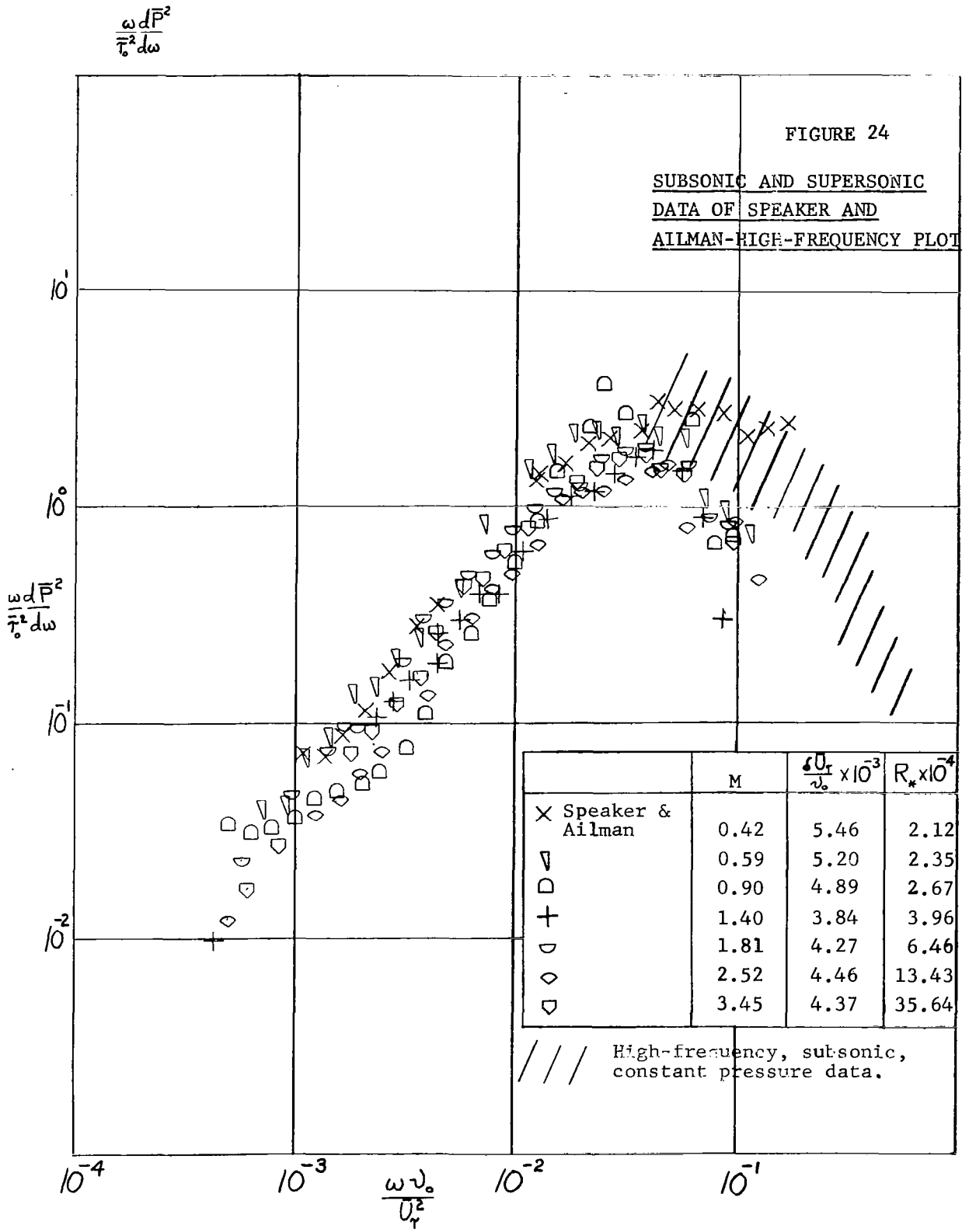
$\frac{\omega d\bar{P}^2}{\bar{\tau}_o^2 d\omega}$
$10^1$
$10^0$
$10^{-1}$
$10^{-2}$
$10^{-4}$
$10^{-3}$
$10^{-2}$
$10^{-1}$
$\frac{\omega \nu_o}{U_\tau^2}$
FIGURE 24
SUBSONIC AND SUPERSONIC DATA OF SPEAKER AND AILMAN-HIGH-FREQUENCY PLOT
M
$\frac{\delta U_\tau}{\nu_o} \times 10^{-3}$
$R_* \times 10^{-4}$
× Speaker & Ailman 0.42 5.46 2.12
0.59 5.20 2.35
0.90 4.89 2.67
1.40 3.84 3.96
1.81 4.27 6.46
2.52 4.46 13.43
3.45 4.37 35.64
High-frequency, subsonic, constant pressure data.

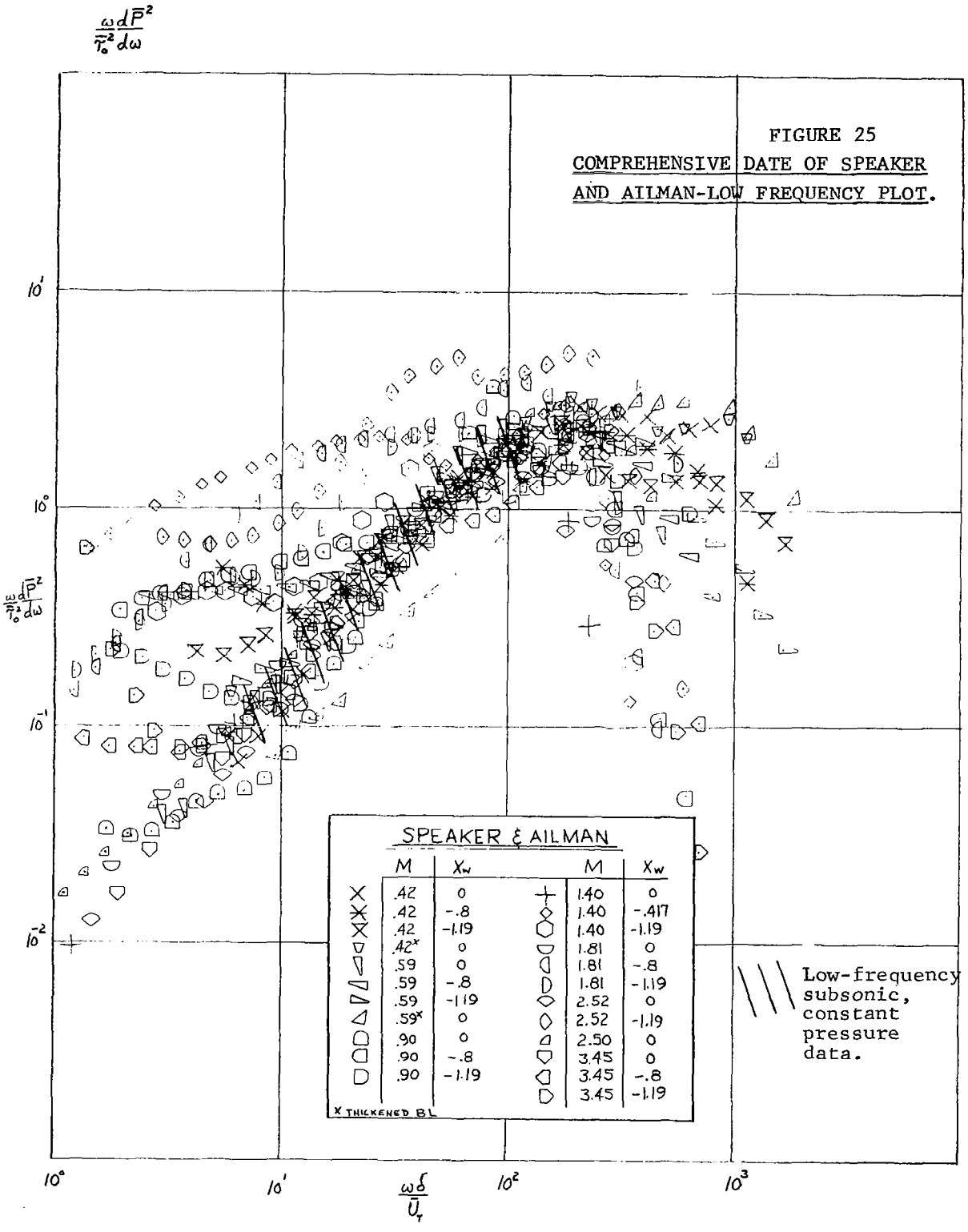


FIGURE 25
COMPREHENSIVE DATE OF SPEAKER AND AILMAN-LOW FREQUENCY PLOT.

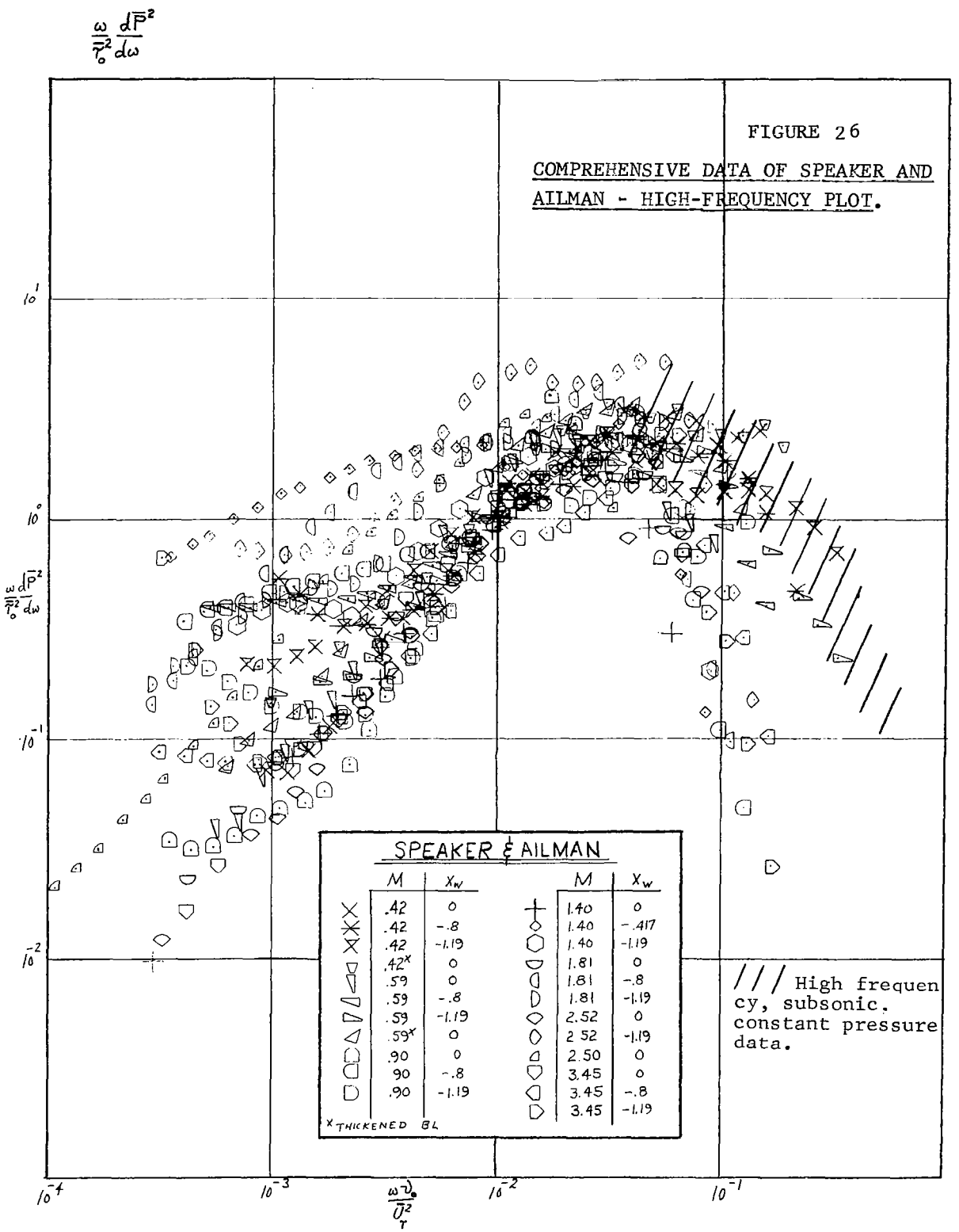


FIGURE 26

COMPREHENSIVE DATA OF SPEAKER AND AILMAN - HIGH-FREQUENCY PLOT.

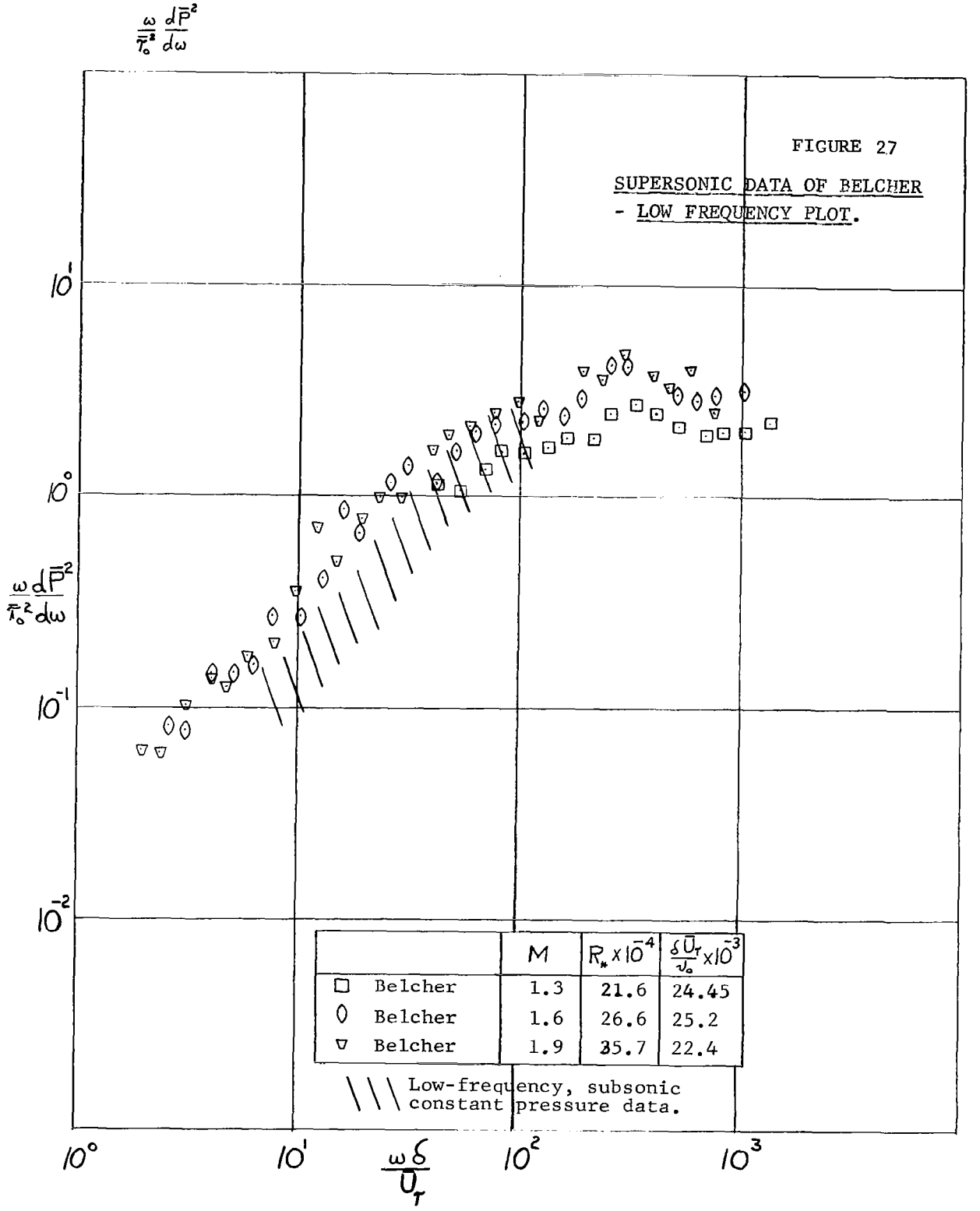


FIGURE 27

SUPERSONIC DATA OF BELCHER - LOW FREQUENCY PLOT.

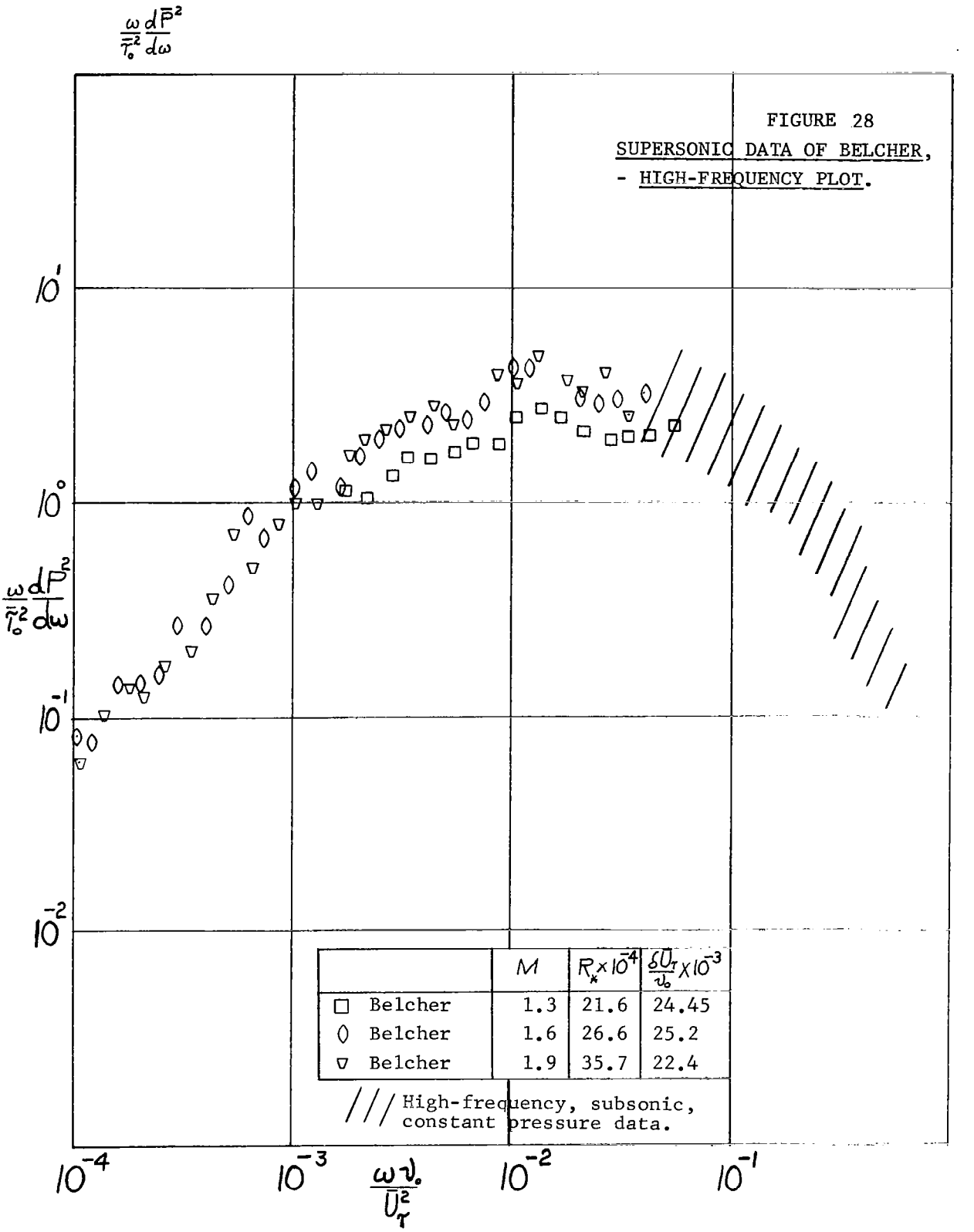


FIGURE 28
SUPERSONIC DATA OF BELCHER, - HIGH-FREQUENCY PLOT.

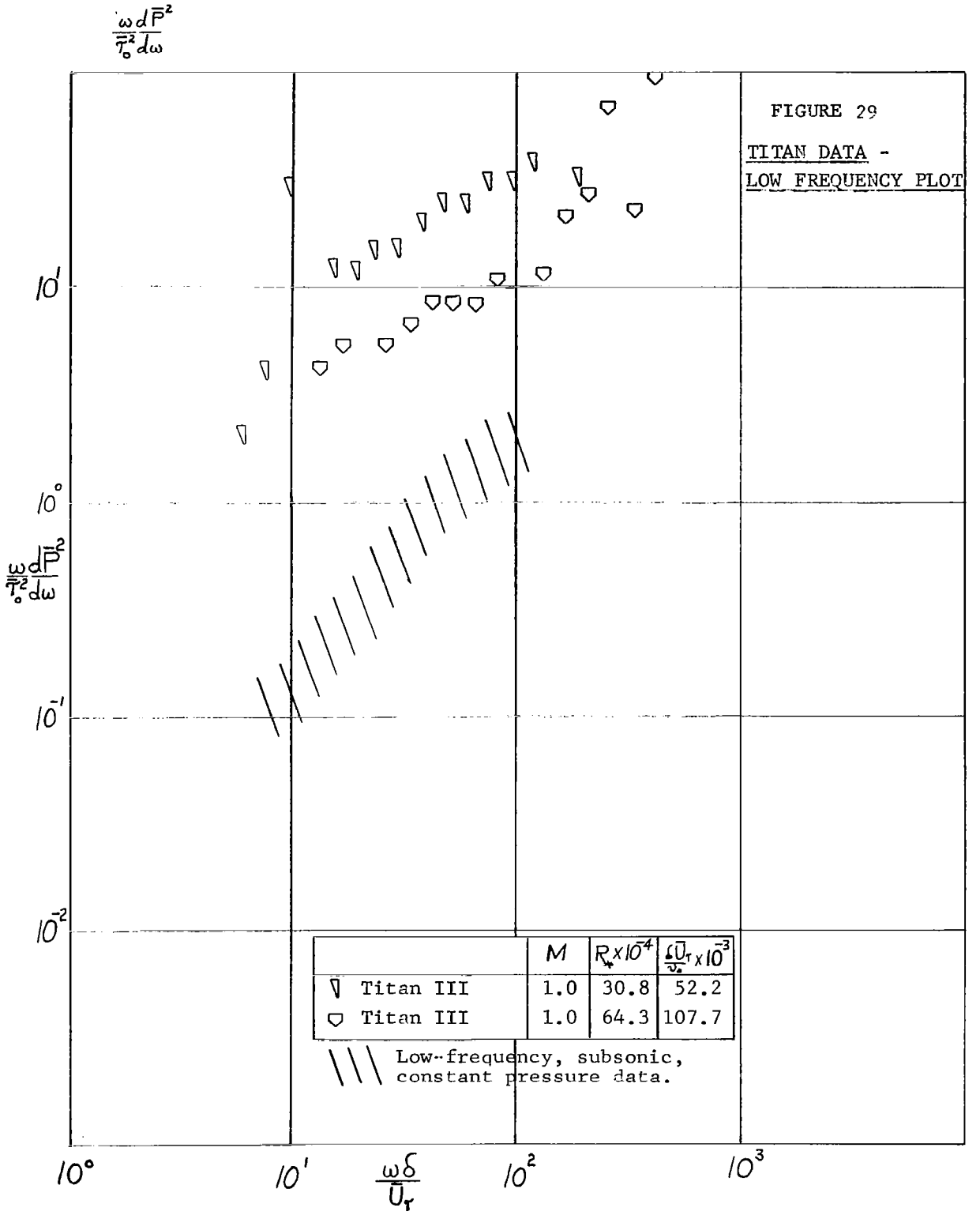


| | M | $R_\delta \times 10^{-4}$ | $\frac{\bar{U}_T}{\nu_o} \times 10^{-3}$ |
|---|---|---|---|
| Titan III | 1.0 | 30.8 | 52.2 |
| Titan III | 1.0 | 64.3 | 107.7 |

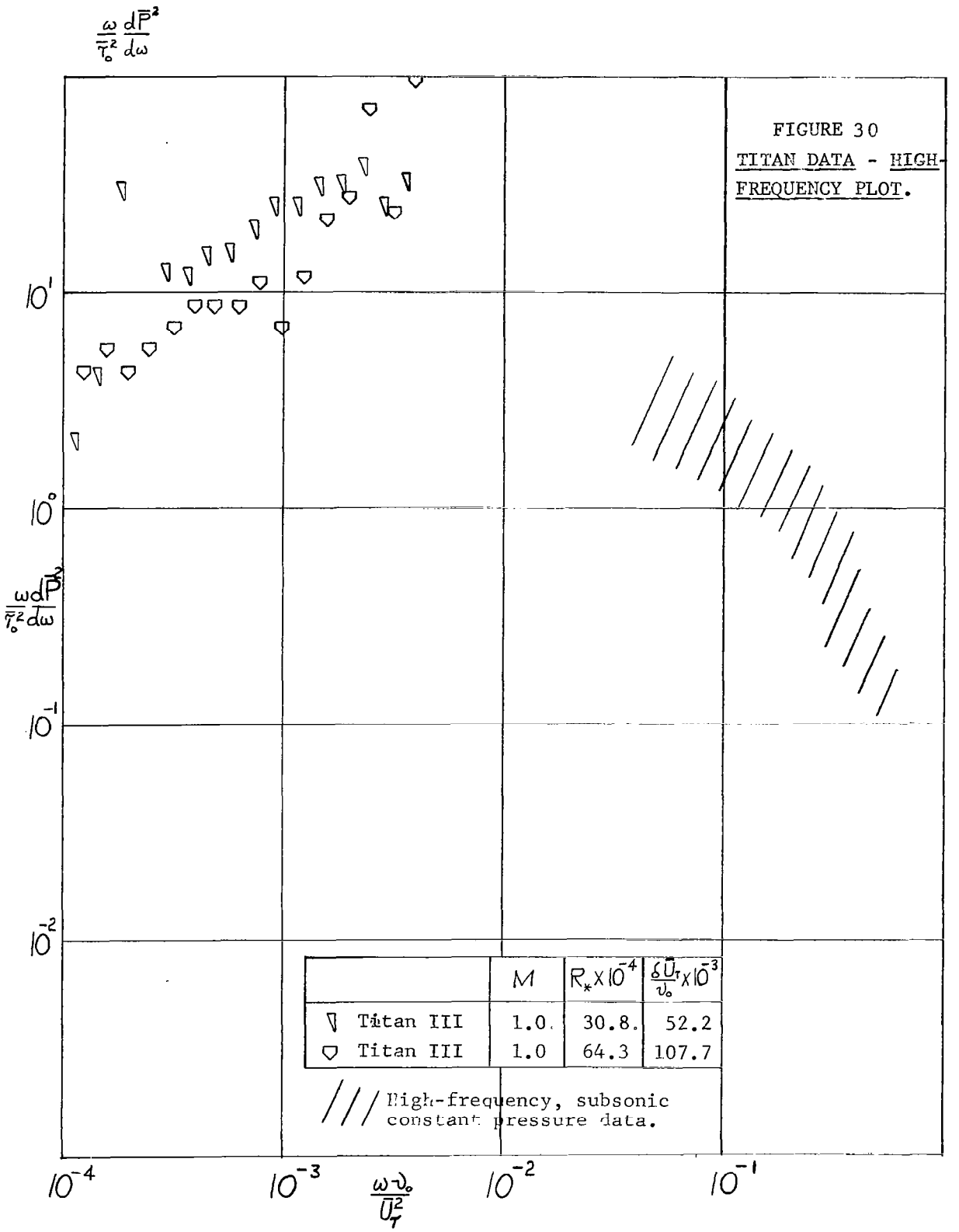


FIGURE 30
TITAN DATA - HIGH-FREQUENCY PLOT.

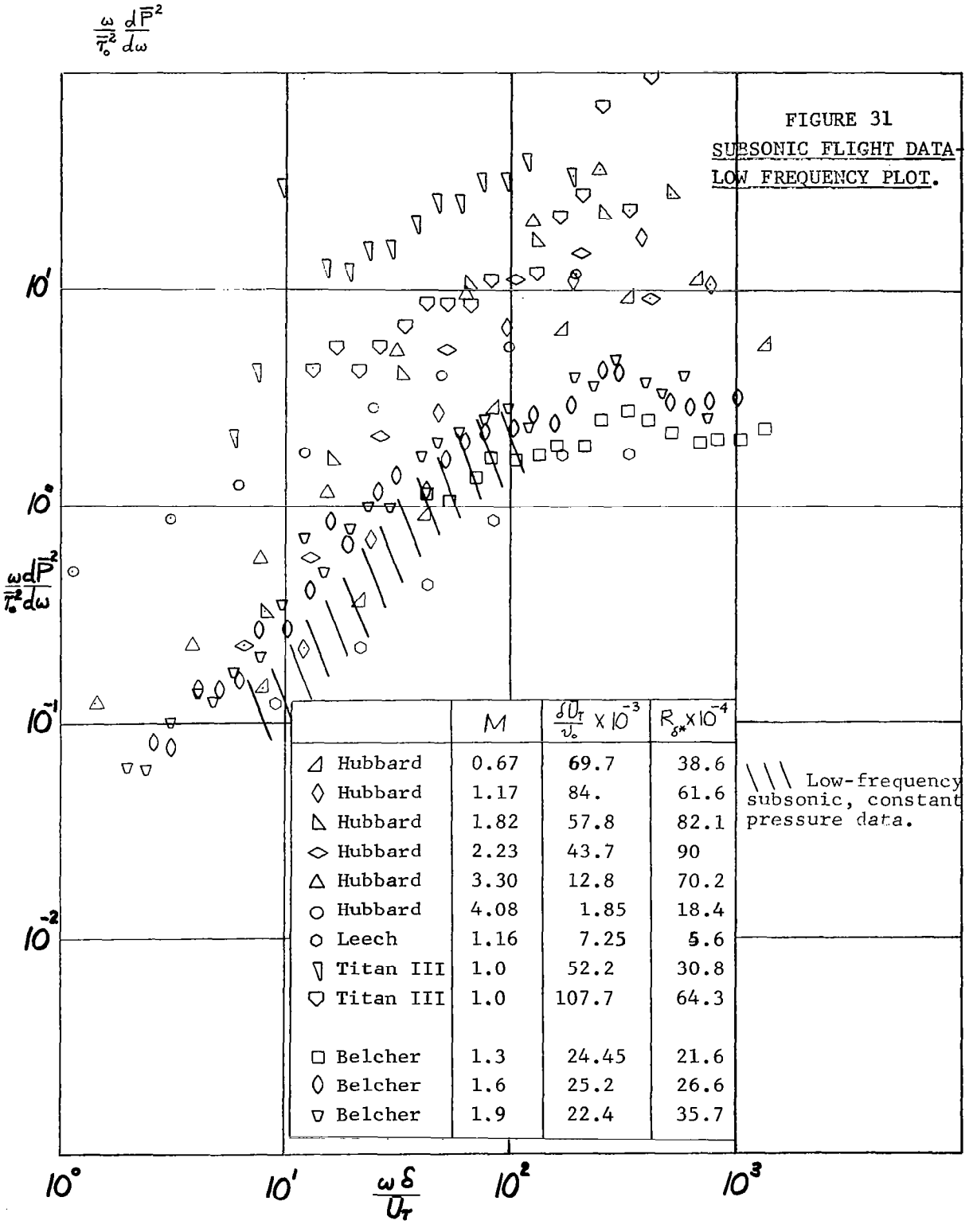


FIGURE 31
SUBSONIC FLIGHT DATA-
LOW FREQUENCY PLOT.

| | M | $\frac{\delta U_\tau}{v_o} \times 10^{-3}$ | $R_{\delta^*} \times 10^{-4}$ |
|---|---|---|---|
| ◿ Hubbard | 0.67 | 69.7 | 38.6 |
| ◇ Hubbard | 1.17 | 84. | 61.6 |
| ◺ Hubbard | 1.82 | 57.8 | 82.1 |
| ◇ Hubbard | 2.23 | 43.7 | 90 |
| △ Hubbard | 3.30 | 12.8 | 70.2 |
| ○ Hubbard | 4.08 | 1.85 | 18.4 |
| ○ Leech | 1.16 | 7.25 | 5.6 |
| ▽ Titan III | 1.0 | 52.2 | 30.8 |
| ▽ Titan III | 1.0 | 107.7 | 64.3 |
| □ Belcher | 1.3 | 24.45 | 21.6 |
| ◇ Belcher | 1.6 | 25.2 | 26.6 |
| ▽ Belcher | 1.9 | 22.4 | 35.7 |

\\\ Low-frequency subsonic, constant pressure data.

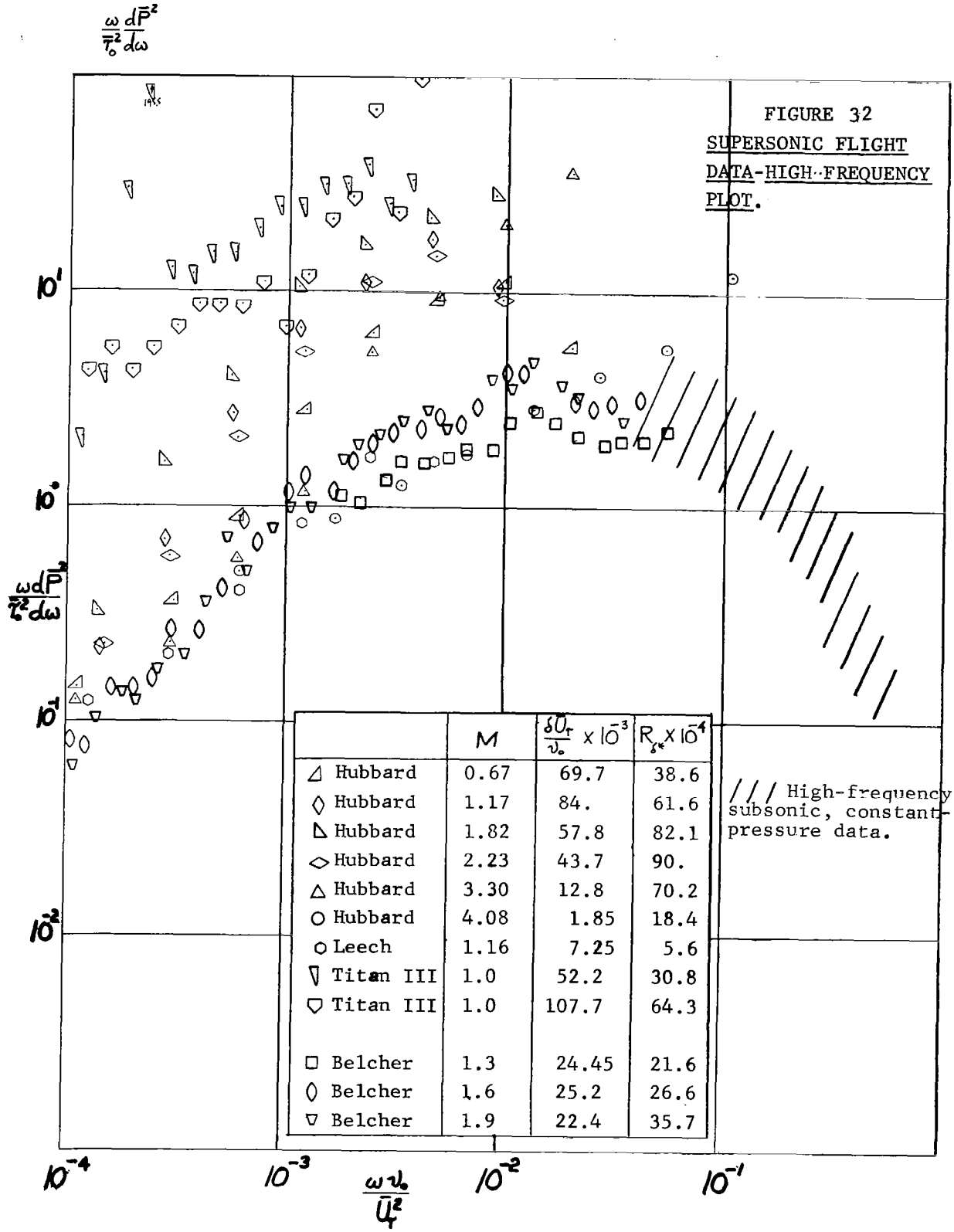


FIGURE 32
SUPERSONIC FLIGHT DATA-HIGH-FREQUENCY PLOT.

| | M | $\frac{\delta U_r}{v_o} \times 10^{-3}$ | $R_{\delta^*} \times 10^{-4}$ |
|---|---|---|---|
| △ Hubbard | 0.67 | 69.7 | 38.6 |
| ◇ Hubbard | 1.17 | 84. | 61.6 |
| ◺ Hubbard | 1.82 | 57.8 | 82.1 |
| ◇ Hubbard | 2.23 | 43.7 | 90. |
| △ Hubbard | 3.30 | 12.8 | 70.2 |
| ○ Hubbard | 4.08 | 1.85 | 18.4 |
| ○ Leech | 1.16 | 7.25 | 5.6 |
| ▽ Titan III | 1.0 | 52.2 | 30.8 |
| ▽ Titan III | 1.0 | 107.7 | 64.3 |
| □ Belcher | 1.3 | 24.45 | 21.6 |
| ◇ Belcher | 1.6 | 25.2 | 26.6 |
| ▽ Belcher | 1.9 | 22.4 | 35.7 |

/// High-frequency subsonic, constant-pressure data.

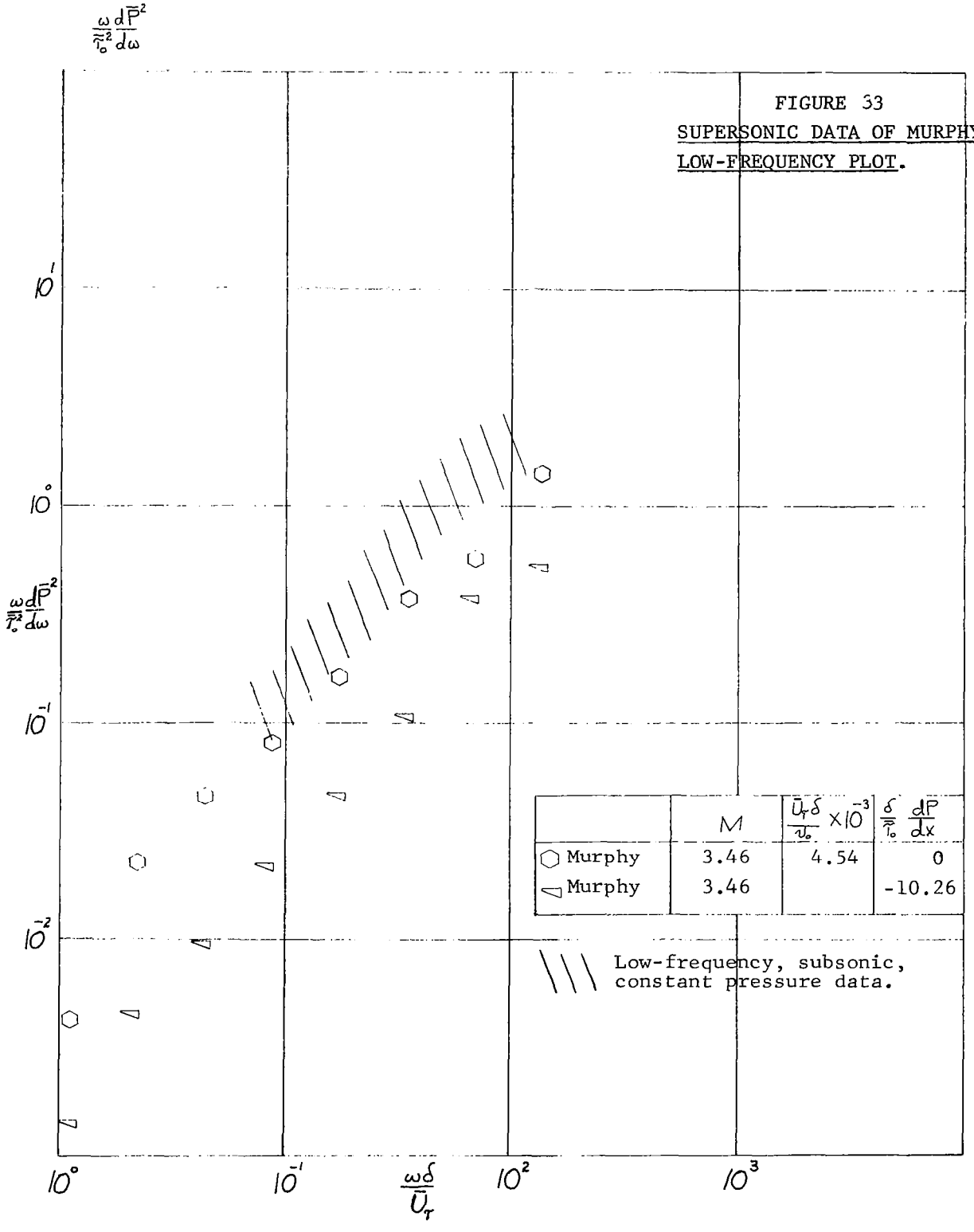


FIGURE 33
SUPERSONIC DATA OF MURPHY-LOW-FREQUENCY PLOT.

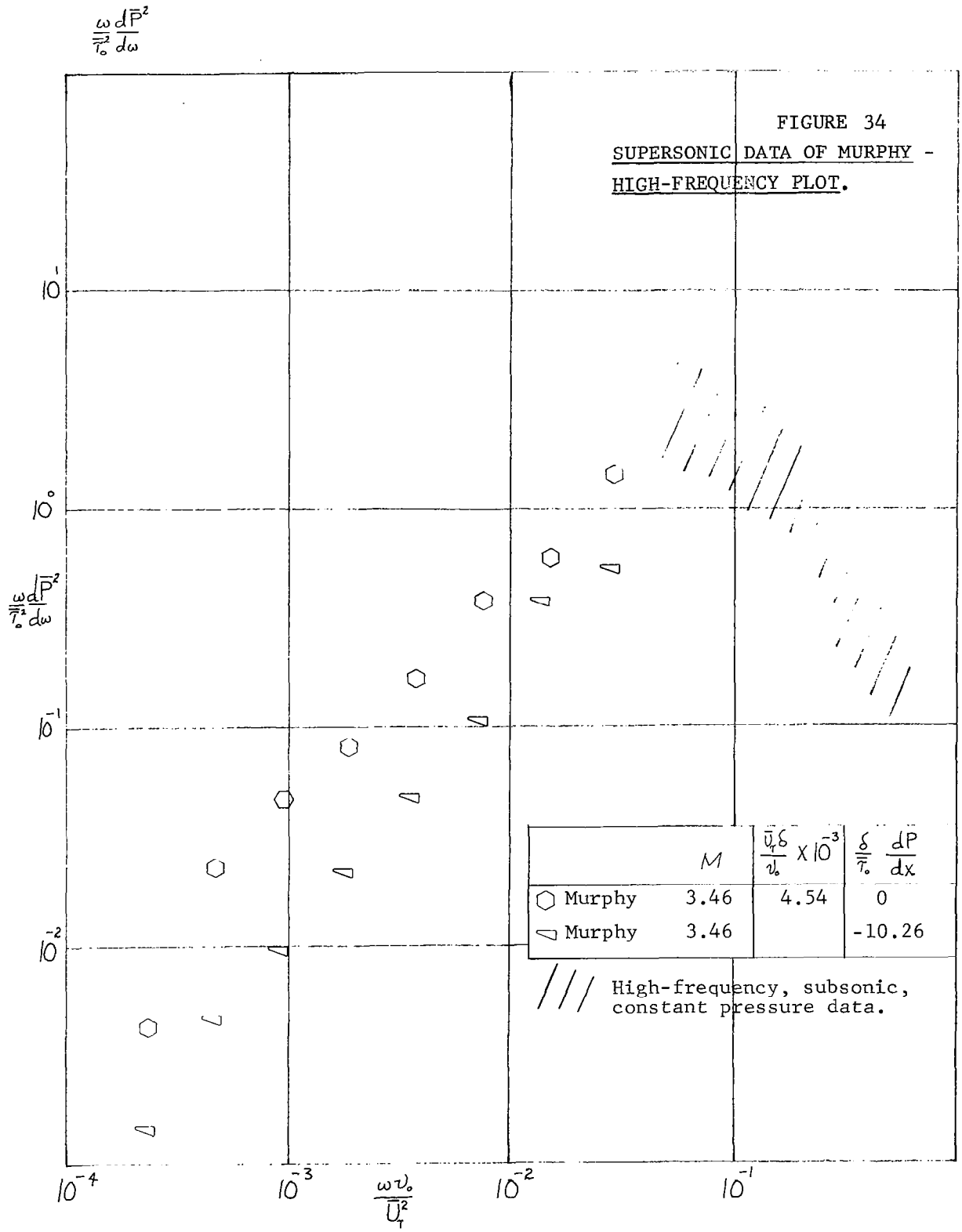


FIGURE 34
SUPERSONIC DATA OF MURPHY - HIGH-FREQUENCY PLOT.

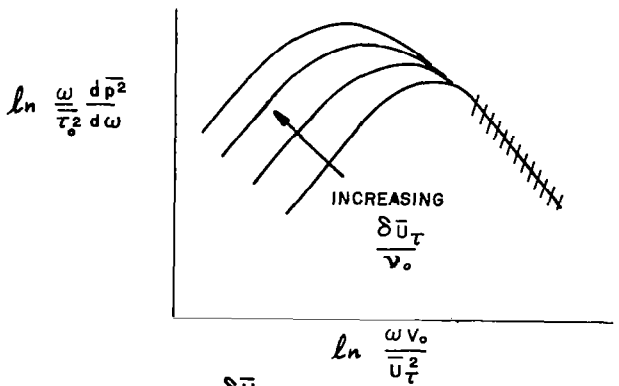


FIGURE 35 a. EFFECT OF $\frac{\delta \bar{U}_\tau}{\nu_o}$ ON LOW FREQUENCY PLOT

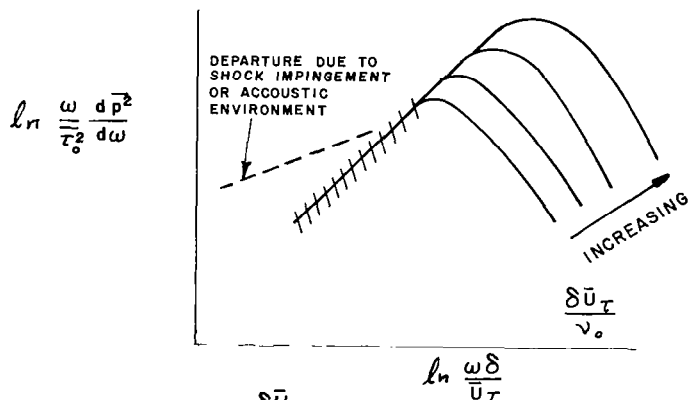


FIGURE 35 b. EFFECT OF $\frac{\delta \bar{U}_\tau}{\nu_o}$ ON HIGH FREQUENCY PLOT

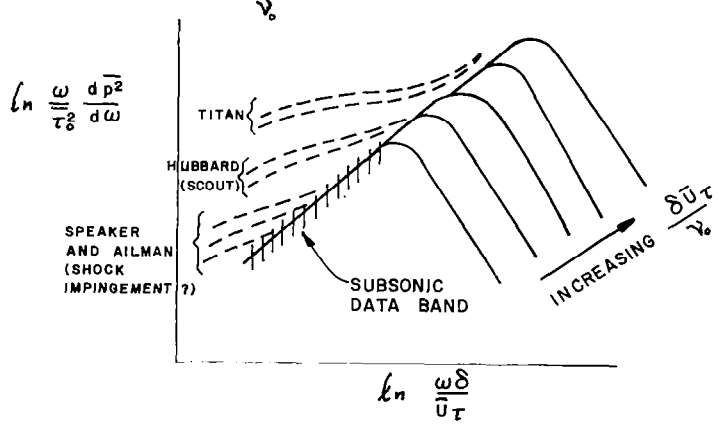


FIGURE 35c. POSSIBLE INTERPRETATION OF TITAN AND SCOUT DATA

FIGURE 35 EFFECT OF $\frac{\delta \bar{U}_\tau}{\nu_o}$ ON SPECTRA